universität wien

MASTERARBEIT / MASTER'S THESIS

Titel der Masterarbeit / Title of the Master's Thesis

„Theoretical investigation of the photodissociation of solvated phenol“

verfasst von / submitted by

Isolde Sandler, BSc

angestrebter akademischer Grad / in partial fulfilment of the requirements for the degree of

Master of Science (MSc)

Wien, 2018 / Vienna 2018

Studienkennzahl lt. Studienblatt / degree programme code as it appears on the student record sheet:	A 066 862
Studienrichtung lt. Studienblatt / degree programme as it appears on the student record sheet:	Masterstudium Chemie
Betreut von / Supervisor:	Univ.-Prof. Dr. Leticia González Herrero

ABSTRACT

In this work, two possible mechanisms for the photodissociation of phenol are investigated: 1) elongation of the O–H bond; 2) reorganization of solvent molecules, facilitating the formation of solvated electrons. In order to investigate the mechanism of O–H elongation, scans of the O–H distance were carried out with CASPT2/CASSCF and ADC(2)/CASSCF to determine the height of the energy barrier between the bright $\pi\pi^*$ state and the dark, dissociative $\pi\sigma^*$ state. While CASPT2 overestimates the barrier, ADC(2) provides better agreement with the experimental time scale for the formation of solvated electrons. From an energetic point of view, the mechanism of O–H elongation is plausible. To investigate the mechanism of reorganization of the solvent molecules, facilitating the formation of a solvated electron, the absorption spectrum and the density of states were calculated with ADC(2) based on snapshots from a classical molecular dynamics simulation. For the description of the environment, a cluster model comprised of 15 water molecules was chosen. While the $\pi\sigma^*$ states are mainly dark, the density of states shows that for several geometries the $\pi\sigma^*$ state has a lower excitation energy than the maximum of the $\pi\pi^*$ band. These low-lying states can be populated after excitation to the $\pi\pi^*$ band by reorganization of the solvent molecules without elongation of the O–H bond. A geometrical analysis reveals that the energy of the $\pi\sigma^*$ state is lowered if the σ^*-orbital is well solvated by a large number of water molecules at a rather large distance from phenol. Our work demonstrates that the reorganization of solvent molecules may drive photodissociation of phenol and suggests that the investigation of this mechanism in derivatives of phenol might be worthwhile.

ZUSAMMENFASSUNG

Im Rahmen dieser Arbeit wurden zwei Mechanismen der Photodissoziation von Phenol untersucht: 1) Elongation der O–H Bindung; 2) Reorganisation der Lösungsmittelmoleküle und die dadurch begünstigte Entstehung von solvatisierten Elektronen. Zur Untersuchung des Mechanismus der O–H-Elongation wurden Scans der O–H-Bindungslänge mit CASPT2/CASSCF und ADC(2)/CASSCF durchgeführt um die Höhe der Energiebarriere zwischen dem Minimum des hellen $\pi\pi^*$-Zustands und dem dunklen, dissoziativen $\pi\sigma^*$-Zustand zu ermitteln. Die mit ADC(2) berechnete Barriere stimmt besser mit der experimentellen Zeitkonstante für die Entstehung von solvatisierten Elektronen überein, während mit CASPT2 die Höhe der Barriere überschätzt wird. Aus energetischer Sicht erscheint der Mechanismus der O–H-Elongation plausibel. Um den Mechanismus der Reorganisierung der Lösungsmittelmoleküle zu untersuchen, der die Entstehung von solvatisierten Elektronen begünstigt, wurden, basierend auf Momentaufnahmen einer klassischen Molekulardynamiksimulation, das Absorptionsspektrum und die Zustandsdichte mittels ADC(2) berechnet. Für die Beschreibung der Umgebung wurde ein Clustermodell bestehend aus 15 Wassermolekülen verwendet. Während die $\pi\sigma^*$-Zustände weitestgehend dunkel sind, zeigt eine Analyse der Zustandsdichte, dass für mehrere Geometrien der $\pi\sigma^*$-Zustand eine geringere Anregungsenergie als das Maximum der $\pi\pi^*$-Bande hat. Durch Reorganisierung der Lösungsmittelmoleküle können diese energetisch niedrigen Zustände nach elektronischer Anregung in die $\pi\pi^*$-Bande ohne Elongation der O–H-Bindung populiert werden. Die Energie des $\pi\sigma^*$-Zustandes wird verringert, wenn das σ^*-Orbital durch eine große Anzahl an Wassermolekülen in einer relativ großen Distanz von Phenol solvatisiert wird. Unsere Arbeit zeigt die Möglichkeit der Photodissoziation von Phenol durch Reorganisation der Lösungsmittelmoleküle und legt eine Untersuchung dieses Mechanismus in Derivaten von Phenol nahe.

CONTENTS

Frequently Used Acronyms

ADC(2)	Algebraic Diagrammatic Construction to 2nd order
ASC	Apparent Surface Charge
CASPT2	Complete Active Space 2nd order Perturbation Theory
CASSCF	Complete Active Space Self-Consistent Field
CC2	Approximate Coupled Cluster of 2nd order
CI	Conical Intersection
COSMO	Conductor-like Screening Model
CT	Charge Transfer
C-PCM	Conductor-like Polarizable Continuum Model
DFT	Density Functional Theory
DHI	5,6-Dihydroxyindole
DOS	Density Of States
LCAO	Linear Combination of Atomic Orbitals
MD	Molecular Dynamics
MM	Molecular Mechanics
MS-CASPT2	Multistate Complete Active Space 2nd order Perturbation Theory
NEVPT2	n-Electron Valence State 2nd order Perturbation Theory
NTO	Natural Transition Orbital
PCM	Polarizable Continuum Model
QM	Quantum Mechanics
SA-CASSCF	State-Averaged Active Space Self-Consistent Field
SCF	Self-Consistent Field
TDA	Tamm-Dancoff Approximation
TDDFT	Time-Dependent Density Functional Theory
UV	Ultraviolet

LIST OF SYMBOLS

$\hat{\alpha}$	Observable
$\alpha(\omega_S)$	Eigenfunction of spin operator
$\alpha(t)$	Expectation value of $\hat{\alpha}$
α_0	Ground-state expectation value of $\hat{\alpha}$
α_1	Linear response of $\hat{\alpha}$
$\hat{\beta}$	Observable
$\beta(\omega_S)$	Eigenfunction of spin operator
∇	Nabla operator
γ	Friction coefficient
γ^{0I}	One-particle transition density matrix in coordinate space
Δt	Length of time step
δ	Delta function
δ_{ij}	Kronecker delta
δ_t	Phase
ε	Orbital energy
ε_0	Vacuum permittivity
ε_d	Distance-dependent dielectric constant
ε_s	Static dielectric constant

ε_{ij}	Depth of potential well in the Lennard-Jones potential
ζ	Collision frequency
η_p	Scaling factor for dimensions of simulation box
θ	Angle
θ_0	Equilibrium angle
λ	Scaling factor
ξ	Compressibility
Ξ	Step function
Π	Polarization propagator
ρ	Electron density
$\hat{\rho}$	Density operator
ρ_0	Electron density of the ground state
ρ_1	First-order density-density response
$\rho_{1\sigma}$	Linear response of spin density
ρ_C	Charge distribution of the chromophore
ρ_S	Electron density of noninteracting reference system
σ	Subscript indicating spin-dependence
σ_{ij}	Bond distance for wich $U_{\text{Lennard-Jones}} = 0$
τ	Time constant
τ_{rel}	Relaxation time
χ	Spin orbital
$\chi_{\alpha\beta}$	Retarded response function
$\chi_{\rho\rho}$	Density-density response function
$\chi_{S,\rho\rho'}$	Kohn-Sham response function
χ_{exc}	Two-particle wavefunction of electron and hole
ϕ	Basis function
ϕ_t	Torsional angle
φ	Spin orbital
φ^{KS}	Kohn-Sham orbital
Φ	First-order interaction space
Ψ	Wavefunction
Ψ_0	Wavefunction of the ground state
Ψ_f	Wavefunction of final state
Ψ_i	Wavefunction of initial state
Ψ_I	Wavefunction in interaction picture
Ψ_S	Wavefunction in Schrödinger picture
Ψ_{CASSCF}	CASSCF wavefunction
Ψ_{HF}	Hartree-Fock wavefunction
Ψ_ν	Configuration in CASSCF
$\Psi^{(0)}$	Zeroth order wavefunction
$\Psi^{(1)}$	First-order correction to the wavefunction
$\Psi^{(2)}$	Second-order correction to the wavefunction
$\Psi^{(3)}$	Third-order correction to the wavefunction
Ψ^I	Wavefunction of state I
Ψ^J	Wavefunction of state J
ψ	Spatial orbital
ψ_e	Electronic wavefunction
ψ_n	Nuclear wavefunction
ψ^e	Natural transition orbital of the electron
ψ^h	Natural transition orbital of the hole
ω	Frequency

ω_{jk}	Difference between the energies of orbitals j and k
ω_s	Spin coordinate
Ω	Frequency corresponding to excitation energy
Ω_{exc}	Norm of the exciton wavefunction
Ω_i	Excitation energy of state i
Ω^{CT}	Charge-transfer number
$\boldsymbol{\Omega}$	Diagonal matrix containing the excitation energies
$\hat{a}$	Annihilation operator
$\hat{a}^\dagger$	Creation operator
c	Coefficient
$\boldsymbol{C}$	Coefficient matrix
$\boldsymbol{D}$	One-particle density matrix
$D_{\mu\nu}^{IJ}$	Element of the one-particle transition density matrix
$\hat{d}$	Dipole operator
d_{exc}	Exciton size
$\tilde{d}_{exc}$	Approximate exciton size
e	Euler's number
e	Elementary charge
e_p	Electron population
$\mathrm{e}_{\mathrm{solv}}$	Solvated electron
e^-	Electron
E	Energy
$\boldsymbol{E}$	Diagonal matrix containing the orbital energies
E_0	Energy of the ground state
E_i	Energy of state i
$E^{(0)}$	Zeroth order energy
$E^{(1)}$	First-order correction to the energy
$E^{(2)}$	Second-order correction to the energy
$E^{(3)}$	Third-order correction to the energy
E_a	Activation energy
E_C	Energy of the chromophore
$E_{C/EN}$	Energy corresponding to the interaction between chromophore and environment
E_e	Energy of the electrons (without internuclear repulsion)
E_{ee}	Energy of electron-electron interaction
E_{el}	Electronic Energy (i. e. absolute energy), containing internuclear repulsion
E_{en}	Energy of electron-nuclei interaction
E_{EN}	Energy of the environment
E_{kin}	Kinetic energy
E_S	Energy of the system
E_{SA}	State-averaged energy
E_{XC}	Exchange-correlation energy
$\hat{E}_{ij}$	Excitation operator
$\hat{f}$	Fock operator
$\hat{f}^{\mathrm{KS}}$	Kohn-Sham operator
f_{XC}	Time-dependent exchange-correlation kernel
f_j	Occupation number of orbital j
$\boldsymbol{f}$	Spectral amplitude vectors
$\boldsymbol{F}$	Fock matrix
$\vec{F}$	Force
$\vec{F}_{\mathrm{random}}$	Random force
F_{ext}	External field

F_{HK}	Hohenberg-Kohn functional
F_{XC}	Exchange-correlation functional
h	Planck's constant
$\hbar$	Reduced Planck's constant
h^+	Hole
H	Hamilton function
$\hat{H}$	Hamilton operator
$\hat{H}'$	Perturbation in the Hamiltonian
$\hat{H}_1$	Time-dependent perturbation
$\hat{H}^{(0)}$	Zeroth order (unperturbed) Hamiltonian
$\hat{H}^{(1)}$	First order Hamiltonian
$\hat{H}^{(2)}$	Second order Hamiltonian
$\hat{H}_C^0$	Hamiltonian of the isolated chromophore
$\hat{H}^{eff}$	Effective Hamiltonian
$\hat{H}_e$	Electronic Hamiltonian
$\hat{H}_S$	Hamiltonian of non-interacting reference system
i	Imaginary unit
J	Coulomb repulsion between electrons
$\hat{J}$	Coulomb operator
k	Reaction rate constant
$\boldsymbol{K_{C,s}}$	Matrix depending on cavity geometry and ε_s
k_{a}	Force constant for angles
k_{B}	Boltzmann's constant
k_{b}	Force constant for bonds
k_{t}	Force constant for torsions
$\hat{K}$	Exchange operator
m	Mass
M	Active space size
$\boldsymbol{M}$	Energy-shifted Hamiltonian
M_A	Mass of a nucleus
m_e	Electron mass
n	Number of electrons
n_i	Occupation number of orbital i
n_t	Periodicity
N	Number of nuclei
N_{conf}	Number of configurations
N_{exc}	Number of excited states
N_{state}	Number of states
$\hat{O}$	Operator
$\hat{O}_I$	Operator in the interaction picture
$\hat{O}_S$	Operator in the Schrödinger picture
$\vec{p}$	Momentum
P	Pressure
P_0	Reference pressure
$P(t)$	Polarization
$\hat{P}$	One-electron operator
POS	Average position of excitation
$\mathrm{POS_F}$	Position of final orbital
$\mathrm{POS_I}$	Position of initial orbital
q	Charge
$\vec{q}$	Vector containing the apparent charges of surface elements
$\vec{q}^*$	Charges calculated for a conductor

Q	Charge
$Q(t)$	Polarization
$\vec{r}$	Electron spatial coordinate vector
r	Distance
r_0	Equilibrium distance
R	Universal gas constant
$\vec{\mathcal{R}}$	Atomic coordinate vector
$\vec{r}_e$	Position vector of electron
$\vec{r}_h$	Position vector of hole
r_{iA}	Distance between electron i and nucleus A
r_{ij}	Distance between electrons i and j
$\vec{R}$	Nuclear coordinates
$\bar{R}$	Parametric dependence on nuclear coordinates
R_{AB}	Distance between nuclei A and B
$\mathcal{S}$	Total spin
$\boldsymbol{S}$	Overlap matrix
S_0	Ground state
S_1	First excited state
S_2	Second excited state
t	Time
T	Temperature
T_S	Kinetic energy of noninteracting reference system
$\hat{T}_e$	Kinetic energy operator for electrons
$\hat{T}_n$	Kinetic energy operator for nuclei
$T[\rho]$	Functional of kinetic energy of electrons
u	Potential
$\tilde{u}$	Potential
u_0	Ground-state potential
u_1	Perturbational potential
u_{XC}	Exchange-correlation potential
u_{XC1}	Linearized exchange-correlation potential
u_S	Effective potential for noninteracting reference system
u_{S1}	First-order effective potential
$\boldsymbol{U}$	Unitary transformation matrix
U	Potential
U_{a}	Potential for angles
U_{b}	Potential for bonds
U_{el}	Potential for electrostatic interactions
$U_{\text{force field}}$	Potential of the force field
U_{t}	Potential for torsions
$U_{\mathrm{vdW,r}}$	Potential for van der Waals and repulsion interactions
$\vec{v}$	Velocity
v^{HF}	Hartree-Fock mean field
$\boldsymbol{V}$	Unitary transformation matrix
V	Volume
$\hat{V}$	Electrostatic potential
V_C	Electrostatic potential of chromophore on surface elements
$V_{C,EN}$	Electrostatic potential due to chromophore and environment
$\hat{V}_{ee}$	Potential energy operator for electron-electron repulsion
$\hat{V}_{en}$	Potential energy operator for electron-nuclei attraction
$\hat{V}_{nn}$	Potential energy operator for nuclei-nuclei repulsion

V_{nn}	Potential energy for nuclei-nuclei repulsion
V_S	Effective potential
w	Weight
$\vec{x}$	Spatial and spin coordinates of an electron
$\boldsymbol{x}$	Transition amplitudes
$\boldsymbol{Y}$	Eigenvectors
Z	Atomic number

1 INTRODUCTION

Phenol (Figure 1) is the chromophore of many important biomolecules, such as the amino acid tyrosine, which is involved in photosynthesis[1], the neurotransmitter dopamine and the hormone adrenaline. The excited-state deactivation mechanism of phenol has been studied extensively both theoretically and experimentally. However, not all possible photodeactivation mechanisms have been elucidated. Especially, regarding the O–H photodissociation mechanisms operable in solvated phenol there are still open questions.

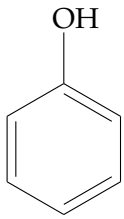

Figure 1. Phenol

According to theoretical studies by Sobolewski et al.,[2–6] the excited-state deactivation mechanism in the gas phase occurs through detachment of the hydrogen atom of the O–H moiety and in solution through excited-state proton transfer[7] from phenol to the solvent.[2–6] For illustration, a scheme of the potential energy landscape of phenol is shown in Figure 2.

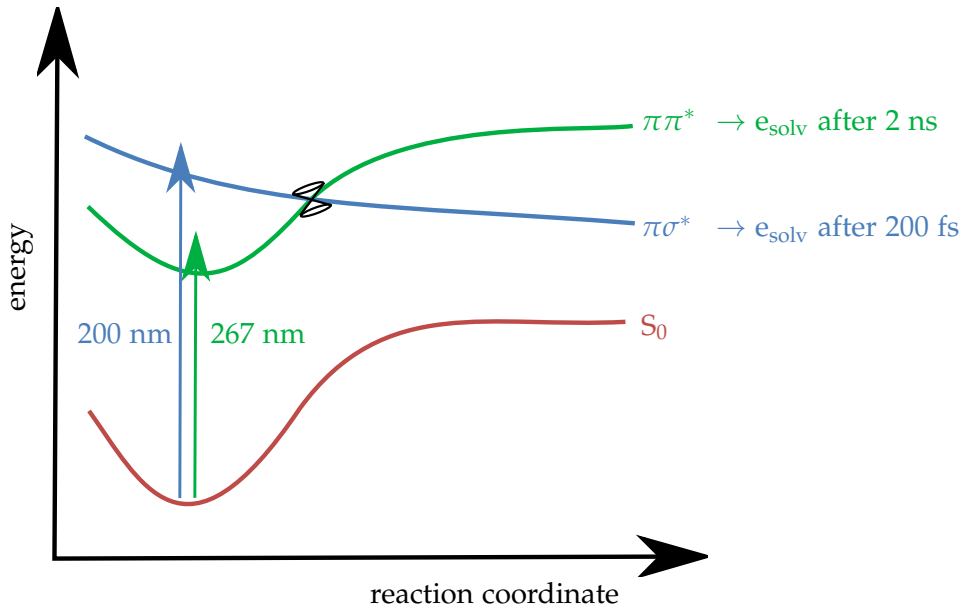

Figure 2. Scheme of the potential energy landscape of phenol to illustrate experimental observations.[8] After excitation with 200 nm light (blue arrow), the formation of solvated electrons is observed after 200 fs. After excitation to the bright S_1 with $\pi\pi^*$ character (green arrow), solvated electrons are observed after 2 ns. The conical intersection is indicated by the funnel.

After excitation to the bright first excited state of $\pi\pi^*$ character (S_1), a conical intersection (CI) to the dark second excited state of $\pi\sigma^*$ character (S_2) is present. This $\pi\sigma^*$ state is dissociative with respect to the O–H distance of phenol. Thus, the reaction

coordinate of the photodissociation reaction is the O–H bond. The transfer of electron and proton occurs concertedly. The σ^* orbital is located at one solvent molecule and, therefore, represents a precursor of the solvated electron. The energy barrier between the minimum of the $\pi\pi^*$ state and the conical intersection between $\pi\pi^*$ and $\pi\sigma^*$ states for gas-phase phenol is about 0.8 eV. For phenol with one water molecule forming a hydrogen bond with the acidic proton, the barrier is about 0.7 eV. With more water molecules, the barrier height is expected to decrease, but this has never been shown. The conical intersection between the $\pi\pi^*$ and $\pi\sigma^*$ states is at an energy of about 5 eV. The existence of a barrier between the $\pi\pi^*$ minimum and the conical intersection between $\pi\pi^*$ and $\pi\sigma^*$ states leads to an energy threshold determining the dynamics and time scale occuring after excitation. Molecules with enough excess energy to overcome this barrier can follow the $\pi\sigma^*$ potential energy surface and either dissociate or relax by internal conversion via another conical intersection present in isolated phenol to the ground state (S_0). If the energy is too low, tunneling under the barrier is possible. Thus, for excitation energies above and below this threshold, different time scales for the photodissociation are expected. Due to this barrier a considerable kinetic isotope effect on fluorescence lifetime and quantum yield is expected.

The hypothesis of Sobolewski et al. is supported by computations carried out by Dixon et al.,[9] who optimized the geometries of phenol with one water molecule for different O–H distances with the complete active space self-consistent field (CASSCF) method with 10 electrons in 10 orbitals while keeping the geometry of the phenyl ring frozen. Excited state energies were calculated employing the complete active space 2nd order perturbation theory (CASPT2) method.

Furthermore, several experiments[10–15,17,19] for gas-phase phenol support the mechanism of photodissociation by O–H elongation. Iqbal et al.[10] excited phenol in the gas phase with a 200 nm laser pulse, which has an energy above the CI between the $\pi\pi^*$ and $\pi\sigma^*$ states. A time constant for H atom formation of 103 ± 30 fs was measured. After excitation with 266 nm light, which is below the energy of the CI, no signal corresponding to the hydrogen atom was observed in the time window up to 200 ps.

Tseng et al.[11] measured the translational energy distribution of the products of photodissociation of gas-phase phenol after excitation with a 248 nm laser pulse. The large velocity of the phenoxyl fragment suggests that the photodissociation occurs on a repulsive state, as predicted by Sobolwski et al.

Nix et al.[12] measured the total kinetic energy release (TKER) spectra in the gas-phase. At excitation wavelengths above 248 nm, phenoxyl radicals and H atoms were observed. At excitation wavelengths below 248 nm, a second peak in the TKER spectrum was observed, suggesting that at high excitation energies another pathway for photodissociation exists.

Iqbal et al.[13] measured the time constants of the formation of hydrogen atoms after excitation of gas-phase phenol as well as phenol deuterated at all positions of the aromatic ring (phenol-d_5) with a 200 nm laser pulse. After 2 ps, two peaks of hydrogen atoms corresponding to high and low kinetic energy were observed. For phenol-d_5 the time constants for the formation of the fast and slow hydrogen atoms were 88 ± 30 fs and 146 ± 25 fs, respectively. If the appearance of the slow hydrogen atoms were due to statictical unimolecular decay, i. e. dissociation of vibrationally excited phenol molecules after internal conversion to the ground state, a larger time constant would be expected.

In accordance with the theoretical description, in an experimental study Roberts et al.[14] observed hydrogen tunneling in gas phase phenol after photoexcitation to S_1 below the predicted energy of the conical intersection to S_2. Phenol was excited with a broadband pump laser pulse centered at 275 nm, which corresponds to the zero point energy of S_1. The time constant for H elimination has been found to be larger than

the temporal limit of this experiment, i. e. $\geq$ 1.2 ns. Moreover, this result suggests that tunneling of the hydrogen atom is the rate-limiting step.

The potential energy landscape of phenol is influenced by the presence of solvent molecules. Lipert et al. measured excited-state lifetimes of the first excited singlet state for isolated phenol[15] as well as for phenol with small clusters of 1, 2 and 3 water molecules[16] by time-resolved pump-probe photoionization. The lifetime of isolated phenol is 2 ± 1 ns. Whereas the singlet-state lifetime of the phenol–$(H_2O)_1$ and phenol–$(H_2O)_3$ clusters are 15 ± 1 ns and 18 ± 1 ns, respectively, the lifetime of the phenol–$(H_2O)_2$ cluster is only 6 ± 1 ns. This difference in life time is attributed to a different pattern of hydrogen bond formation between phenol and the water molecules. In isolated phenol the O–H bond stretching vibration facilitates internal conversion to the ground state. This interpretation is supported by the considerably longer lifetime of deuterated phenol (16 ns) after excitation to S_1.[17] In the clusters containing one and three water molecules the hydrogen bonds hinder the O–H stretching mode. Based on the differences in the absorption spectra of the different clusters[18] and the different lifetimes[16] the authors speculate that this hydrogen bond is weakened or nonexistent in the phenol–$(H_2O)_2$ cluster. Ratzer et al.[19] measured a lifetime of 2.4 ± 0.3 ns for the first excited state of phenol, whereas the lifetime of S_1 of phenol deuterated at the hydroxyl moiety is 13.3 ± 1.6 ns, indicating that in the gas phase the O–H stretching mode is involved in the photodeactivation mechanism.

The fluorescence lifetime of phenol is strongly dependent on the solvent, supporting the conclusion that the presence of hydrogen bonds with the O–H moiety plays an important role in the excited-state deactivation mechanism. In the apolar aprotic solvent cyclohexane the life time of S_1 is 2.4 ± 0.5 ns, while in the polar protic solvent ethanol it is 7.0 ± 0.5 ns.[20] Specifically, it has been shown[21] that in protic solvents the fluorescence lifetimes are larger than in aprotic solvents due to the stabilizing influence of hydrogen bonds on the first excited state of phenol.

Zhang et al.[22] excited phenol in cyclohexane at two different wavelengths. After excitation with 200 nm light, phenoxyl radicals were observed within the time resolution of the experiment, 180 fs. In contrast, when phenol was excited at 267 nm, no phenoxyl radicals were observed within the first nanosecond. After 1.9 ns, a rising signal attributed to the phenoxyl radical was observed. Thus, the dynamics of photodissociation in the apolar aprotic solvent cyclohexane parallels that in the gas phase, with a marked difference in time scale depending on excitation wavelength.

Most experimental studies of the excited-state deactivation mechanism of phenol have been carried out in the gas phase. In contrast, Oliver et al.[8] carried out transient absorption measurements in aqueous solution. For illustration, the potential energy landscape of phenol is schematically depicted in Figure 2. For high-energy excitations (200 nm, 6.2 eV) they observed after 200 fs vibrationally cold phenoxyl radicals and solvated electrons. In addition, another signal attributed to the ground state phenol radical cation $PhOH^{+\bullet}$ was observed, which decays on a sub-picosecond time scale. The occurence of this intermediate species suggests that the photodissociation mechanism of phenol in water does not occur in a concerted way, rather that the electron is transferred to the solvent first and the proton follows after less than one picosecond. The quantum yield for the formation of solvated electrons was determined as 26% after 1 ps and decreasing to 14% after 800 ps due to recombination with phenoxyl radicals. The ratio between solvated electrons and phenoxyl radicals was close to 1, which indicates that almost no neutral hydrogen atoms are produced. For low-energy excitation (267 nm, 4.64 eV), no solvated electrons are observed during the first 2 nanoseconds. Only after more than 2 ns the signal corresponding to solvated electrons begins to rise. Also, the signal corresponding to phenoxyl radicals increases. The quantum yield for the formation of phenoxyl radicals was 13% after 13 ns and the ratio between phe-

noxyl radicals and solvated electrons was 1. Experiments with excitation at 267 nm were also carried out for deuterated phenol (phenol-d_1). The kinetics observed was similar, giving a value for the kinetic isotope effect of 1.0 ± 0.4. This small value indicates that tunneling of the hydrogen atom, if it exists, is not the rate-limiting step in solution, in contrast to the gas phase. The authors suggest that, after excitation to vibrationally excited states of S_1, the molecule relaxes to the vibrational ground state of S_1 and then undergoes slow autoionization to yield $PhOH^{+\bullet}$ and solvated electrons, after which fast deprotonation occurs. After low-energy excitation no signal due to the intermediate species $PhOH^{+\bullet}$ was observed, which can be attributed to the short lifetime of this species. Thus, the experimental results by Oliver et al. suggest that for phenol in bulk solution of a polar protic solvent like water a different mechanism governs the excited-state deactivation process than in the gas phase. The time scale for the formation of solvated electrons after low-energy excitation allows to estimate the height of the energy barrier for this reaction based on the Arrhenius equation[23]

$$k = \frac{k_B T}{h} e^{-E_a/RT} \tag{1}$$

where k_B is Boltzmann's constant, T is the temperature, h is Planck's constant, E_a is the activation energy, R is the universal gas constant and k is the rate constant

$$k = \frac{1}{\tau} \tag{2}$$

with τ being the time constant. Using the experimentally observed time scale of about 2 ns, the lower limit of the energy barrier is expected to be about 0.24 eV. In Chapter 3, this value will be compared to energy barriers calculated with different quantum chemical methods.

Further evidence for a sequential instead of concerted transfer of electron and proton to the solvent was described for the phenol derivative 5,6-dihydroxyindole (DHI) by Nogueira et al.[24] 5,6-dihydroxyindole is a building block of the pigment eumelanin[25,26] that protects human skin cells from photodamage due to UV radiation.[27] DHI in aqueous buffer solution was excited with 280 nm radiation to the first excited state of $\pi\pi^*$ character.[24] The lifetime of this state is 103 ± 10 ps. Theoretical calculations employing time-dependent density functional theory (TDDFT) were carried out for DHI with 10 water molecules. After excitation to S_1, the cluster relaxes to the minimum of the $\pi\pi^*$ state. The solvent molecules reorganize and facilitate the transfer of an electron from one O–H moiety to the solvent. After the formation of the solvated electron, the proton is transfered to a solvent molecule which is not participating in the stabilization of the solvated electron. If D_2O instead of H_2O is used, the reaction is considerably slower, with a kinetic isotope effect of 3, which suggests that the time-limiting step is the proton transfer. Thus, for 5,6-dihydroxyindole the reaction coordinate is reorientation of the solvent molecules rather than elongation of the O–H bond.

The experiments carried out for gas-phase phenol[10–15,17,19] support the hypothesis from Sobolewski et al.[2–6] that the reaction coordinate of photodissociation is the O–H bond. In contrast, the experiment for phenol in aqueous solution[8] suggests that a different mechanism mediated by the solvent might be operative. Furthermore, theoretical investigations of the phenol derivative 5,6-dihydroxyindole[24] show that the reaction mechanism in water involves the formation of a solvated electron facilitated by reorganization of solvent molecules. Therefore, the goal of this work is to investigate the photodissociation of phenol considering two possible mechanisms: 1.) elongation of the O–H bond; 2.) solvent reorganization facilitating the formation of a solvated electron. For the investigation of the first mechanism, excited state optimizations for the $\pi\pi^*$ and $\pi\sigma^*$ state at different O–H bond distances were carried out to estimate the height of the energy barrier of this reaction. To investigate the second mechanism,

first, different solvent models were tested to find a suitable method. Then, the absorption spectrum and density of states (DOS) were calculated based on snapshots from a classical molecular dynamics simulation. The electronic structure of spectrum and DOS were analyzed to determine whether population of the $\pi\sigma^*$ state after excitation to the $\pi\pi^*$ state is possible already in the Franck-Condon region without elongation of the O–H bond. Finally, a geometrical analysis was carried out in order to identify possible geometrical features of the orientation of the solvent molecules contributing to a lowering of the energy of the $\pi\sigma^*$ state.

2

THEORY

In this chapter, the theoretical background of the methods employed in this work will be explained briefly. Since configurational sampling by means of a molecular dynamics simulation was used, this method will be discussed in the first section. Absorption spectra of phenol in water were calculated employing different quantum chemical methods. Therefore, in section 2.2 the basis of quantum chemistry, the Schrödinger equation, will be introduced. Then, one of the most commonly used approximations, the Hartree-Fock method, will be discussed, followed by a brief explanation of two multiconfigurational methods, Complete Active Space Self-Consistent Field (CASSCF) and Complete Active Space 2nd order Perturbation Theory (CASPT2), which were used in this work. For the calculation of absorption spectra and density of states of phenol solvated by small clusters of water molecules the single-reference method ADC(2) was used. This method will be explained in section 2.6. For comparison with the CASPT2 and ADC(2) results, calculations employing density functional theory (DFT) were carried out. Therefore, in section 2.7, DFT for the ground state as well as for excited states will be discussed, including a short introduction to linear-response theory. In order to simulate bulk solvation, two methods combining quantum mechanical calculations for the chromophore and classical calculations for the solvent were employed. In section 2.8 these methods for the description of the environment will be explained. After calculation of absorption spectrum and density of states, the excited states were characterized by means of methods for the analysis of the wavefunction, which will be outlined in the last section. When a new concept is introduced or a term is defined in this chapter, it will be emphasized in italics. In the equations the following notational convention will be used: vectors will be signified by arrows, e. g. $\vec{r}$, matrices will be typeset in bold, e. g. $\boldsymbol{F}$.

2.1 MOLECULAR DYNAMICS

2.1.1 *Equations of motion*

In molecular dynamics (MD),[28,29] the motion of nuclei is simulated by integrating Hamilton's equations of motion.

$$\frac{d\vec{\mathcal{R}}_A}{dt} = \frac{\partial H}{\partial \vec{p}_A} = \frac{\vec{p}_A}{m_A} \tag{3}$$

$$\frac{d\vec{p}_A}{dt} = -\frac{\partial H}{\partial \vec{\mathcal{R}}_A} = -\frac{\partial U}{\partial \vec{\mathcal{R}}_A} = \vec{F}_A \tag{4}$$

where $\vec{\mathcal{R}}_A$, $\vec{p}_A$ and m_A are the position, momentum and mass of particle A, H is the Hamilton function and $\vec{F}$ is the force. These equations have to be solved numerically. To accomplish this, a time step of e. g. 1 fs needs to be chosen. Beginning from a starting geometry of a set of molecules, the equations are solved for each time step. To integrate Hamilton's equations of motion, several integration methods can be used.

Verlet

In the Verlet algorithm,[30] the position $\vec{\mathcal{R}}$ of an atom at time $t + \Delta t$ is calculated based on its positions at the times t and $t - \Delta t$ and the forces at time t:[28]

$$\vec{\mathcal{R}}(t + \Delta t) = 2\vec{\mathcal{R}}(t) - \vec{\mathcal{R}}(t - \Delta t) + \frac{\vec{F}}{m}\Delta t^2 \tag{5}$$

The velocities $\vec{v}$ do not explicitely enter the computation of $\vec{\mathcal{R}}$ but can be calculated afterwards from the positions:

$$\vec{v}(t) = \frac{\vec{\mathcal{R}}(t + \Delta t) - \vec{\mathcal{R}}(t - \Delta t)}{2\Delta t} \tag{6}$$

This algorithm is susceptible to a loss of accuracy during the simulation since a small quantity ($\vec{F}\Delta t^2/m$) is added to the difference of two large quantities, namely the position vectors at times t and $t - \Delta t$. Therefore, different mathematical formulations of this algorithm have been developed to improve the numerical stability. In addition, explicit inclusion of velocities in the calculation of the motion would be preferable so that they can be scaled in order to control the temperature of the system by thermostats.

Leap frog

In the Leap Frog algorithm[31] the velocities explicitely enter the calculation of the positions. Moreover, this algorithm is numerically more stable since no differences of large quantities have to be calculated. A disadvantage is that positions and velocities are not synchronous, i. e. while positions are calculated for the times $t + i\Delta t$, the velocities are calculated for the times $t + \frac{i\Delta t}{2}$:[28]

$$\vec{v}\left(t + \frac{\Delta t}{2}\right) = \vec{v}\left(t - \frac{\Delta t}{2}\right) + \frac{\vec{F}}{m}\Delta t \tag{7}$$

$$\vec{\mathcal{R}}(t + \Delta t) = \vec{\mathcal{R}}(t) + \vec{v}\left(t + \frac{\Delta t}{2}\right)\Delta t \tag{8}$$

Velocity Verlet

The *Velocity Verlet* algorithm[32] has the advantages that the velocities explicitely enter the computation and that positions and velocities are synchronous. In addition, it is numerically stable. First, the forces at time t are calculated based on an evalution of the potential energy. Then, the positions at time $t + \Delta t$ are calculated from the positions, velocities and forces at time t:

$$\vec{\mathcal{R}}(t + \Delta t) = \vec{\mathcal{R}}(t) + \vec{v}(t)\Delta t + \frac{\vec{F}}{2m}\Delta t^2 \tag{9}$$

As a third step, the forces at time $t + \Delta t$ are calculated since they are needed for the computation of the velocities at time $t + \Delta t$:

$$\vec{v}(t + \Delta t) = \vec{v}(t) + \frac{\vec{F}(t) + \vec{F}(t + \Delta t)}{2m}\Delta t \tag{10}$$

2.1.2 *Force Field*

As can be seen in equations 5, 7, 9 and 10 the evaluation of the gradient of the potential energy is necessary to integrate the equations of motion. The potential in which the atoms move can be calculated by quantum chemical methods. However, for systems

containing a large number of molecules, high-level calculations are unfeasible. In classical MD, the forces on the nuclei are calculated based on the evaluation of a potential U described by a force field, which usually contains five terms:

$$U_{\text{force field}} = U_{\text{b}} + U_{\text{a}} + U_{\text{t}} + U_{\text{el}} + U_{\text{vdW,r}} \tag{11}$$

For the potentials of bonds and angles, U_{b} and U_{a}, the harmonic oscillator approximation is used:[28]

$$U_{\text{b}} = \frac{1}{2} k_{\text{b}} (r - r_0)^2 \tag{12}$$

$$U_{\text{a}} = \frac{1}{2} k_{\text{a}} (\theta - \theta_0)^2 \tag{13}$$

where the parameters representing equilibrium bond lengths and angles, r_0 and θ_0, as well as force constants, k_{b} and k_{a} are determined experimentally or by quantum chemical calculations. The torsional potential is described by a sum of cosine functions:

$$U_{\text{t}} = \sum_i \frac{1}{2} k_{\text{t},i} \left(1 + \cos(n_t \phi_t - \delta_{t,i})\right) \tag{14}$$

where n_t is a factor that describes the symmetry of the potential, ϕ_t is the torsional angle and $\delta_{t,i}$ is the phase. The van der Waals and repulsion interactions are usually approximated by a Lennard-Jones potential[33] of the form[28]

$$U_{\text{vdW,r}} = 4\varepsilon_{AB} \left[\left(\frac{\sigma_{AB}}{r_{AB}} \right)^{12} - \left(\frac{\sigma_{AB}}{r_{AB}} \right)^{6} \right] \tag{15}$$

where ε_{AB} is the depth of the potential well and σ_{AB} is the bond distance for which $U_{\text{vdW,r}} = 0$. The Coulomb potential, here written in atomic units, describes the electrostatic term for two charges q_A and q_B

$$U_{\text{el}} = \frac{q_A q_B}{r_{AB}} \tag{16}$$

The van-der-Waals and electrostatic interactions are termed *nonbonded interactions*.

Whereas the computational effort for the potentials for bonds, angles and torsions grows linearly with the size of the molecule, nonbonded interactions have to be calculated between all pairs of atoms. Therefore, computational cost increases as N^2, where N is the number of atoms. For van der Waals interactions a cutoff value can be employed since the strength of the interactions decreases very fast with r^{-6}. This cutoff value is usually of the order of 10 Å. In contrast to the van der Waals potential, the Coulomb potential has a comparatively long-range decay due to its r^{-1}-dependence. Therefore, a special treatment is necessary and it is not possible to employ a small cutoff value.[34] For systems with periodic boundary conditions (*vide infra*), *Ewald sum*[35] methods can be employed to calculate the electrostatic interactions, which reduce the scaling to $N^{3/2}$ or even $N\,log N$ in case of the Particle Mesh Ewald summation.[36–38]

2.1.3 *Periodic boundary conditions*

In order to avoid surface effects due to a too small number of solvent molecules, periodic boundary conditions can be employed: The system is placed in a box of the form of a cube or a truncated octahedron. This box is replicated in all directions of space, but the equations of motion are only solved for the original box. Thus, the atoms inside the replica boxes mimic the motion of the atoms in the original box. If a solvent molecule leaves the box on one side, an image of this molecule enters the box at the opposite side. Employing periodic boundary conditions, bulk solution can be simulated with a rather limited number of solvent molecules.[29]

2.1.4 *Thermostats and barostats*

Chemical reactions are often carried out in open vessels, i. e. the temperature and the pressure are kept constant. In order to simulate these conditions in molecular dynamics, different thermostats[39] and barostats[40–49] have been developed. Here, only the methods that have been used in this work will be explained, namely the Langevin thermostat and the Berendsen barostat.

In a molecular dynamics simulation, the instantaneous temperature of a system is related to the velocities of the particles as[28]

$$T = \frac{\sum_{A}^{N} m_A \vec{v}_A^2}{3k_B N} \tag{17}$$

where k_B is Boltzmann's constant. With the *Langevin thermostat*,[50] the velocities of the atoms A are modified every l time steps by employing a "friction coefficient" γ and a random force $\vec{F}_{\text{random}}$. Thus, the Hamilton equation (4) is modified as

$$\frac{d\vec{p}_A}{dt} = \vec{F}_A - \gamma \vec{v}_A + \vec{F}_{\text{A, random}} \tag{18}$$

Thus, the fastest atoms experience the largest friction while the random force counteracts the friction and ensures that the average temperature of the system does not decrease.

The friction coefficient is related to the *collision frequency* ζ, which is commonly used to characterize a Langevin thermostat, as[51]

$$\gamma = m\zeta \tag{19}$$

The pressure of the system is calculated according to[52]

$$P = \frac{1}{3V}\left(3Nk_B T + \sum_{A \neq B} \vec{\mathcal{R}}_{AB}\vec{F}_{AB}\right) \tag{20}$$

where V is the volume of the box and $\vec{\mathcal{R}}_{AB}$ and $\vec{F}_{AB}$ are the difference between the coordinate vectors and the forces between particles A and B, respectively.

Employing the *Berendsen barostat*,[41] the dimensions of the simulation box are scaled by the factor η_p, which can induce alterations in the volume V.

$$\eta_p = \left(1 + \frac{\Delta t}{\tau_{rel}}\xi(P - P_0)\right)^{\frac{1}{3}} \tag{21}$$

where τ_{rel} is the relaxation time and ξ is the compressibility of the system. P_0 is the desired pressure.

2.2 THE SCHRÖDINGER EQUATION

Most of quantum chemistry is concerned with finding approximate solutions to the *Schrödinger equation*,[53] which is given in its non-relativistic, time-independent form as

$$\hat{H}\,|\Psi\rangle = E\,|\Psi\rangle \tag{22}$$

where $\hat{H}$ is the *Hamilton operator*, which describes the interactions between the particles of a system, E is the total energy and $|\Psi\rangle$ is the *wavefunction* of the system. For a

molecule consisting of atomic nuclei and electrons, the Hamiltonian consists of five parts:[54]

$$\hat{H} = \underbrace{-\sum_{i=1}^{n} \frac{1}{2}\nabla_i^2}_{\hat{T}_e} \underbrace{-\sum_{A=1}^{N} \frac{1}{2m_A}\nabla_A^2}_{\hat{T}_n} + \underbrace{\sum_{i=1}^{n}\sum_{j>i}^{n} \frac{1}{r_{ij}}}_{\hat{V}_{ee}} + \underbrace{\sum_{A=1}^{N}\sum_{B>A}^{N} \frac{Z_A Z_B}{R_{AB}}}_{\hat{V}_{nn}} \underbrace{-\sum_{i=1}^{n}\sum_{A=1}^{N} \frac{Z_A}{r_{iA}}}_{\hat{V}_{en}} \tag{23}$$

$\hat{T}_e$ and $\hat{T}_n$ are the kinetic energy operators for n electrons and N nuclei. $\hat{V}_{ee}$ and $\hat{V}_{nn}$ describe the electrostatic repulsion between electrons and nuclei, respectively. r_{ij} and R_{AB} are the distances between two electrons and two nuclei, respectively. Z_A is the atomic number of nucleus A. $\hat{V}_{en}$ is the Coulomb operator for the electrostatic attraction between electrons and nuclei. r_{iA} is the distance between electron i and nucleus A and

$$\nabla^2 = \frac{\partial^2}{\partial x^2} + \frac{\partial^2}{\partial y^2} + \frac{\partial^2}{\partial z^2} \tag{24}$$

Here, atomic units are used to simplify notation. Thus, $\hbar$, the mass of the electron m_e and the elementary charge e are unity. m_A, the mass of a nucleus, is expressed in units of m_e.

For systems containing more than two particles, the Schrödinger equation cannot be solved analytically. However, the assumption that the motion of nuclei happens on a different timescale than that of the electrons since they are about 1000 times heavier is often valid. Then, the total wavefunction can be split in an electronic and a nuclear part:

$$|\Psi(\vec{r}, \vec{R})\rangle = |\psi_e(\vec{r}, \bar{R})\rangle \, |\psi_n(\vec{R})\rangle \tag{25}$$

as proposed by Born and Oppenheimer in 1927.[55] $|\psi_n(\vec{R})\rangle$ and $|\psi_e(\vec{r}, \bar{R})\rangle$ are the nuclear and electronic wavefunctions, respectively. $|\psi_e\rangle$ depends parametrically on the nuclear coordinates $\bar{R}$ and explicitely on the electronic coordinates $\vec{r}$. Thus, for a fixed nuclear geometry, $\hat{T}_n = 0$ and $\hat{V}_{nn}$ is constant. In this way, the *electronic Schrödinger equation* becomes:[54]

$$\hat{H}_e \, |\psi_e\rangle = E_e \, |\psi_e\rangle \tag{26}$$

where the Hamiltonian contains only $\hat{T}_e$, $\hat{V}_{ee}$ and $\hat{V}_{en}$. The total energy is then obtained as

$$E_{el} = E_e + V_{nn} \tag{27}$$

This equation can in principle be solved for different nuclear geometries. However, in practice, further approximations have to be introduced in order to actually solve equation 27.

2.3 HARTREE-FOCK

The Hartree-Fock approximation[54] is the basis for most higher-level methods of quantum chemistry, which add corrections to it as described in later sections. In the Hartree-Fock method, the many-electron wavefunction is approximated as a *Slater determinant* consisting of one-electron wavefunctions (*spin orbitals* $|\chi_i(\vec{x}_i)\rangle$)

$$|\Psi(\vec{x}_1, \vec{x}_2, \ldots, \vec{x}_n)\rangle = \frac{1}{\sqrt{n!}} \begin{vmatrix} \chi_1(\vec{x}_1) & \chi_2(\vec{x}_1) & \cdots & \chi_n(\vec{x}_1) \\ \chi_1(\vec{x}_2) & \chi_2(\vec{x}_2) & \cdots & \chi_n(\vec{x}_2) \\ \vdots & \vdots & \ddots & \vdots \\ \chi_1(\vec{x}_n) & \chi_2(\vec{x}_n) & \cdots & \chi_n(\vec{x}_n) \end{vmatrix} \tag{28}$$

where $\vec{x}$ denotes the spatial and spin coordinates of an electron. The *spin orbitals* $|\chi_i(\vec{x}_i)\rangle$ consist of the *spatial orbitals* $|\psi_i(\vec{r}_i)\rangle$, depending only on the spatial coordinates

$\vec{r}$, times one of the eigenfunctions of the spin operator, $|\alpha(\omega_s)\rangle$ and $|\beta(\omega_s)\rangle$ with the spin coordinate ω_s.

For the Hartree-Fock method the *variation principle* is used, which states that the energy calculated for a trial wavefunction is always greater than the exact ground state energy, unless the trial wavefunction equals the exact ground state wavefunction. Therefore, a trial wavefunction can be improved by varying its parameters to give the lowest obtainable energy.

In accordance with the variational principle, the energy of the Slater determinant is minimized by optimizing the orbitals. Thus, n coupled single-particle equations are obtained, which have to be solved iteratively.

$$\hat{f}(\vec{x}_i)\,|\chi(\vec{x}_i)\rangle = \varepsilon_\nu\,|\chi(\vec{x}_i)\rangle \tag{29}$$

ε_ν are the orbital energies, $\hat{f}$ is the Fock operator:

$$\hat{f}(\vec{x}_i) = -\frac{1}{2}\nabla_i^2 - \sum_{A=1}^{N}\frac{Z_A}{r_{iA}} + v^{\mathrm{HF}}(\vec{x}_i) \tag{30}$$

where v^{HF} is the *average* potential being exerted on electron i by the other electrons.

$$v^{\mathrm{HF}}(\vec{x}_i) = \sum_{b=1}^{n}\left(\hat{J}_b(\vec{x}_i) - \hat{K}_b(\vec{x}_i)\right) \tag{31}$$

where the *Coulomb operator* describes the repulsion between the ith electron and electron j in spin orbital $|\chi_b\rangle$

$$\hat{J}_b(\vec{x}_i)\,|\chi_a(\vec{x}_i)\rangle = \left\langle \chi_b(\vec{x}_j)\,\middle|\,\frac{1}{r_{ij}}\,\middle|\,\chi_b(\vec{x}_j)\right\rangle |\chi_a(\vec{x}_i)\rangle \tag{32}$$

whereas the *exchange operator* does not have a classical interpretation.

$$\hat{K}_b(\vec{x}_i)\,|\chi_a(\vec{x}_i)\rangle = \left\langle \chi_b(\vec{x}_j)\,\middle|\,\frac{1}{r_{ij}}\,\middle|\,\chi_a(\vec{x}_j)\right\rangle |\chi_b(\vec{x}_i)\rangle \tag{33}$$

The Fock operator depends on its eigenfunctions, i. e. on *all* spin orbitals. Thus, the Hartree-Fock equations can only be solved iteratively. In order to do this, further approximations are introduced.

Since linear algebra problems can be very efficiently solved by modern computers, the Hartree-Fock problem is reformulated by introducing a *basis set* in which the orbitals are expanded. If pairs of spin orbitals $|\chi\rangle$ are constrained to have the same spatial part $|\psi\rangle$, the method is termed *Restricted Hartree-Fock*. The *linear combination of atomic orbitals* (LCAO) expansion can be written as

$$|\psi_i\rangle = \sum_{\mu=1}^{k} c_{\mu i}\,|\phi_\mu\rangle \tag{34}$$

where $|\phi_\mu\rangle$ is a set of k atom-centered basis functions, from which the molecular orbitals ψ_i are constructed. Many sets of basis functions for calculations with various methods and at different levels of accuracy have been developed.[56–58] Usually, linear combinations of Gaussian functions with different parameters controlling spatial extension are used. Then, the coefficients $c_{\mu i}$ of the molecular spatial orbitals have to be determined using equation 29[54]

$$\hat{f}(\vec{r}_i)\sum_{\nu}^{k} c_{\nu i}\,|\phi_\nu(\vec{r}_i)\rangle = \varepsilon_i\sum_{\nu}^{k} c_{\nu i}\,|\phi_\nu(\vec{r}_i)\rangle \tag{35}$$

The *Roothaan-Hall equations* are obtained after premultiplying both sides by $\langle\phi_\mu|$

$$\sum_\nu^k c_{\nu i} \underbrace{\langle\phi_\mu|\,\hat{f}(\vec{r}_i)\,|\phi_\nu\rangle}_{F_{\mu\nu}} = \varepsilon_i \sum_\nu^k c_{\nu i} \underbrace{\langle\phi_\mu|\phi_\nu\rangle}_{S_{\mu\nu}} \tag{36}$$

which can be written in matrix form as

$$\boldsymbol{FC} = \boldsymbol{SCE} \tag{37}$$

The *Fock matrix* $\boldsymbol{F}$ and the *overlap matrix* $\boldsymbol{S}$ are $k \times k$ dimensional hermitian matrices. $\boldsymbol{C}$ contains the coefficients of the molecular spatial orbitals. The orbital energies are the elements of the diagonal matrix $\boldsymbol{E}$.

The Roothaan-Hall equations have to be solved iteratively with the *self-consistent field* (SCF) method: A first guess of the coefficients is made. Then, the Roothaan-Hall equations are solved, yielding a new set of coefficients, which is then used to again solve the equations until the new and old orbitals do not differ anymore by more than a specified threshold, i. e. until self-consistency is reached. The Hartree-Fock wavefunction $|\Psi_{HF}\rangle$ is then constructed from the $n/2$ lowest-lying orbitals.

The Hartree-Fock total energy is then

$$\begin{aligned} E_{HF} &= \langle\Psi_{HF}|\hat{H}|\Psi_{HF}\rangle = \\ &= -\sum_{i=1}^{n/2}\left\langle\phi_\mu(\vec{r}_i)\left|\frac{1}{2}\nabla_i^2\right|\phi_\mu(\vec{r}_i)\right\rangle + \sum_{i=1}^{n/2}\left\langle\phi_\mu(\vec{r}_i)\left|\sum_A^N\frac{Z_A}{r_{iA}}\right|\phi_\mu(\vec{r}_i)\right\rangle \\ &\quad + \sum_{i=1}^{n/2}\sum_{j=1}^{n/2} 2\left\langle\phi_\mu(\vec{r}_i)\phi_\nu(\vec{r}_j)\left|\frac{1}{r_{ij}}\right|\phi_\mu(\vec{r}_i)\phi_\nu(\vec{r}_j)\right\rangle - \left\langle\phi_\mu(\vec{r}_i)\phi_\nu(\vec{r}_j)\left|\frac{1}{r_{ij}}\right|\phi_\mu(\vec{r}_j)\phi_\nu(\vec{r}_i)\right\rangle \end{aligned} \tag{38}$$

For *unrestricted Hartree-Fock*, where all spin orbitals are allowed to have different spatial extent, the similar *Pople-Nesbet equations* have to be solved:

$$\begin{aligned} \boldsymbol{F^\alpha C^\alpha} &= \boldsymbol{S C^\alpha E^\alpha} \\ \boldsymbol{F^\beta C^\beta} &= \boldsymbol{S C^\beta E^\beta} \end{aligned} \tag{39}$$

where the fock matrix depends on the coefficients of both α- and β-orbitals.

2.4 COMPLETE ACTIVE SPACE SELF-CONSISTENT FIELD

Some chemical systems cannot be described by employing only one Slater determinant. In bond dissociation, for example, the contribution of the bonding configuration decreases while that of the antibonding configuration increases with increasing bond distance. Thus, at elongated bond distances both configurations have to be taken into account for an accurate description of the system. Also, in excited states calculations often several configurations have to be considered. Then, the wavefunction can be approximated by using a linear combination of Slater determinants:[59]

$$|\Psi_{CASSCF}\rangle = \sum_\nu c_\nu\,|\Psi_\nu\rangle \tag{40}$$

where both the coefficients c_ν and the coefficients of the spatial orbitals are optimized.

In CASSCF,[60,61] the orbitals are divided in three categories[59]: The *inactive* orbitals are always doubly occupied while the *secondary* orbitals are always empty. All distributions of electrons in the orbitals of the *active space* are taken into account. Excitations betwen active and inactive or secondary orbitals are not considered. However, during

the calculation, orbitals can be exchanged between the active space and the inactive or secondary orbitals. The number of active orbitals M and the number of active electrons n is indicated by the nomenclature $CASSCF(n, M)$. The choice of the size of the active space as well as of the character of the active orbitals is nontrivial and depends on the chemical nature of the system as well as on the question being investigated. However, the feasible size of the active space is rather limited since the number of configurations N_{conf} for a system with total spin $\mathcal{S}$ grows with the Weyl formula[62]

$$N_{conf} = \frac{2\mathcal{S}+1}{M+1}\binom{M+1}{n/2-\mathcal{S}}\binom{M+1}{n/2+\mathcal{S}+1} \tag{41}$$

In *state-averaged* (SA) CASSCF, the orbitals are not optimized for a single state but for all N_{state} states included in the calculation. A state-average energy function E_{SA}, which is a linear combination of the energies E_i of the N_{state} states with the weights w_i, is employed:

$$E_{SA} = \sum_{i}^{N_{state}} w_i E_i \tag{42}$$

Ususally the weigths of all states are equal to ensure that all states are equally well described. The states obtained by SA-CASSCF are orthogonal. However, the average orbitals obtained this way might be less well suited to describe a given state than orbitals obtained in a state-specific CASSCF calculation. Also, the number of states has to be chosen in accordance with the size of the active space and the character of the active orbitals.

CASSCF is well-suited to describe systems where only a limited number of configurations with large coefficients are important for the description (*static correlation*). However, if a large number of configurations with small coefficients have to be considered (*dynamic correlation*), additional corrections are needed. Perturbational methods like CASPT2[63,64] (Complete Active Space 2nd order Perturbation Theory) and NEVPT2[65–67] (*n*-Electron Valence State Perturbation Theory) are able to introduce dynamical correlation.

2.5 COMPLETE ACTIVE SPACE 2ND ORDER PERTURBATION THEORY

CASPT2[63,64] employs a CASSCF wavefunction and adds perturbational corrections to better describe dynamic correlation. In *perturbation theory*,[68] the problem to be solved is split into an exactly solvable problem and a small perturbation. The addition of the perturbative corrections to the simplyfied system then gives an approximate description of the real target system. Correspondingly, the Hamiltonian is split into the unperturbed *zeroth order* Hamiltonian $\hat{H}^{(0)}$, for which exact solutions can be calculated, and the small perturbation $\hat{H}'$. In CASPT2,[59] the unperturbed wavefunction is a CASSCF wavefunction. The unperturbed Hamiltonian is the *CASSCF Fock operator*

$$\hat{F} = \sum_{ij} \hat{f}_{ij}\hat{E}_{ij} \tag{43}$$

where $\hat{E}_{ij}$ is an excitation operator defined as

$$\hat{E}_{ij} = \hat{a}^{\dagger}_{i\alpha}\hat{a}_{j\alpha} + \hat{a}^{\dagger}_{i\beta}\hat{a}_{j\beta} \tag{44}$$

$\hat{a}^{\dagger}$ and $\hat{a}$ are the *creation* and *annihilation operators*. Thus, $\hat{a}^{\dagger}_{i\alpha}$ and $\hat{a}^{\dagger}_{i\beta}$ create one electron with spin α and one electron with spin β in orbital i whereas $\hat{a}_{j\alpha}$ and $\hat{a}_{j\beta}$ annihilate

two electrons with opposite spin in orbital j. Therefore, the operator $\hat{E}_{ij}$ excites two electrons from orbital j to orbital i. The operator $\hat{f}_{ij}$ can be expressed as

$$\begin{aligned}\hat{f}_{ij} = &\left\langle \phi_i \left| -\frac{1}{2}\nabla^2 \right| \phi_j \right\rangle - \sum_{A=1}^{N} Z_A \left\langle \phi_i \left| \frac{1}{r_A} \right| \phi_j \right\rangle \\ &+ \sum_{ij,kl} D_{ij} \left[\langle \phi_i \phi_j | \phi_k \phi_l \rangle - \frac{1}{2} \langle \phi_i \phi_k | \phi_j \phi_l \rangle \right]\end{aligned} \tag{45}$$

where $\boldsymbol{D}$ is the first-order one-particle density matrix, which can be calculated from the one-electron coupling coefficients

$$D_{ij}^{mn} = \langle \Psi_m | \hat{E}_{ij} | \Psi_n \rangle \tag{46}$$

as

$$D_{ij} = \sum_{mn} c_m^* c_n D_{ij}^{mn} \tag{47}$$

The *first-order interaction space* Φ contains all states which are generated by double excitations from the CASSCF wavefunction into secondary orbitals.

$$\Phi = \hat{E}_{ij}\hat{E}_{kl} \left| \Psi_{CASSCF} \right\rangle \tag{48}$$

After the zeroth-order Hamiltonian and the perturbation have been set up, the perturbation equations can be solved.

If the first-order interaction space contains states for which the eigenvalue of the zeroth-order Hamiltonian is close to the value for the CASSCF wavefunction, the second-order energy can become too large. Such states are termed *intruder states*.[69,70] Ideally, the orbitals contributing to these states should be included into the active space.[71] However, since the size of the active space for which calculations are still feasible is rather limited, an arbitrary *level shift*[69,70] can be added to the zeroth-order Hamiltonian. Then, the second-order energy is corrected by applying a level-shift correction. If no intruder states are present, the effect of the level-shift technique on the second-order energy is negligible.

CASPT2 can be used in a state-specific (SS) or a *multistate* (MS) formalism.

2.6 ALGEBRAIC DIAGRAMMATIC CONSTRUCTION TO 2ND ORDER

The *Algebraic Diagrammatic Construction to 2nd order* (ADC(2))[72] is a perturbational method for the calculation of excitation energies.[73] The basis for this method is the polarization propagator. A *propagator* describes how a perturbation propagates through a system between the times t and t'. The *polarization propagator* describes a perturbation of the electron density. The polarization $P(t)$ can be expressed as[74]

$$P(t) = \sum_{pq} \hat{P}_{pq} \hat{a}_q^\dagger(t) \hat{a}_p(t) \tag{49}$$

where $\hat{P}$ is an arbitrary one-electron operator. Depending on the choice of $\hat{P}$, different phenomena can be described. For example, if $\hat{P}$ is chosen as the Fermi-contact Hamiltonian, indirect nuclear spin-spin coupling constants can be calculated.[75] For the description of electronic excitations, a transition moment operator should be chosen, which is usually the dipole operator.[74] The annihilation and creation operators $\hat{a}_p$ and $\hat{a}_q^\dagger$ annihilate and create an electron in the orbital p and q, respectively. The polarization propagator is defined as

$$\Pi_{pq,rs}(t,t') = -\mathrm{i}\,\Xi(t-t') \langle \Psi_0 | P(t) Q(t') | \Psi_0 \rangle - \mathrm{i}\,\Xi(t-t') \langle \Psi_0 | Q(t') P(t) | \Psi_0 \rangle \tag{50}$$

where $\Xi(t-t')$ is a step function and Ψ_0 is the ground state wavefunction. The polarization propagator gives the probability amplitude that a polarization P of the ground state created at time t evolves to a polarization Q at time t', where Q can be written as

$$Q(t') = \sum_{rs} \hat{Q}_{rs} \hat{a}_r^\dagger(t) \hat{a}_s(t) \tag{51}$$

In the derivation of linear-response based methods as well as methods formulated employing propagators[76] it is often convenient to use the *interaction picture*[77] of quantum mechanics. While in the *Schrödinger picture*[78] operators $\hat{O}_S$ are time-independent and only state vectors $|\Psi_S(t)\rangle$ are time-dependent, in the interaction picture[77] both operators $\hat{O}_I(t)$ and state vectors $|\Psi_I(t)\rangle$ are time-dependent. By transformations it is possible to convert operators from one picture to the other.

$$\hat{O}_I(t) = e^{\mathrm{i}\,\hat{H}t} \hat{O}_s e^{-\mathrm{i}\,\hat{H}t} \tag{52}$$

where $\hat{H}$ is the Hamiltonian in the Schrödinger picture. Converting the time-independent polarization propagator in the Schrödinger picture Π_0 to the time-dependent operator in the interaction picture $\Pi(t)$ is accomplished by[74]

$$\Pi(t) = e^{\mathrm{i}\,\hat{H}t} \Pi_0 e^{-\mathrm{i}\,\hat{H}t} \tag{53}$$

Rewriting equation 50 employing the above expression for the time-dependency and inserting the completeness relation $\sum_i^{N_{exc}} |\Psi_i\rangle \langle\Psi_i| = 1$ gives

$$\begin{aligned} \Pi_{pq,rs}(t,t') = &-\mathrm{i}\,\Xi(t-t') \sum_{i=1}^{N_{exc}} \langle\Psi_0|P|\Psi_i\rangle \langle\Psi_i|Q|\Psi_0\rangle\, e^{\mathrm{i}(t-t')(E_0-E_i)} \\ &-\mathrm{i}\,\Xi(t-t') \sum_{i=1}^{N_{exc}} \langle\Psi_0|Q|\Psi_i\rangle \langle\Psi_i|P|\Psi_0\rangle\, e^{\mathrm{i}(t-t')(E_i-E_0)} \end{aligned} \tag{54}$$

Fourier transformation of the polarization propagator gives the Lehmann representation of the polarization propagator[74]

$$\Pi_{pq,rs}(\omega) = \sum_{i=1}^{N_{exc}} \frac{\langle\Psi_0|\hat{a}_q^\dagger \hat{a}_p|\Psi_i\rangle \langle\Psi_i|\hat{a}_r^\dagger \hat{a}_s|\Psi_0\rangle}{\omega + (E_0^{N_{exc}} - E_i^{N_{exc}}) + \mathrm{i}\,\eta} - \sum_{i=1}^{N_{exc}} \frac{\langle\Psi_0|\hat{a}_r^\dagger \hat{a}_s|\Psi_i\rangle \langle\Psi_i|\hat{a}_q^\dagger \hat{a}_p|\Psi_0\rangle}{\omega - (E_0^{N_{exc}} - E_i^{N_{exc}}) - \mathrm{i}\,\eta} \tag{55}$$

where $E_0 - E_i$ are the excitation energies of the N_{exc} excited states. The polarization propagator has poles at the excitation energies.

Equation 55 can be written in matrix notation as

$$\Pi(\omega) = \Pi^+(\omega) - \Pi^-(\omega) \tag{56}$$

Since $\Pi^+(\omega)$ and $\Pi^-(\omega)$ are related by

$$\Pi^{+\dagger}(-\omega) = -\Pi^-(\omega) \tag{57}$$

only one of these matrices needs to be calculated. The polarization propagator is expressed in the eigenstates of the Hamiltonian. Therefore, equation 55 is termed *diagonal representation*, which can be written as[73]

$$\Pi(\omega) = \boldsymbol{x}^\dagger (\omega \mathbf{1} - \boldsymbol{\Omega})^{-1} \boldsymbol{x} \tag{58}$$

where the matrix elements are calculated as[79]

$$x_{i,rs} = \langle\Psi_i|\hat{a}_r^\dagger \hat{a}_s|\Psi_0\rangle \tag{59}$$

$$\Omega_{ij} = -(E_0^{N_{exc}} - E_i^{N_{exc}})\delta_{ij} \tag{60}$$

$\mathbf{\Omega}$ is a diagonal matrix containing the excitation energies ω_i while $\boldsymbol{x}$ contains the transition amplitudes.

For the calculation of the excitation energies, $\mathbf{\Pi}^+$ has to be brought into a non-diagonal form according to

$$\mathbf{\Pi}^+(\omega) = \boldsymbol{f}^\dagger(\omega\mathbf{1} - \boldsymbol{M})^{-1}\boldsymbol{f} \tag{61}$$

$\boldsymbol{M}$ is the energy-shifted Hamiltonian[79] with the matrix elements

$$M_{IJ} = \langle\Psi_I|\hat{H} - E_0|\Psi_J\rangle \tag{62}$$

where E_0 is the ground-state energy and Ψ_I and Ψ_J are the wavefunctions of the excited states I and J. These wavefunctions usually correspond to the orthogonalized eigenstates of the Hamiltonian for which $\boldsymbol{M}$ is diagonal.

$\boldsymbol{f}$ are the spectral amplitude vectors

$$f_{pq,I} = \langle\Psi_I|\hat{a}_p^\dagger\hat{a}_q|\Psi_0\rangle \tag{63}$$

where Ψ_0 is the ground state wavefunction and the effect of the creation and annihilation operators $\hat{a}_p^\dagger$ and $\hat{a}_q$ is the excitation of an electron from orbital q to orbital p. The excited state wavefunctions can be obtained by carrying out a Møller-Plesset[80] (MP) perturbational calculation of the desired (usually second) order to obtain the ground state wavefunction and then acting on Ψ_0 with excitation operators generating single, double and, if wanted, higher excitations.[79] In this way, an ADC(i) calculation can be carried out by starting with an MPi computation.

The Hamiltonian and the transition amplitudes are expanded in a perturbational series.[73]

$$\boldsymbol{M} = \boldsymbol{M}^{(0)} + \boldsymbol{M}^{(1)} + \boldsymbol{M}^{(2)} + \boldsymbol{M}^{(3)} + \cdots \tag{64}$$

$$\boldsymbol{f} = \boldsymbol{f}^{(0)} + \boldsymbol{f}^{(1)} + \boldsymbol{f}^{(2)} + \boldsymbol{f}^{(3)} + \cdots \tag{65}$$

Thus, the polarization propagator can be written as

$$\begin{aligned}\mathbf{\Pi}^+(\omega) = (\boldsymbol{f}^{(0)\dagger} + \boldsymbol{f}^{(1)\dagger} + \boldsymbol{f}^{(2)\dagger} + \cdots)(\omega\mathbf{1} - \boldsymbol{M}^{(0)} - \boldsymbol{M}^{(1)} \\ -\boldsymbol{M}^{(2)} - \cdots)^{-1}(\boldsymbol{f}^{(0)} + \boldsymbol{f}^{(1)} + \boldsymbol{f}^{(2)} + \cdots)\end{aligned} \tag{66}$$

Then, the matrix expressions can be ordered according to the order of expansion. The zeroth and first order terms are:[72]

$$\Pi^{(0)}(\omega) = \boldsymbol{f}^{(0)\dagger}(\omega\mathbf{1} - \boldsymbol{M}^{(0)})^{-1}\boldsymbol{f}^{(0)} \tag{67}$$

$$\begin{aligned}\Pi^{(1)}(\omega) = \boldsymbol{f}^{(1)\dagger}(\omega\mathbf{1} - \boldsymbol{M}^{(0)})^{-1}\boldsymbol{f}^{(0)} + \boldsymbol{f}^{(0)\dagger}(\omega\mathbf{1} - \boldsymbol{M}^{(0)})^{-1}\boldsymbol{f}^{(1)} \\ + \boldsymbol{f}^{(0)\dagger}(\omega\mathbf{1} - \boldsymbol{M}^{(0)})^{-1}\boldsymbol{M}^{(1)}(\omega\mathbf{1} - \boldsymbol{M}^{(0)})^{-1}\boldsymbol{f}^{(0)}\end{aligned} \tag{68}$$

The second order terms are:

$$\begin{aligned}\Pi^{(2)}(\omega) = \boldsymbol{f}^{(1)\dagger}(\omega\mathbf{1} - \boldsymbol{M}^{(0)})^{-1}\boldsymbol{f}^{(1)} + \boldsymbol{f}^{(1)\dagger}(\omega\mathbf{1} - \boldsymbol{M}^{(0)})^{-1}\boldsymbol{M}^{(1)}(\omega\mathbf{1} - \boldsymbol{M}^{(0)})^{-1}\boldsymbol{f}^{(0)} + c.c. \\ + \boldsymbol{f}^{(0)\dagger}(\omega\mathbf{1} - \boldsymbol{M}^{(0)})^{-1}\boldsymbol{M}^{(1)}(\omega\mathbf{1} - \boldsymbol{M}^{(0)})^{-1}\boldsymbol{M}^{(1)}(\omega\mathbf{1} - \boldsymbol{M}^{(0)})^{-1}\boldsymbol{f}^{(0)} \\ + \boldsymbol{f}^{(0)\dagger}(\omega\mathbf{1} - \boldsymbol{M}^{(0)})^{-1}\boldsymbol{M}^{(2)}(\omega\mathbf{1} - \boldsymbol{M}^{(0)})^{-1}\boldsymbol{f}^{(0)} + \boldsymbol{f}^{(2)\dagger}(\omega\mathbf{1} - \boldsymbol{M}^{(0)})^{-1}\boldsymbol{f}^{(0)} + c.c.\end{aligned} \tag{69}$$

where *c.c.* denotes the complex conjugate of the preceding term.

Different ADC(i) approximation schemes with truncation of the expansion at order i are possible.[73] The most commonly used method ADC(2) includes terms up to second order.

By diagrammatic analysis, explicit algebraic expressions can be derived. For example, the zeroth-order terms can be calculated as

$$\Pi^{(0)} = \sum_{jk} \underbrace{D^*_{jk}}_{\boldsymbol{f}^{(0)\dagger}} \underbrace{\frac{(1-n_j)n_k}{\omega + \varepsilon_k - \varepsilon_j}}_{(\omega \mathbf{1} - \boldsymbol{M}^{(0)})^{-1}} \underbrace{D_{jk}}_{\boldsymbol{f}^{(0)}} \tag{70}$$

where D_{jk} means the matrix element $\langle \varphi_j | \hat{d} | \varphi_k \rangle$ with $\hat{d}$ being the dipole operator, n_i is the occupation number of orbital i and ε_i is its energy.

Then, the matrix $\boldsymbol{M}$, truncated at the chosen order, can be diagonalized, which corresponds to solving the eigenvalue problem

$$\boldsymbol{M}\boldsymbol{Y} = \boldsymbol{Y}\boldsymbol{\Omega} \tag{71}$$

From the eigenvectors $\boldsymbol{Y}$ the spectroscopic amplitudes $\boldsymbol{x}$ can be calculated as

$$\boldsymbol{x} = \boldsymbol{y}^\dagger \boldsymbol{f} \tag{72}$$

2.7 DENSITY FUNCTIONAL THEORY

2.7.1 *Ground state density functional theory*

In density functional theory[81] (DFT) the central quantity is the electron density $\rho(\vec{r})$. Like the wavefunction, the electron density contains all information that can be known about a system: it integrates to the number of electrons and contains information about the position and charge of the nuclei. According to the first Hohenberg-Kohn theorem,[82] the electron density uniquely determinates the Hamilton operator[81] and thus all properties of the system, including the energy of the ground state as well as the energy of excited states. The ground state energy can be divided into parts depending on the actual system (i. e. the attraction between nuclei and electrons) and parts whose form is independent of the number of electrons as well as the position and charge of the nuclei:

$$E[\rho] = \underbrace{T[\rho] + E_{ee}[\rho]}_{\text{universally valid}} + \underbrace{E_{en}[\rho]}_{\text{system dependent}} = F_{\mathrm{HK}}[\rho] + E_{en}[\rho] \tag{73}$$

The system-independent parts are collected into the *Hohenberg-Kohn functional* F_{HK}. According to the second Hohenberg-Kohn theorem, the energy of a trial electron density calculated with the exact Hohenberg-Kohn functional is greater than the exact ground state energy, unless the trial density equals the true ground-state density. However, this variational principle is only valid for the exact Hohenberg-Kohn functional, which unfortunately is not known. Several approximate functionals have been developed. Most of them employ the *Kohn-Sham approach*, in which a reference system of non-interacting electrons with the same electron density as the real system is assumed. The Hamilton operator $\hat{H}_S$ of this non-interacting system contains an effective potential $V_S(\vec{r}_i)$ in order to generate the same electron density as the interacting system.

$$\hat{H}_S = -\frac{1}{2}\sum_{i=1}^{n} \nabla_i^2 + \sum_{i=1}^{n} V_s(\vec{r}_i) \tag{74}$$

The ground state wavefunction is described by one single Slater determinant. By employing the *Kohn-Sham operator*

$$\hat{f}^{\mathrm{KS}} = -\frac{1}{2}\nabla^2 + V_S(\vec{r}) \tag{75}$$

the *Kohn-Sham orbitals* φ_i^{KS} are calculated, analogously as in the Hartree-Fock method.

$$\hat{f}^{\mathrm{KS}}\varphi_i^{KS} = \varepsilon_i \varphi_i^{KS} \tag{76}$$

Then, the electron density is calculated from the Kohn-Sham orbitals as

$$\rho(\vec{r}) = \sum_{i=1}^{k} |\varphi_i^{KS}|^2 \tag{77}$$

The kinetic energy of the non-interacting system can then be calculated as

$$T_S = -\frac{1}{2}\sum_{i=1}^{k} \langle \varphi_i^{KS} | \nabla^2 | \varphi_i^{KS} \rangle \tag{78}$$

The Hohenberg-Kohn functional is separated into three parts:

$$F_{\mathrm{HK}}[\rho] = T_S[\rho] + J[\rho] + F_{\mathrm{XC}}[\rho] \tag{79}$$

where $J[\rho]$ decribes the Coulomb repulsion between the electrons. The unknown quantities about the system are collected into the *exchange-correlation functional* $F_{\mathrm{XC}}[\rho]$, which is used to approximately describe the non-classical effects of exchange and correlation (the dependency of the probability density of one electron on the probability density of all other electrons), self-interaction correction and the part of the kinetic energy that is not captured by the kinetic energy of the non-interacting system. The Kohn-Sham operator is then

$$\hat{f}^{\mathrm{KS}} = \underbrace{-\frac{1}{2}\nabla_i^2}_{T_{\mathrm{S}}} \underbrace{- \sum_{A=1}^{N} \frac{Z_A}{r_{iA}}}_{V_{en}} + \underbrace{\int \frac{\rho(\vec{r}')}{|\vec{r}_i - \vec{r}'|}\, dr'}_{J} + \underbrace{\frac{\partial E_{\mathrm{XC}}[\rho(\vec{r})]}{\partial \rho(\vec{r})}}_{F_{\mathrm{XC}}} \tag{80}$$

where $E_{XC}[\rho(\vec{r})]$ is the *exchange-correlation energy*. Thus, the energy of the real, interacting system is

$$E[\rho(\vec{r})] = \underbrace{-\frac{1}{2}\sum_{i=1}^{k} \langle \varphi_i^{KS} | \nabla^2 | \varphi_i^{KS} \rangle}_{T_S} \underbrace{- \sum_{A=1}^{N} \frac{Z_A}{R_A} \int \frac{\rho(\vec{r})}{R_A}\, dr}_{E_{en}} \underbrace{+ \frac{1}{2} \iint \frac{\rho(\vec{r})\rho(\vec{r}')}{|\vec{r} - \vec{r}'|}\, dr dr'}_{J} + E_{XC}[\rho(\vec{r})] \tag{81}$$

Many exchange-correlation functionals at different levels of accuracy have been proposed,[83] but there is no way to improve the functionals in a systematic way.

2.7.2 *Time-dependent density functional theory*

The foundation for the calculation of excited states with density functional theory is the *Runge-Gross theorem*,[84] which states that the time-dependent electron density $\rho(\vec{r}, t)$ determines the time-dependent wavefunction $\Psi(\vec{r}, t)$ up to a time-dependent phase.[85] Thus, all observable properties can be deduced from the time-dependent density.[86]

In this section, some important definitions of linear response theory will be briefly outlined. Then, the application of linear response theory to the electron density and to a non-interacting reference system, as in the Kohn-Sham method, will be shown. Finally, the Casida equation will be discussed and a commonly used approximation will be introduced.

Linear response theory

Linear response theory is a perturbational theoretical ansatz with the goal to describe how an observable changes when a small time-dependent perturbation acts on a system.

The ground state expectation value of an observable α is $\alpha_0 = \langle \Psi_0 | \hat{\alpha} | \Psi_0 \rangle$, where Ψ_0 is the ground state wavefunction. At $t = t_0$, a time-dependent perturbation $\hat{H}_1$ consisting of an external field $F_{ext}(t)$ coupled to an observable β[86]

$$\hat{H}_1 = F_{ext}(t)\hat{\beta} \tag{82}$$

perturbs the system and affects the wavefunction. Thus, the expectation value of α becomes time-dependent: $\alpha(t) = \langle \Psi(t) | \hat{\alpha} | \Psi(t) \rangle$.

The *response* of $\hat{\alpha}$ is $\alpha(t) - \alpha_0$, i. e. the difference between the time-dependent and the ground-state expectation value. It can be expanded in powers of the external field:

$$\alpha(t) - \alpha_0 = \alpha_1(t) + \alpha_2(t) + \alpha_3(t) + \cdots \tag{83}$$

The *linear response* is the first order response, $\alpha_1(t)$. The linear response of $\hat{\alpha}$ at time t to a perturbation that has occured at an earlier time t' can be calculated as

$$\alpha_1(t) = -\,\mathrm{i} \int_{t_0}^{t} F_{ext}(t') \, \langle \Psi_0 | [\hat{\alpha}(t - t'), \hat{\beta}] | \Psi_0 \rangle \, dt' \tag{84}$$

where i denotes the imaginary unit and $[\hat{\alpha}, \hat{\beta}]$ is the commutator of the operators $\hat{\alpha}$ and $\hat{\beta}$. Equation 84 can be rewritten as

$$\alpha_1(t) = \int_{-\infty}^{\infty} \chi_{\alpha\beta}(t - t') F_{ext}(t') dt' \tag{85}$$

where the integration limit t_0 can be replaced by $-\infty$ since the external potential is zero before t_0, and $\chi_{\alpha\beta}$ is the *retarded response function*, which is defined as

$$\chi_{\alpha\beta}(t - t') = -\,\mathrm{i}\, \Xi(t - t') \, \langle \Psi_0 | [\hat{\alpha}(t - t'), \hat{\beta}] | \Psi_0 \rangle \tag{86}$$

where $\Xi(t - t')$ denotes a step function corresponding to the fact that the perturbation occured earlier than the response.

Linear response of the electron density

Let $u(\vec{r}, t)$ be a time-dependent potential of the form[86]

$$u(\vec{r}, t) = u_0(\vec{r}) + u_1(\vec{r}, t)\Xi(t - t_0) \tag{87}$$

u_0 corresponds to the (time-independent) ground state potential, i. e., in the simplest case, the potential due to the positively charged nuclei. $u_1(\vec{r}, t)$ is a small perturbational potential that is switched on at time t_0, which is signified by the step function Ξ.

The *density operator* $\hat{\rho}(\vec{r})$ is defined as

$$\hat{\rho}(\vec{r}) = \sum_{i=1}^{n} \delta(\vec{r} - \vec{r}_i) \tag{88}$$

where the δ-function does not vanish at the position of the electrons $\vec{r}_i$. The density operator gives the electron density when operating on the wavefunction:

$$\rho(\vec{r}) = \langle \Psi | \hat{\rho}(\vec{r}) | \Psi \rangle \tag{89}$$

If the perturbation is a scalar potential $u_1(\vec{r}', t')$ coupling to the density operator,

$$\hat{H}_1(t) = \int u_1(\vec{r}', t') \hat{\rho}(\vec{r}') \, d^3 r' \tag{90}$$

the first-order density-density response is

$$\rho_1(\vec{r},t) = \int_{-\infty}^{\infty} dt' \int \chi_{\rho\rho}(\vec{r},\vec{r}',t-t')u_1(\vec{r}',t')d^3r' \tag{91}$$

with the density-density response function being:

$$\chi_{\rho\rho}(\vec{r},\vec{r}',t-t') = -\mathrm{i}\,\Xi(t-t')\,\langle\Psi_0|[\rho(\vec{r},t-t'),\rho(\vec{r}')]|\Psi_0\rangle \tag{92}$$

where $[\rho(\vec{r},t-t'),\rho(\vec{r}')]$ signifies the commutator. Picturesquely, equation 91 can be imagined in the following way: several perturbances $u_1(\vec{r}',t')$ are carried out at positions $\vec{r}'$ at time t', each of them influencing the whole electron density at all $\vec{r}$. Therefore, the retarded response functions due to these small perturbations have to be integrated over space.

As in the general case (equation 83), the response of the density can be expanded as a Taylor series in powers of the perturbation

$$\rho(\vec{r},t) - \rho_0(\vec{r}) = \rho_1(\vec{r},t) + \rho_2(\vec{r},t) + \rho_3(\vec{r},t) + \cdots \tag{93}$$

Thus, the density-density response function can be expressed as

$$\chi_{\rho\rho}(\vec{r},\vec{r}',t,t') = \left.\frac{\delta\rho[u](\vec{r},t)}{\delta u(\vec{r}',t')}\right|_{u_0(\vec{r})} \tag{94}$$

where δ signifies the functional derivative. The initial potential u_0 corresponds to the ground state and is, according to the first Hohenberg-Kohn theorem, a functional of the density. Since the Taylor series is evaluated around u_0, i. e. the ground state potential, the linear response function is a functional of the ground state density and not of the perturbed density.

Lehmann representation of the linear response function

The time-dependent linear response function can by Fourier transformation be expressed as a frequency-dependent linear response function. Fourier transformation of equation 86 gives[86]

$$\chi_{\alpha\beta}(\omega) = -\mathrm{i}\int_{-\infty}^{\infty} \Xi(t)\,\langle\Psi_0|[\hat{\alpha}(t),\hat{\beta}]|\Psi_0\rangle\, e^{\mathrm{i}\,\omega t}\,dt \tag{95}$$

Employing the *completeness relation*

$$\sum_{i=0}^{\infty} |\Psi_i\rangle\,\langle\Psi_i| = 1 \tag{96}$$

where Ψ_i are the eigenfunctions of the Hamiltonian with the energy differences $E_i - E_0$ corresponding to the excitation energies Ω_i, equation 95 can be written as

$$\chi_{\alpha\beta}(\omega) = -\mathrm{i}\sum_{i=1}^{\infty}\int_{-\infty}^{\infty} \Xi(t)e^{\mathrm{i}\,\omega t}\left\{\langle\Psi_0|\hat{\alpha}|\Psi_i\rangle\,\langle\Psi_i|\hat{\beta}|\Psi_0\rangle\, e^{-\mathrm{i}\,\Omega_i t} - \langle\Psi_0|\hat{\beta}|\Psi_i\rangle\,\langle\Psi_i|\hat{\alpha}|\Psi_0\rangle\, e^{\mathrm{i}\,\Omega_i t}\right\} dt \tag{97}$$

Since the step function can be expressed as

$$\Xi(t) = \lim_{\eta\to 0^+}\frac{\mathrm{i}}{2\pi}\int_{-\infty}^{\infty}\frac{e^{-\mathrm{i}\,\omega t}}{\omega+\mathrm{i}\,\eta}\,d\omega \tag{98}$$

the *Lehmann representation* of the linear response function can be written as

$$\chi_{\alpha\beta}(\omega) = \lim_{\eta\to 0^+}\sum_{i=1}^{\infty}\left\{\frac{\langle\Psi_0|\hat{\alpha}|\Psi_i\rangle\,\langle\Psi_i|\hat{\beta}|\Psi_0\rangle}{\omega-\Omega_i+\mathrm{i}\,\eta} - \frac{\langle\Psi_0|\hat{\beta}|\Psi_i\rangle\,\langle\Psi_i|\hat{\alpha}|\Psi_0\rangle}{\omega+\Omega_i+\mathrm{i}\,\eta}\right\} \tag{99}$$

where $\hat{\beta}$ is the operator the perturbation couples to while $\hat{\alpha}$ is the operator whose linear response is of interest.

The Lehmann representation of the density-density response function is then

$$\chi_{\rho\rho}(\vec{r},\vec{r}',\omega) = \lim_{\eta\to 0^+} \sum_{i=1}^{\infty} \left\{ \frac{\langle\Psi_0|\hat{\rho}(\vec{r})|\Psi_i\rangle\,\langle\Psi_i|\hat{\rho}(\vec{r}')|\Psi_0\rangle}{\omega-\Omega_i+\mathrm{i}\,\eta} - \frac{\langle\Psi_0|\hat{\rho}(\vec{r}')|\Psi_i\rangle\,\langle\Psi_i|\hat{\rho}(\vec{r})|\Psi_0\rangle}{\omega+\Omega_i+\mathrm{i}\,\eta} \right\} \tag{100}$$

where the notation $\vec{r}'$ denotes the spatial coordinates of the perturbation coupling to the density operator $\hat{\rho}(\vec{r}')$ while the linear response of the density operator $\hat{\rho}$ at all positions $\vec{r}$ is of interest. From equation 100 it can be seen that $\chi_{\rho\rho}$ has poles at the excitation energies Ω.

Time-dependent Kohn Sham

The time-dependent Kohn-Sham method can be used to (in principle, exactly) model the evolution of a system in time, similarly to a solution of the time-dependent Schrödinger equation; however, solving the time-dependent Kohn-Sham equations is not necessary for the computation of the excitation energies since, instead, a perturbational theoretical ansatz is used. Therefore, in the following subsection only the necessary aspects of time-dependent Kohn-Sham method will be discussed.

According to the *van Leeuwen theorem*,[87] a noninteracting reference system with the same time-dependent electron density $\rho_S(\vec{r},t)$ as the real system can be constructed, comparable to the time-independent Kohn-Sham method. This reference system is described by one single Slater determinant, from which its density is calculated as[86]

$$\rho(\vec{r},t) = \rho_S(\vec{r},t) = \sum_{i=1}^{n} |\varphi_i(\vec{r},t)|^2 \tag{101}$$

Since the external potential $u_1(\vec{r}',t')$ is time-dependent, the Kohn-Sham orbitals $\varphi_i(\vec{r},t)$ are now also time-dependent. The effective potential for this non-interacting system is

$$u_s[\rho](\vec{r},t) = u(\vec{r},t) + \int \frac{\rho(\vec{r}',t)}{|\vec{r}-\vec{r}'|} d^3r' + u_{XC}[\rho](\vec{r},t) \tag{102}$$

Conversely, the time-dependent density can be expressed as a functional of the effective potential, which is itself a functional of the external potential:

$$\rho(\vec{r},t) = \rho[u_S[u]](\vec{r},t) \tag{103}$$

where the potential u contains the time-independent ground state potential u_0 and the time-dependent potential u_1 (see equation 87). As in equation 93, the time-dependent density response can be expanded in powers of the effective potential, where the first-order term is

$$\rho_1(\vec{r},t) = \int_{-\infty}^{\infty} dt' \int \chi_{\rho\rho,S}(\vec{r},t,\vec{r}',t') u_{S1}(\vec{r}',t') d^3r' \tag{104}$$

which is the linear response equation of TDDFT, where

$$\chi_{\rho\rho,S}(\vec{r},\vec{r}',t,t') = \left.\frac{\delta\rho[u_S](\vec{r},t)}{\delta u_S(\vec{r}',t')}\right|_{u_S[\rho_0](\vec{r})} \tag{105}$$

The first-order effective potential is

$$u_{S1}[\rho](\vec{r},t) = u_1(\vec{r},t) + \int \frac{\rho_1(\vec{r}',t)}{|\vec{r}-\vec{r}'|} d^3r' + u_{XC1}(\vec{r},t) \tag{106}$$

where u_{XC1} is the linearized exchange-correlation potential

$$u_{XC1}(\vec{r},t) = \int dt' \int \left.\frac{\delta u_{XC}[\rho](\vec{r},t)}{\delta\rho(\vec{r}',t')}\right|_{\rho_0(\vec{r})} \rho_1(\vec{r}',t') d^3r' \tag{107}$$

with the time-dependent exchange-correlation kernel

$$f_{XC}(\vec{r},t,\vec{r}',t') = \left.\frac{\delta u_{XC}[\rho](\vec{r},t)}{\delta\rho(\vec{r}',t')}\right|_{\rho_0(\vec{r})} \tag{108}$$

Then, a Fourier transformation is carried out to obtain a frequency-dependent exchange-correlation kernel.

Whereas the exact exchange-correlation kernel is frequency-dependent, TDDFT most often uses the *adiabatic approximation*, i. e. a non-frequency dependent exchange-correlation kernel is used. In temporal space, this corresponds to using an exchange-correlation kernel that depends only on the instantaneous time-dependent density while the exact exchange-correlation kernel depends also on the density at all earlier times.

By construction, the density response of the non-interacting system (equation 104) is equal to the density response of the real, interacting system (equation 91). Since the effective potential depends on the response of the density, as can be seen from equations 106 and 107, but the density response depends on the effective potential, as can be seen from equation 104, it can only be calculated iteratively. A Fourier transformation of the Kohn-Sham response function can be carried out, giving

$$\chi_{S,\rho\rho'}(\vec{r},\vec{r}',\omega) = \sum_{j,k=1}^{\infty}(f_k - f_j)\frac{\varphi_j^0(\vec{r})\varphi_k^{0*}(\vec{r})\varphi_j^{0*}(\vec{r}')\varphi_k^0(\vec{r}')}{\omega - \omega_{jk} + \mathrm{i}\,\eta} \tag{109}$$

To ensure that only terms with one occupied and one unoccupied orbital contribute, the factor $(f_k - f_j)$ is used, where f_j and f_k are the occupation numbers of the spin orbitals in the ground state (1 or 0). ω_{jk} is the difference between orbital energies

$$\omega_{jk} = \varepsilon_j - \varepsilon_k \tag{110}$$

When ω goes to ω_{jk}, the denominator goes to zero. Therefore, the linear response function has poles at the frequencies corresponding to the excitation energies of the system.

Analogously to the spin-independent formulation described above, the linear response of the Kohn-Sham density can be formulated in an explicitely spin-dependent way.

The Casida equation

The linear response of the spin density without an external perturbation is[86]

$$\rho_{1\sigma}(\vec{r},\Omega) = \sum_{\sigma'\sigma''}\int \chi_{S,\sigma\sigma'}(\vec{r},\vec{r}',\Omega)d^3r' \int\left\{\frac{1}{|\vec{r}'-\vec{r}''|} + f_{XC,\sigma'\sigma''}(\vec{r}',\vec{r}'',\Omega)\right\}\rho_{1\sigma''}(\vec{r}'',\Omega)\,d^3r'' \tag{111}$$

σ describes the spin-dependence of the quantities. This equation has the form of an eigenvalue equation: A frequency-dependent integral operator acts on $\rho_{1\sigma}(\vec{r},\Omega)$. Those frequencies Ω, which give an eigenvalue of 1, are the excitation energies. From this equation, the *Casida equation*[88] can be derived:[86]

$$\begin{bmatrix}\mathbf{A} & \mathbf{B}\\ \mathbf{B} & \mathbf{A}\end{bmatrix}\begin{bmatrix}\mathbf{X}\\ \mathbf{Y}\end{bmatrix} = \Omega\begin{bmatrix}-1 & 0\\ 0 & 1\end{bmatrix}\begin{bmatrix}\mathbf{X}\\ \mathbf{Y}\end{bmatrix} \tag{112}$$

where the elements of the matrices **A** and **B** are calculated as

$$A_{ia\sigma,i'a'\sigma'}(\Omega) = \delta_{ii'}\delta_{aa'}\delta_{\sigma\sigma'}\omega_{a'i'\sigma'} + B_{ia\sigma,i'a'\sigma'} \tag{113}$$

$$B_{ia\sigma,i'a'\sigma'}(\Omega) = \int d^3r\int d^3r'\varphi_{i\sigma}^*(\vec{r})\varphi_{a\sigma}(\vec{r})\left(\frac{1}{|\vec{r}-\vec{r}'|} + f_{XC\sigma\sigma'}(\vec{r},\vec{r}',\omega)\right)\varphi_{i'\sigma'}(\vec{r}')\varphi_{a'\sigma'}^*(\vec{r}') \tag{114}$$

where the subscripts i and a denote occupied and unoccupied orbitals, respectively.

In the commonly applied *Tamm-Dancoff approximation* (TDA), the matrix elements of **B**, which correspond to deexcitations, are set to zero.

In practice, in TDDFT often the density functionals developed for ground state calculations are also employed for the calculation of excited states.[86] For a better description of charge-transfer states, *range-separated functionals*[89–92] can be used, which use two different expressions for the calculation of the Coulomb interaction for short and long distances and thus give the correct asymptotic behaviour, i. e. the potential falls of as r^{-1} and not exponentially fast.

2.8 DESCRIPTION OF ENVIRONMENT

Employing molecular mechanics (MM), calculations on systems containing several hundred thousand atoms can be carried out. With quantum mechanics (QM), such calculations are unfeasible. In order to include a description of a larger environment in an *ab initio* calculation, different approaches to combine a QM calculation of the chromophore with a classical simulation of the solvent can be used. In *hybrid Quantum Mechanics/Molecular Mechanics*[93–96] (QM/MM) models the environment is described with atomistic resolution employing force fields. In QM/continuum models, such as apparent surface charge (ASC) methods, the environment is described as a dielectric continuum.[97–99] In the most commonly used *additive* approach in QM/classical calculations, the total energy of the system E_S is calculated from three parts:[100]

$$E_S = E_C(QM) + E_{EN}(classical) + E_{C/EN} \tag{115}$$

The energy of the chromophore E_C is calculated employing a quantum chemical method while the energy of the environment E_{EN} is computed classically. In QM/MM calculations E_{EN} is calculated from a force field as described in Section 2.1.2 while in QM/continuum calculations this term is neglected. The interaction between chromophore and environment $E_{C/EN}$ can be described at different levels of accuracy. Usually only electrostatic interactions between environment and chromophore are considered at QM level. For QM/MM calculations van der Waals and repulsion interactions between pairs of atoms in the QM and MM region are described by a Lennard-Jones potential (see equation 15) and in QM/continuum calculations empirical corrections are used.[99]

For both QM/MM and QM/continuum approaches, $E_C(QM)$ and $E_{C/EN}$ are calculated together by employing in the QM calculation an effective Hamiltonian H^{eff} that contains the Hamiltonian of the chromophore $\hat{H}_C^0$ and the classically treated charges q from the environment[100]

$$\hat{H}^{eff} = \hat{H}_C^0 + \sum_i q_i(\vec{\mathcal{R}}_i)\hat{V}(\vec{\mathcal{R}}_i) \tag{116}$$

where $\hat{V}(\vec{\mathcal{R}}_i)$ is the electrostatic potential the chromophore exerts on the environment charges.

In QM/MM, in the *electrostatic embedding* approach, the one used here, the MM point charges are included in the quantum mechanical Hamiltonian by adding a one-electron term of the form:[93]

$$\hat{H}_{C/EN} = -\sum_i^n \sum_\alpha^L \frac{q_\alpha}{|\vec{r}_i - \vec{R}_\alpha|} + \sum_A^N \sum_\alpha^L \frac{q_\alpha Z_A}{|\vec{R}_A - \vec{R}_\alpha|} \tag{117}$$

The first term describes the electrostatic attraction between the n quantum mechanically treated electrons at positions $\vec{r}_i$ and the L MM point charges q_α at positions $\vec{R}_\alpha$.

The second term contains the electrostatic repulsion between the N QM nuclei with charge Z_A at $\vec{R}_A$ and the MM point charges. By including this term in the QM Hamiltonian, the polarization of the electron density due to the presence of the MM charges is taken into account. However, with the commonly employed nonpolarizable force fields it is not possible to take into account the polarization of the environment due to the chromophore. While electrostatic embedding has been used for accurate calculations of biomolecules, *overpolarization* can occur when the distance between MM point charges and the QM electron density becomes small since at short distances the point charge does not accurately model the effects of the more spread-out charge distribution.[94] Overpolarization is exacerbated if the distance between MM point charges and the QM electron density decreases and if the electron density is spatially flexible due to the use of a larger basis set including polarization and diffuse functions.[93]

In QM/continuum approaches the chromophore is placed inside a cavity surrounded by a polarizable continuum representing the solvent. To calculate the environment charges at the surface of the cavity, the Poisson equation is employed[100]

$$-\nabla \cdot [\varepsilon_d(\vec{r})\nabla V_{C,EN}(\vec{r})] = 4\pi\rho_C(\vec{r}) \tag{118}$$

which relates the charge distribution of the chromophore ρ_C and the electrostatic potential $V_{C,EN}$ due to both the chromophore and the environment. ε_d is the distance-dependent dielectric constant. With the introduction of a cavity, the permittivity equals one inside the cavity; outside it is the static dielectric constant ε_s of the simulated solvent. The surface of the cavity is divided into small segments with constant charge density. The compensating charges induced by the charge density of the chromophore on the small surface elements are calculated. These point charges $\vec{q}$, which are included in the QM Hamiltonian (Equation 116), can be calculated as[100]

$$\vec{q} = -\boldsymbol{K_{C,s}}\vec{V}_C \tag{119}$$

where the matrix $\boldsymbol{K_{C,s}}$ depends on the geometry of the cavity as well as on ε_s and $\vec{V}_C$ is the electrostatic potential the chromophore exerts on the small surface areas. In the conductor-like polarizable continuum model[101,102] (C-PCM) and the conductor-like screening model[103–105] (COSMO), which differ in the way the elements of $\boldsymbol{K_{C,s}}$ are calculated, the environment is initially described as a conductor with $\varepsilon = \infty$. Then, the surface charges $\vec{q}^*$ are scaled by an empirical function to reflect a finite dielectric constant of the medium.

$$\vec{q} = \frac{\varepsilon_s - 1}{\varepsilon_s + k}\vec{q}^* \tag{120}$$

where k equals 0.5 in COSMO and 0 in the C-PCM model. The surface charges $\vec{q}$ are then included in the Hamiltonian of the chromophore to describe the effect of the dielectric medium on the chromophore. Thus, the solvent-induced changes of the charge density of the chromophore are calculated self-consistently, i. e. the solvent is also polarized by the chromophore.

QM/MM methods are suited to describe explicit interactions with high directionality, such as hydrogen bonding and stacking. However, the electrostatics are not calculated in a self-consistent way since the environment cannot be polarized by the chromophore. In contrast, QM/continuum models describe the electrostatic interactions with bulk solvation well.

2.9 WAVEFUNCTION ANALYSIS

The goal of wavefunction analysis[106] is to achieve an accurate and quantitative analysis of the wavefunction obtained in an electronic structure calculation. In this work, wavefunction analysis was used to characterize excited states as local excitations or

charge-transfer states, for which also the root mean square electron-hole separation was calculated for further analysis.

To facilitate comparisons between different quantum chemical methods, the *density matrix* is calculated from the wavefunction. Then, different properties can be calculated from it. The elements of the *reduced one-particle transition density matrix* between the states I and J can be calculated as

$$D_{\mu\nu}^{IJ} = \langle \Psi^I | \hat{a}_\mu^\dagger \hat{a}_\nu | \Psi^J \rangle \tag{121}$$

where the annihilation operator $\hat{a}_\nu$ annihilates the electron in orbital χ_ν while the creation operator $\hat{a}_\mu^\dagger$ creates an electron in orbital χ_μ. For $I = J$, the resulting matrix is termed *state density matrix*. The expectation value of an one-electron operator $\hat{O}$ can be calculated directly from the density matrix:

$$\langle \Psi^I | \hat{O} | \Psi^J \rangle = \sum_{\mu\nu} D_{\mu\nu}^{IJ} \langle \chi_\mu | \hat{O} | \chi_\nu \rangle \tag{122}$$

The excited state can be considered as consisting of an electron at position $\vec{r}_e$ and a hole at position $\vec{r}_h$. The two-particle wavefunction χ_{exc} describes the correlated movement of the electron and the hole. The expectation value of an operator acting on the electron-hole wavefunction can be calculated as

$$\langle \hat{O} \rangle_{exc} = \frac{\langle \chi_{exc} | \hat{O} | \chi_{exc} \rangle}{\langle \chi_{exc} | \chi_{exc} \rangle} \tag{123}$$

The *one-particle transition density matrix* γ^{0I} between the ground state and the excited state I in coordinate space is

$$\gamma^{0I}(\vec{r}_h, \vec{r}_e) = \sum_{ij} \psi_i^*(\vec{r}_h) \underbrace{\langle \Psi_0 | \hat{a}_i^\dagger \hat{a}_j | \Psi_I \rangle}_{D_{\mu\nu}^{0I}} \psi_j(\vec{r}_e) \tag{124}$$

To facilitate the distinction between local excitations and charge-transfer states, the system is divided into fragments, e. g. by defining the chromophore as one fragment and the solvent molecules as the second fragment. For illustration, a depiction of the transition density matrix for a system consisting of four fragments is depicted in Figure 3. The elements of the transition density matrix are ordered into blocks corresponding to the fragments. Local excitations occur within the diagonal blocks (blue) while charge-transfer transitions occur in the off-diagonal blocks.

The *charge-transfer number* $\Omega_{AB}^{\mathrm{CT}}$

$$\Omega_{AB}^{\mathrm{CT}} = \int_A \int_B \gamma^{0I}(\vec{r}_h, \vec{r}_e)^2 \, dr_h dr_e \tag{125}$$

describes the probability that the hole is located in fragment A whereas the electron is located in fragment B.

The charge-transfer number is calculated from contributions of the single atoms of the fragments. Employing the Mulliken population analysis scheme,[107] it can be calculated as[106]

$$\Omega_{AB}^{\mathrm{CT}} = \frac{1}{2} \sum_{\mu \in A} \sum_{\nu \in B} [(\mathbf{D}^{0I}\mathbf{S})_{\mu\nu} (\mathbf{S}\mathbf{D}^{0I})_{\mu\nu} + D_{\mu\nu}^{0I} (\mathbf{S}\mathbf{D}^{0I}\mathbf{S})_{\mu\nu}] \tag{126}$$

where the elements of the matrix $\mathbf{S}$ are[108]

$$S_{\mu\nu} = \int \chi_\mu(\vec{r}) \chi_\nu(\vec{r}) \, dr \tag{127}$$

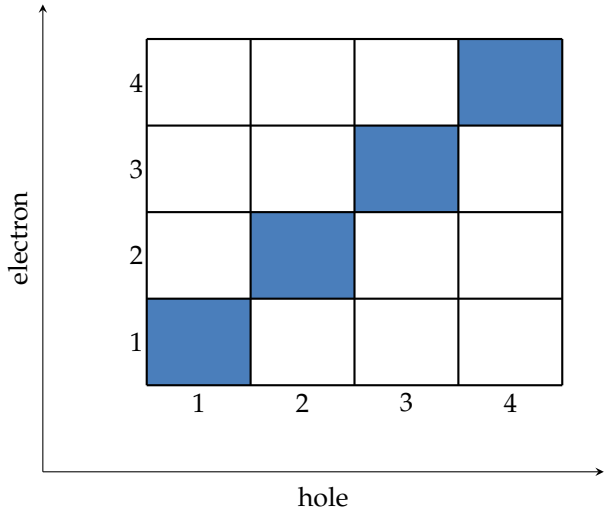

Figure 3. Representation of the transition density matrix of a system comprised of four fragments. Local excitations (blue) correspond to the diagonal elements while charge-transfer states (white) correspond to the off-diagonal elements.

and thus give the overlap between the basis functions. The sum of the charge-transfer numbers over all fragments gives the norm of the exciton wavefunction Ω_{exc},[109]

$$\sum_{A,B} \Omega_{AB}^{\mathrm{CT}} = \Omega_{exc} = \langle \chi_{exc} | \chi_{exc} \rangle \tag{128}$$

which corresponds to the amount of single excitation character of an excited state. For normalized wavefunctions $0 \leq \Omega_{exc} \leq 1$.

The average positions of the initial ($\mathrm{POS_I}$) and final ($\mathrm{POS_F}$) orbitals, corresponding to the hole and the electron, are calculated as[110]

$$\begin{aligned} \mathrm{POS_I} &= \frac{\sum_A A(\sum_B \Omega_{AB}^{\mathrm{CT}})}{\Omega_{exc}} \\ \mathrm{POS_F} &= \frac{\sum_B B(\sum_A \Omega_{AB}^{\mathrm{CT}})}{\Omega_{exc}} \end{aligned} \tag{129}$$

Then, the mean position of the excitation is

$$\mathrm{POS} = \frac{\mathrm{POS_I} + \mathrm{POS_F}}{2} \tag{130}$$

The average separation between electron and hole (*exciton size*) is defined as[109]

$$\begin{aligned} d_{exc}^2 = \langle (\vec{r}_h - \vec{r}_e)^2 \rangle_{exc} &= \frac{\langle \chi_{exc} | (\vec{r}_h - \vec{r}_e)^2 | \chi_{exc} \rangle}{\langle \chi_{exc} | \chi_{exc} \rangle} \\ &= \frac{1}{\Omega_{exc}} \int \int \gamma^{0I}(\vec{r}_h, \vec{r}_e)(\vec{r}_h - \vec{r}_e)^2 \gamma^{0I}(\vec{r}_h, \vec{r}_e)\, dr_h dr_e \end{aligned} \tag{131}$$

It can be calculated approximately as

$$\tilde{d}_{exc} = \sqrt{\frac{1}{\Omega_{exc}} \sum_{M,N} \Omega_{MN}^{\mathrm{CT}} d_{MN}^2} \tag{132}$$

where d_{MN} is the distance between the nuclei M and N.

Instead of canonical orbitals, as an alternative basis *natural transition orbitals*[85] (NTOs) can be used to describe electronic transitions. NTOs can be calculated from the transition density matrix. Since the transition density matrix is not symmetric, it cannot be

diagonalized. However, the hole matrix[106] $\boldsymbol{DD^\dagger}$ and the electron matrix $\boldsymbol{D^\dagger D}$ can be diagonalized by the unitary transformation matrices $\boldsymbol{U}$ and $\boldsymbol{V}$, respectively. Then, the hole natural transitions orbitals ψ_i^h are

$$\psi_i^h(\vec{r}) = \sum_j U_{ij}\psi_j(\vec{r}) \tag{133}$$

and the electron NTOs are

$$\psi_i^e(\vec{r}) = \sum_j V_{ij}\psi_j(\vec{r}) \tag{134}$$

In this work, the charge-transfer numbers Ω^{CT} and POS values are used to characterize the states and to distinguish between local excitations corresponding to $\pi\pi^*$ states and charge-transfer states corresponding to $\pi\sigma^*$ excitations. Furthermore, NTOs are employed to visualize the excitations. Additionally, the approximate exciton size of the $\pi\sigma^*$ states was calculated and the correlation with the excitation energy was investigated.

3

RESULTS AND DISCUSSION

In this chapter, the results of the investigations of the mechanism of O–H elongation (Section 3.1) and solvent reorganization (Section 3.2) will be discussed. The computational details of the calculations that were carried out will be described together with the results.

3.1 MECHANISM 1: ELONGATION OF O–H BOND

As described in Chapter 1, the mechanism for photodissociation of phenol proposed by Sobolewski et al.[2,3] after excitation to the bright $\pi\pi^*$ state involves overcoming a barrier between the minimum of the bright $\pi\pi^*$ state and the conical intersection between the $\pi\pi^*$ and the dark $\pi\sigma^*$ state which is dissociative with respect to the O–H bond of phenol. The reaction coordinate of this mechanism is the O–H bond distance. To investigate the energetic barrier associated with this mechanism, scans of the O–H distance have been carried out with CASPT2 and ADC(2). The scans described in the following differ from those by Sobolewski et al.[2,3] in the choice of the active space: for the CASSCF geometry optimizations Sobolewski et al. used a (6,6) active space, containing the six π and π^* orbitals for the $\pi\pi^*$ optimized scan. In case of the $\pi\sigma^*$ optimized scan, three π, two π^* and the σ^* orbitals were included while the highest π^* orbital was removed from the active space. For the CASPT2 energy calculations of phenol, a (8,8) active space was used by them, containing all valence π orbitals of phenol and the σ^* orbital. For the calculations on phenol-water clusters, an additional π orbital located at the oxygen atom of water was included by them in the active space. Use of different active spaces can introduce inconsistencies in the results. In order to see whether the results from Sobolewski et al. were consistent, we used the same active space in the whole computational procedure: in the CASSCF and CASPT2 calculations described as the following, a (6,7) active space containing the six π and π^* orbitals as well as the σ^* orbital, was used. For comparison, calculations have also been carried out with a (6,9) active space (see Appendix A.3).

3.1.1 *CASPT2 O–H scan*

Since CASPT2 has been used in the past to study the photophysics of phenol along the reaction coordinate of O–H bond elongation,[2,3] for phenol with one water molecule a scan of the O–H bond distance has been carried out employing this method (see Figure 4a: Geometries of the $\pi\pi^*$ and the $\pi\sigma^*$ states at different O–H distances were optimized with SA-CASSCF(6,7) for three states employing MOLCAS, version 8.0.[111]. The augmented correlation-consistent polarized valence-only double *zeta* (aug-cc-pvdz) basis set[56,113–115] was used. To obtain accurate energies, multi-state (MS)[116] CASPT2[63,64] calculations were performed on the CASSCF-optimized geometries using the corresponding active space size and number of states. A level shift of 0.3 was used to avoid the occurence of intruder states even in geometries far from the Frank-Condon region. Test calculations for the ground-state and excited-state optimized geometries without level shift showed the occurence of intruder states (see Section A.2 in the Appendix). No IPEA shift was used.[117] The energies are plotted relative to the energy of the ground-state optimized geometry. The energies plotted for S_0 were calculated at $\pi\sigma^*$-optimized geometries. The O–H distance at the crossing and the height of the

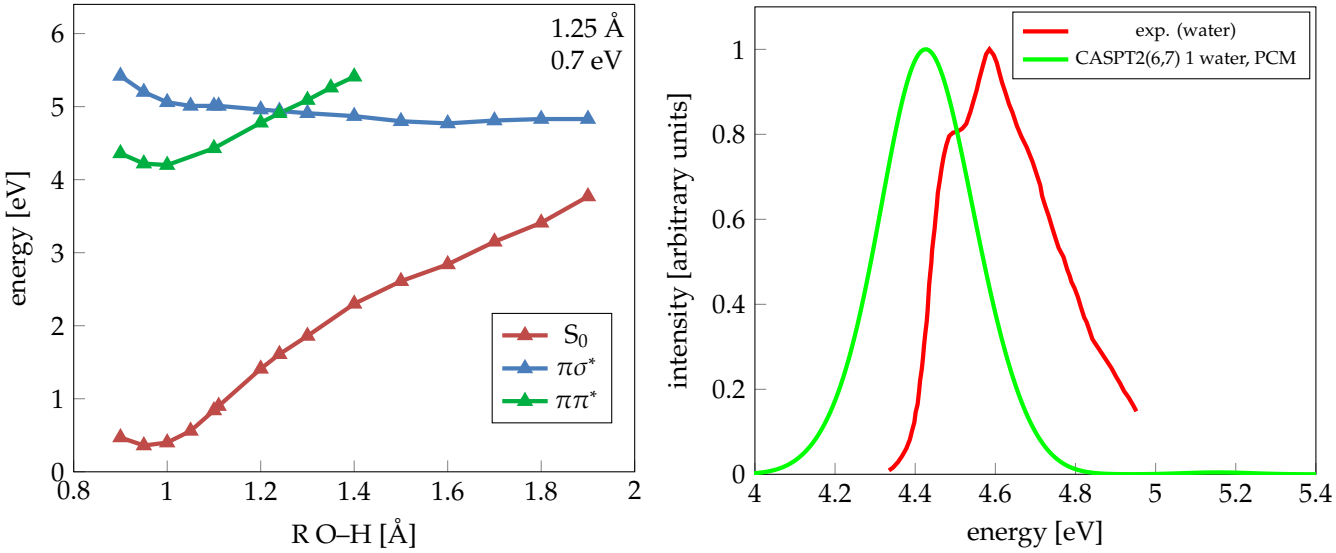

Figure 4. a) MS-CASPT2 energies of geometries of phenol with one water molecule optimized with SA-CASSCF(6,7) in the $\pi\pi^*$ and the $\pi\sigma^*$ state plotted relative to the energy of the S_0-optimized geometry. Energies of S_0 were calculated at $\pi\sigma^*$-optimized geometries. Numbers in the right corner give the O–H distance at the $\pi\pi^*/\pi\sigma^*$ crossing and the height of the energy barrier between these states. b) Absorption spectrum calculated with MS-CASPT2 with one explicitely treated water molecule and PCM for 100 snapshots from a classical MD simulation. Experimental data from Ref. 112

energy barrier, calculated as the energy difference between the minimum of the $\pi\pi^*$ state and the crossing, are also shown. Here, the term "crossing" refers to the point of intersection between the fitted curves corresponding to the $\pi\sigma^*$ and $\pi\pi^*$ states. We did not try to optimize the conical intersection between $\pi\pi^*$ and $\pi\sigma^*$ state. The orbitals included in the (6,7) active space are depicted in Figure 5.

The value of the O–H distance at the crossing between $\pi\pi^*$ and $\pi\sigma^*$ states of 1.25 Å as well as the height of the energy barrier between these states of 0.7 eV agree with the results obtained by Sobolewski et al.[2] From the experimentally observed timescale for the formation of solvated electrons,[8] which is about 2 ns, the expected height of the barrier which has to be overcome after excitation to the $\pi\pi^*$ state can be calculated based on the Arrhenius equation (see Chapter 1), giving a value of about 0.24 eV . The barrier calculated with CASPT2 corresponds, according to the Arrhenius equation, to a time constant of about 0.09 s, whereas the formation of the solvated electron was experimentally observed after about 2 ns. With an energy barrier of 0.7 eV the photodissociation mechanism of phenol by O–H bond elongation would seem improbable. Sobolewski et al. suggest that the height of the barrier should decrease with increasing number of water molecules, but this has never been shown. Unfortunately, investigating this hypothesis by including larger numbers of water molecules in the CASPT2 calculations is unfeasible due to difficulties with the selection of the active space.

Our results suggest that the energy of the $\pi\pi^*$ state is underestimated because the barrier height calculated with CASPT2 is considerably higher than that estimated based on the experimental time scale for the formation of the solvated electron. In order to corroborate this hypothesis, an absorption spectrum was calculated with CASPT2 with one explicitely treated water molecule and the polarizable continuum method (PCM) to simulate bulk solvation for 100 snapshots from a classical molecular dynamics simulation. This CASPT2(6,7) spectrum was calculated with a development version of MOLCAS that supports wavefunction analysis by the library libwfa. The MD simulation has been carried out with AMBER 16[118] using the general AMBER force field (GAFF)[119] on graphics processing units (GPUs).[120–122] Phenol was solvated in a truncated octahedral box extending to a distance of 15 Å from any solute atom,

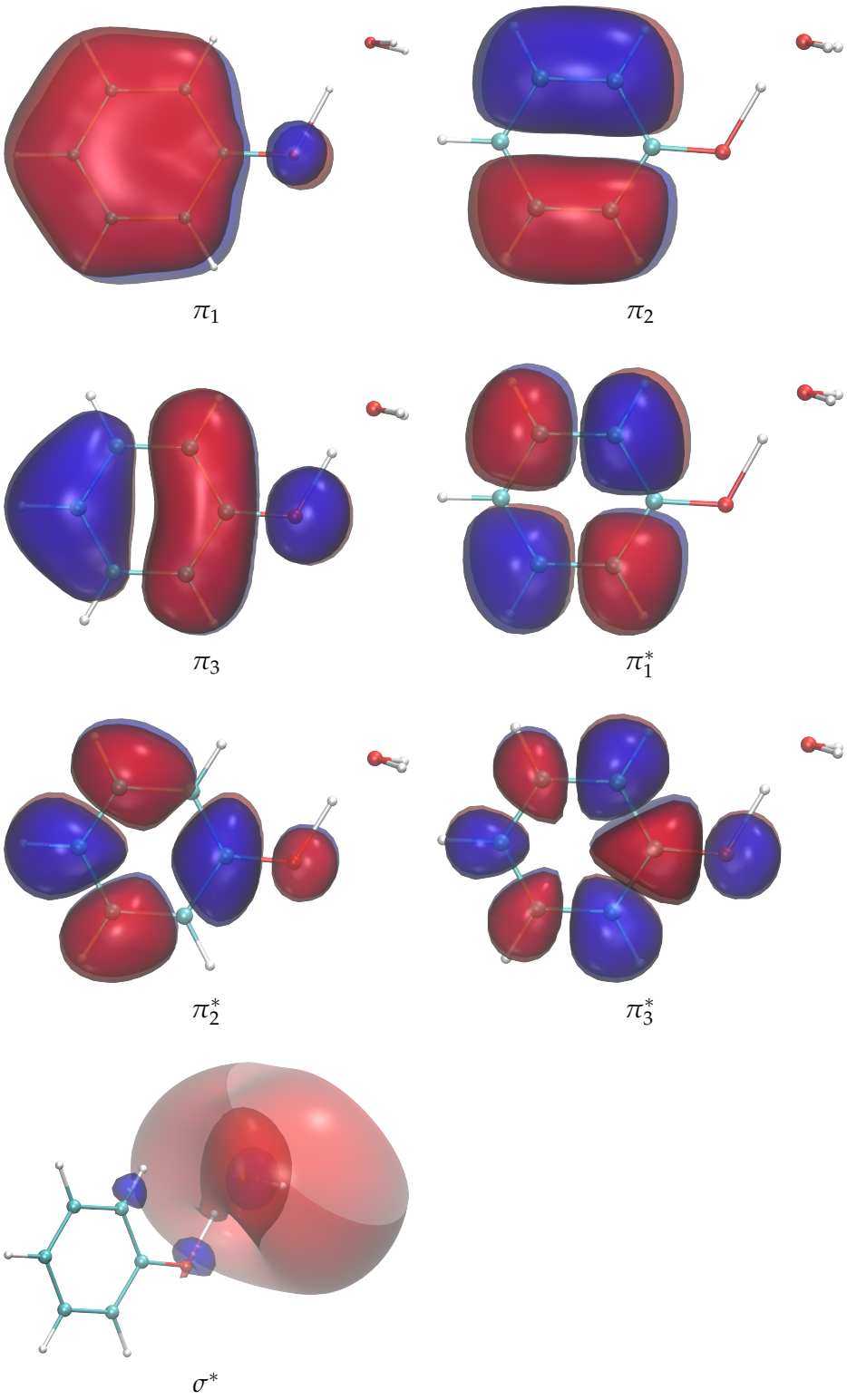

Figure 5. (6,7) active space depicted for $\pi\sigma^*$ optimized geometry at O–H distance of 1.4 Å.

filled with 1223 TIP3P[123] water molecules, using the leap module of AmberTools14. First, a minimization employing the steepest descent method has been carried out for 500 steps, followed by a conjugate gradient minimization for another 500 steps. Then, the system was heated during 200 ps with a timestep of 1 fs to 300 K at constant volume (NVT) employing a Langevin thermostat with a collision frequency of 5 ps^{-1}. After heating, an NPT molecular dynamics simulation was performed for 5 ns with a timestep of 2 fs. Every hundreth geometry was saved. A Berendsen barostat[41] was employed to keep the pressure at a value of 1 bar with a pressure relaxation time of

5 ps. A cutoff of 10 Å was used for the nonbonded interactions. For the calculation of electrostatic interactions, the particle mesh Ewald method[36–38] was employed. During the heating and the NPT MD simulation the bonds involving hydrogen atoms were constrained employing the SHAKE[124,125] algorithm. In order to allow for a more efficient sampling of relevant conformations, where a water molecule forms a hydrogen bond with the acidic hydrogen atom of phenol, during the heating and the 5 ns NPT MD trajectory the water molecule closest to the acidic hydrogen atom of phenol was restrained employing a harmonic potential at an equilibrium distance of 1.58 Å with a force constant of 50 kcal/molÅ^2. Since an analysis of an unconstrained MD simulation shows that a water molecule is hydrogen-bonded to phenol more than 80% of the time, the introduction of the constraint does not adulterate the simulation.

As can be seen from Figure 4 b, the CASPT2 spectrum is red-shifted compared to experiment by 0.157 eV. Thus, CASPT2 slightly underestimates the energy of the $\pi\pi^*$ state and thus overestimates the height of the barrier, leading to wrong mechanistic conclusions. In order to investigate whether a different method gives a better description of the system and can be employed for calculations involving several water molecules, a scan of the O–H distance has been carried out with ADC(2).

3.1.2 *ADC(2) O–H scan*

As shown in the previous subsection, CASPT2 overestimates the height of the energy barrier between $\pi\pi^*$ and $\pi\sigma^*$ states. One reason for this result could be the limited size of the active space. Therefore, an O–H scan has been carried out employing ADC(2), which is an accurate method that avoids difficulties with the selection of an active space (see Fig. 6). The ADC(2)[72] calculations have been carried out employing the Turbomole[126–130] program package with the aug-cc-pVDZ basis set.[56,113–115] The energies of the $\pi\sigma^*$ and $\pi\pi^*$ state were calculated based on the CASSCF-optimized geometries. The natural transition orbitals for the $\pi\sigma^*$ and $\pi\pi^*$ states at an O–H distance of 1 Å, which were calculated with the TheoDORE program package,[106,108,109,131–133] are depicted in Figure 7.

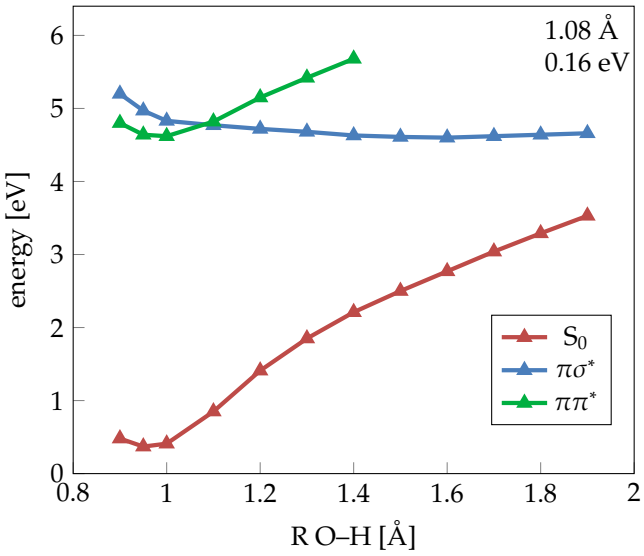

Figure 6. Energies calculated with ADC(2) of the geometries of phenol with one water molecule optimized employing CASSCF.

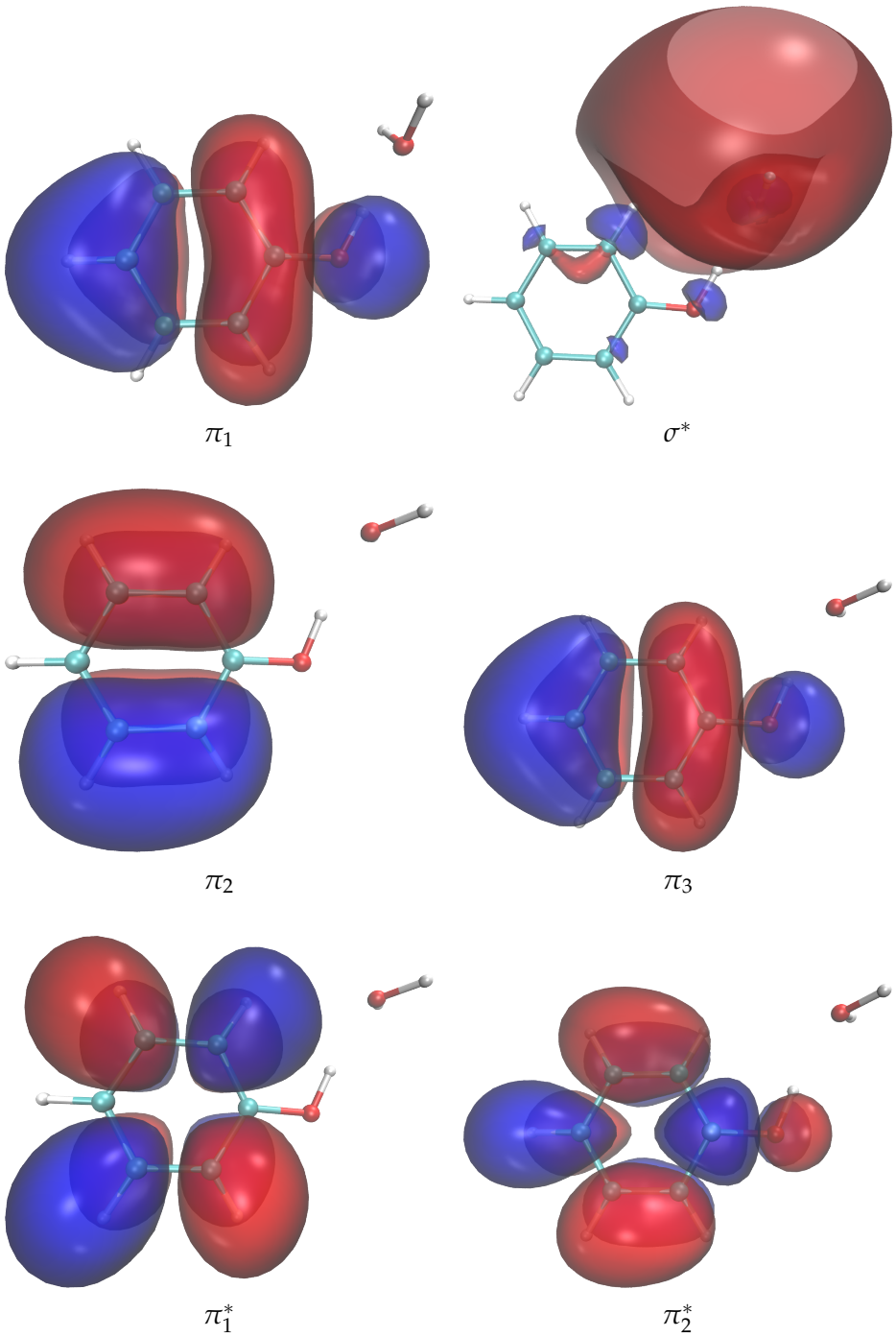

Figure 7. Natural transition orbitals calculated with ADC(2) at an O–H distance of 1 Å involved in the bright state, whose main transitions are $\pi_3\pi_1^*$ and $\pi_2\pi_2^*$, and the repulsive state, whose main transition is $\pi_1\sigma^*$.

For the $\pi\sigma^*$ transition, there is only one transition with large contribution, which involves the participation of only two orbitals, whereas the $\pi\pi^*$ state contains two transitions involving four NTOs corresponding to the two π orbitals with one nodal plane and the two π^* orbitals with two nodal planes orthogonal to the ring.

The crossing bond distance and energy barrier height calculated with ADC(2) are 1.08 Å and 0.16 eV. The height of the barrier corresponds to a time constant of 78 ps, showing better agreement with the experimental time of 2 ns than the CASPT2 value. However, as will be shown in section 3.2.1, ADC(2) overestimates the energy of the $\pi\pi^*$ state and therefore underestimates the height of the barrier.

With an energy barrier of about 0.2 eV the photodissociation mechanism by O–H bond elongation is plausible. Since ADC(2) agrees better with experiment than

CASPT2, this method will be used in the calculations with more water molecules. Also, CASPT2 calculations with several solvent molecules become rather expensive and the choice of the correct active space becomes more difficult the more water molecules are included.

3.2 MECHANISM 2: SOLVENT REORGANIZATION

As described in Chapter 1, for the photodissociation of the phenol derivative 5,6-dihydroxyindole a mechanism involving reorganization of the solvent molecules, facilitating the formation of a solvated electron and, thusly, sequential transfer of electron and proton to the solvent, was demonstrated by Nogueira et al.[24] In order to investigate whether this mechanism is also operative in phenol, the absorption spectrum and density of states were calculated after identification of a suitable solvent model. Since the σ^* orbital is located in the solvent, certain solvent configurations could stabilize this orbital, thereby decreasing the energy of the $\pi\sigma^*$ state already in the Franck-Condon region.

In this section, the investigated models for the description of the environment will be discussed: The size of the small cluster of explicitely treated water molecules was varied and the effects of bulk solvation were simulated by employing a continuum model and a hybrid QM/MM method. Then, the electronic structure of the absorption spectrum and the density of states will be analyzed. Finally, the results of the analysis to identify a geometrical feature of the solvent orientation lowering the energy of the $\pi\sigma^*$ state will be described.

3.2.1 *Solvent Description: Explicit Cluster Models*

Inclusion of the environment in the description of phenol is crucial since experiments suggest that the excited-state deactivation mechanism is different in polar solvents than in the gas phase or unpolar solvents. In order to investigate by which approach bulk solution could be simulated, both explicit and implicit solvation models were investigated.

To investigate the potential formation of a solvated electron, chemical intuition suggests that at least five water molecules should be included in the calculations explicitely since four water molecules are needed in the theoretical description of the solvated electron[134] and one water molecule acts as hydrogen acceptor in a hydrogen bond with the acidic proton of phenol. However, more water molecules might be needed. In the cluster model used by Nogueira et al.[24] 10 water molecules were included. On the other hand, the energies of the $\pi\sigma^*$ and $\pi\pi^*$ states might already be converged with fewer water molecules. In order to determine the number of water molecules that should be considered explicitely, the absorption spectrum of phenol with different sizes of the cluster model was calculated with ADC(2) (see Figure 9) for up to 101 snapshots taken from the last 2 ns of the constrained classical molecular dynamics simulation. Due to difficulties with the generation of redundant internal coordinates with larger numbers of water molecules, the number of geometries varies between 96 and 101 for the different cluster sizes. Table 2 lists the number of snapshots on which the calculated absorption spectra are based. Since the position of the σ^* orbital of the $\pi\sigma^*$ state is expected to be close to the water molecule forming a hydrogen bond to the acidic proton of phenol, this water molecule was included for the cluster of size one. For the larger cluster sizes the four and fourteen water molecules closest to this hydrogen-bonded water molecule were included in the calculations. The states were convoluted with Gaussian functions of full width at half maximum of 0.2 eV and height proportional to the oscillator strength. Since the energetic region of the $\pi\pi^*$ band is of interest for

this study, only transitions with energies below 5.2 eV were included in the absorption spectra plotted below. For comparability the height of the spectra was scaled to one. For better comparison, the energy of the peak of the spectra and the difference to experiment is listed in Table 3.

Table 2. Number of geometries for different numbers of explicitely treated water molecules based on which the absorption spectrum and density of states were calculated.

Size of cluster	number of geometries
0	101
1	101
5	99
15	96

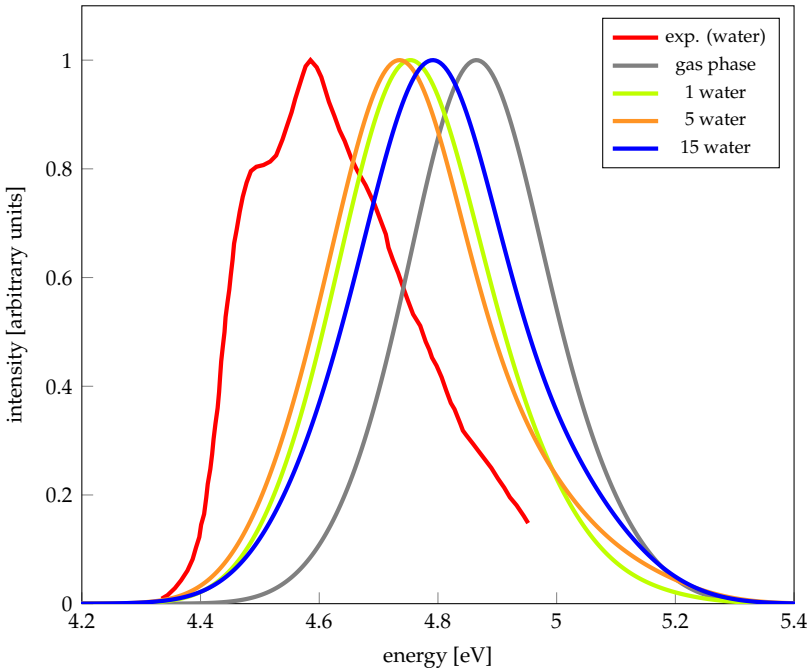

Figure 8. Absorption speectrum calculated with ADC(2) for different water cluster sizes based on 96 to 101 geometries from a constrained classical molecular dynamics simulation. Experimental data from Ref. 112

Table 3. Excitation energy at the maximum of the peak and difference to experiment[112] for different cluster sizes in eV.

Cluster size	energy at peak	diff. to exp.
experiment[112]	4.59	
gas phase	4.86	0.27
1	4.75	0.16
5	4.74	0.15
15	4.79	0.20

The calculated spectra agree well with experiment. However, the experimental spectrum, which peaks at an excitation energy of 4.59 eV, has a shoulder at lower energies which is not reproduced by the calculated spectra. This shoulder could be due to

vibronic transitions or the presence of dimers, factors that are not considered by the theoretical model here. The gas phase spectrum, peaking at 4.86 eV, is blue-shifted by 0.27 eV compared to experiment, indicating that ADC(2) slightly overestimates the energy of the $\pi\pi^*$ state, consistent with the small underestimation of the energy barrier between the $\pi\pi^*$ and $\pi\sigma^*$ states described in Section 3.1.1. Inclusion of just one water molecule leads to a red shift of 0.11 eV, decreasing the difference to experiment to 0.16 eV. Increasing the size of the water cluster to five water molecules causes only a small red shift of 0.01 eV. However, a further increase of the cluster size to 15 water molecules causes a blue shift of 0.05 eV compared to the cluster size of five. With this energy behaviour one cannot be sure if the energy of the $\pi\pi^*$ state is already converged with respect to the number of water molecules treated explicitely. However, calculations including more explicitely treated water molecules quickly become unfeasible. In order to simulate the effects of bulk solvation, QM/continuum and QM/MM calculations were carried out. Since the largest shift occurs when going from the gas phase to a cluster of one water molecule and experimental observations suggest that hydrogen bonding plays an important role in the photodeactivation mechanism of phenol, in these continuum and QM/MM calculations one water molecule was included explicitely.

The 101 snapshots from the constrained classical MD simulation with the hydrogen-bonded water molecule were used for the calculation of absorption spectra employing the COSMO implicit solvation model and a hybrid QM/MM approach. The spectra were calculated as described above. Figure 9 shows these spectra and, for comparison, the experimental spectrum as well as the spectrum calculated with the cluster size of 15 water molecules. The energy of the maximum of the peaks and the difference to experiment is listed in Table 4.

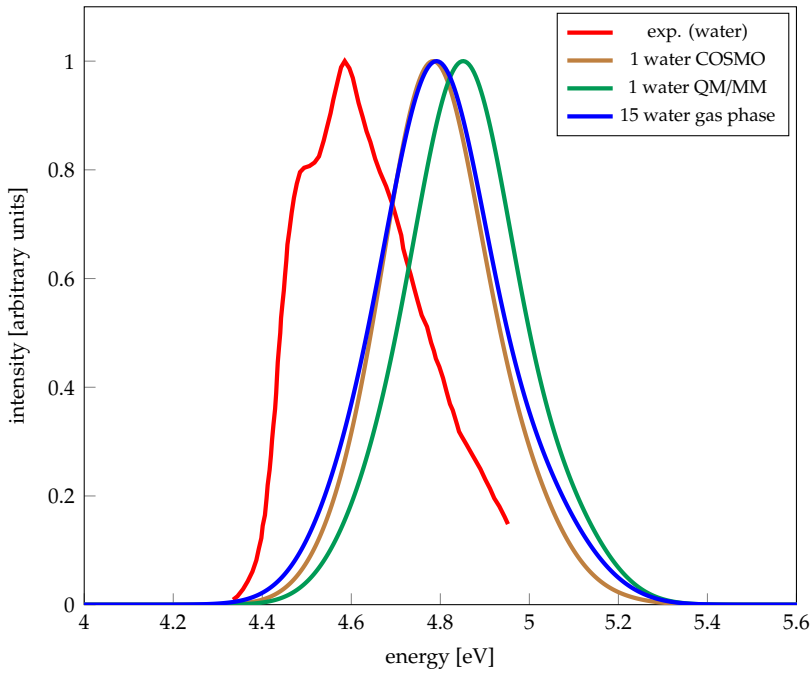

Figure 9. Absorption spectrum calculated with ADC(2) for different solvent models.

The spectrum calculated with one explicitely treated water molecule and the COSMO continuum model, peaking at an excitation energy of 4.78 eV, agrees very well with the spectrum based on a cluster size of 15, which peaks at 4.79 eV. The QM/MM spectrum with one water molecule in the QM region is blue-shifted by 0.07 eV compared to the spectrum of the continuum model. Since the electrostatic interactions between the solvent model and the QM region are described self-consistently in the continuum

Table 4. Excitation energy at the maximum of the peak and difference to experiment for different solvent models in eV.

Solvent model	energy at peak	diff. to exp.
experiment[112]	4.59	
1 water COSMO	4.78	0.19
1 water QM/MM	4.85	0.26
15 water	4.79	0.20

model but the MM region in the QM/MM calculation is not polarizable, it is to be expected that the COSMO model is better able to describe the interactions with bulk solvation. For calculations of excited states, polarizability of the environment is even more important than for ground-state calculations since the electronic distribution of the chromophore changes considerably, and the solvent needs to react accordingly which is not possible with electrostatic-embedding QM/MM. The good agreement between the spectrum based on one water and COSMO, which models complete bulk solvation, and the spectrum with the 15 water molecules cluster size suggests that the energy of the $\pi\pi^*$ state is already converged with this number of water molecules. Therefore, in the following analysis this cluster model will be used.

3.2.2 *Electronic structure analysis of absorption spectrum and density of states*

If the photodissociation mechanism of formation of a solvated electron facilitated by solvent reorganization is operable, it is expected that for some geometries obtained in the configurational sampling by molecular dynamics the energy of the $\pi\sigma^*$ state is already low in the Franck-Condon region. In order to investigate this hypothesis, the electronic structure of the absorption spectrum and the density of states calculated with the chosen cluster model was analyzed with the TheoDORE program package.[106,108,109,131–133] For the population analysis the Löwdin method[135,136] was used. In order to distinguish between local excitations at the phenol molecule, corresponding to $\pi\pi^*$ states, and charge-transfer states between the phenol and the water molecules, a combination of two criteria from the wavefunction analysis was used: The charge-transfer number (CT) gives the percentage of charge-transfer character. A value of 0.5 was used to identify charge-transfer states corresponding to $\pi\sigma^*$ excitations. The POS value gives the fragment of the average position of the excitation. Phenol was defined as the first fragment and a POS value of $\leqslant 1.2$ was employed as the threshold to identify excitations which are located mainly at phenol and not at the solvent. Excitations with a charge-transfer number $\leqslant 0.5$ and a POS value $\leqslant 1.2$ were classified as $\pi\pi^*$ states. Figure 10 shows the absorption spectrum and the decomposition into $\pi\pi^*$ and $\pi\sigma^*$ states, according to this classification. The percentages of the spectrum comprised of $\pi\pi^*$ and $\pi\sigma^*$ states were calculated as the ratios between the areas under the corresponding curves.

The $\pi\sigma^*$ states have low oscillator strength, accounting for only 5% of the total absorption spectrum, whereas the $\pi\pi^*$ states are bright and account for 90% of the spectrum. In addition, the $\pi\sigma^*$ states are found at the blue end of the spectrum, mostly at higher energies than the peak of the $\pi\pi^*$ band. Thus, it seems unlikely that direct excitation to the $\pi\sigma^*$ band is possible. However, only states with a sufficiently large oscillator strength are included in the absorption spectrum. If there exist dark $\pi\sigma^*$ states at lower energies than the peak of the $\pi\pi^*$ band, population of these dark $\pi\sigma^*$ states might be possible after excitation to the $\pi\pi^*$ state and subsequent internal

conversion. The density of states, which takes into account all states irrespective of their oscillator strength, is depicted in Figure 11.

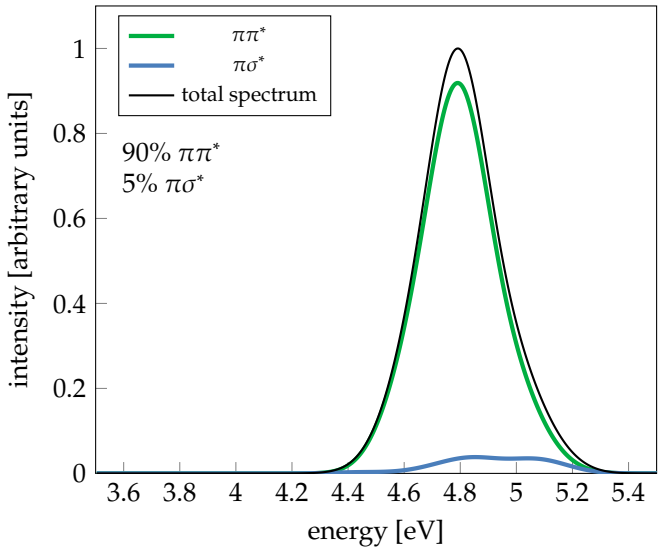

Figure 10. Absorption spectrum of phenol microsolvated by a cluster of 15 water molecules calculated with ADC(2) and decomposition into $\pi\pi^*$ states and $\pi\sigma^*$ states.

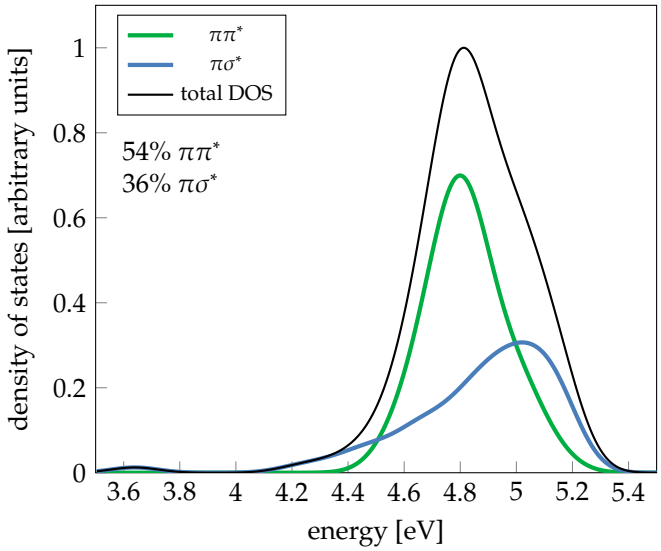

Figure 11. Density of states of phenol solvated by a cluster of 15 water molecules and decomposition into $\pi\pi^*$ and $\pi\sigma^*$ states.

The density of states is comprised to 36% of $\pi\sigma^*$ and 54% of $\pi\pi^*$ states. Thus, $\pi\sigma^*$ states have a considerably larger contribution to the DOS than to the absorption spectrum. While most of these $\pi\sigma^*$ states are in the blue region of the spectrum, a significant number also exists at energies below the maximum of the $\pi\pi^*$ band. These dark $\pi\sigma^*$ states can in principle be populated by internal conversion after excitation to the $\pi\pi^*$ state.

Among the 96 geometries on which the absorption spectrum and the DOS are based, there are six geometries for which the $\pi\pi^*$ and $\pi\sigma^*$ states are nearly degenerate. The energies of the first and second excited states of these geometries as well as charge-transfer numbers and O–H bond distances are listed in Table 5. Figure 12 shows for one exemplary geometry the natural transition orbitals of S_1 and S_2. For illustration, the excitation energies of these states are highlighted in the density of states depicted

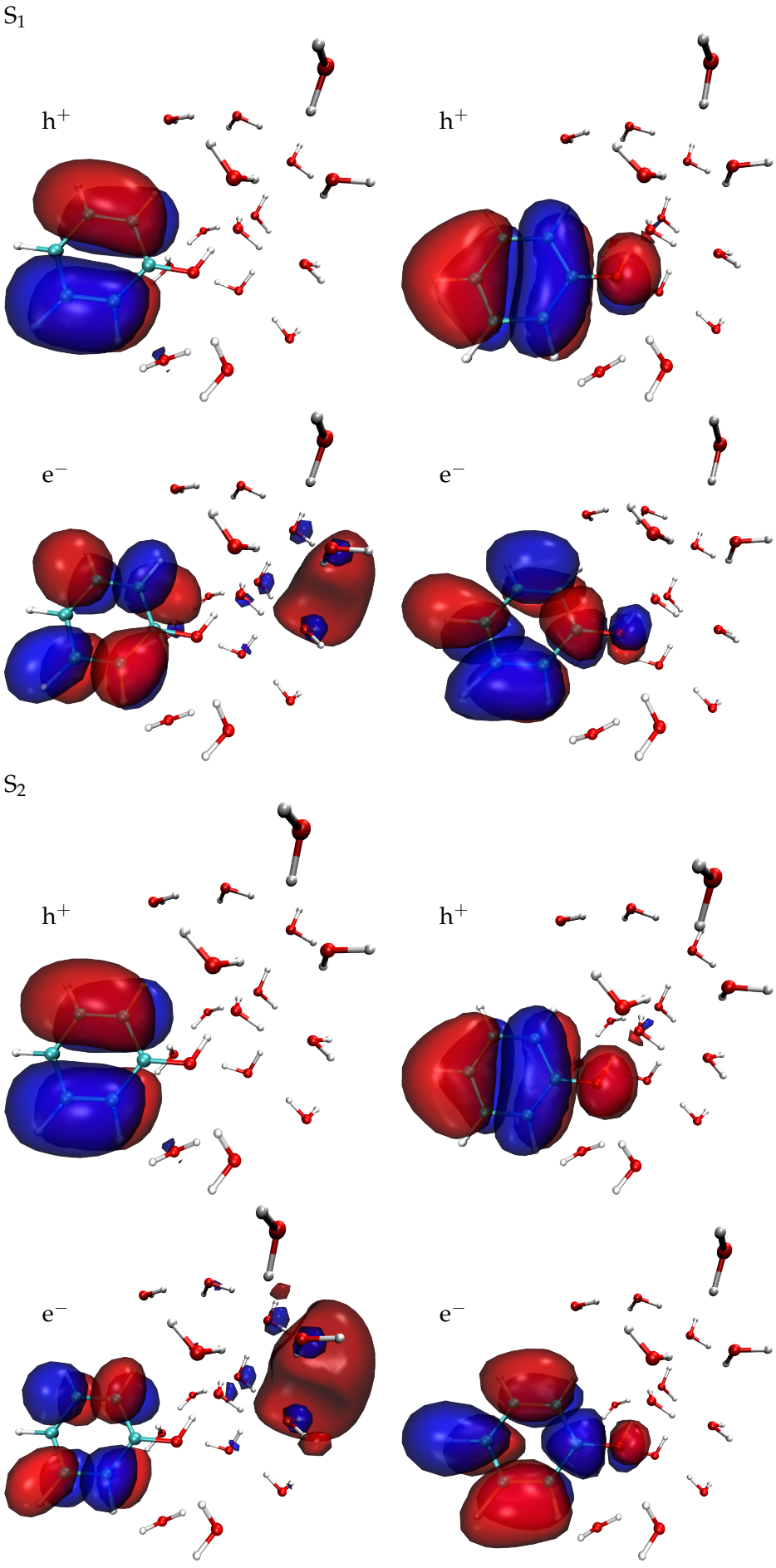

Figure 12. Natural transition orbitals of the first (excitation energy 4.78444 eV) and second (4.83825 eV) excited state of one geometry with nearly degenerate $\pi\pi^*$ and $\pi\sigma^*$ states. Hole natural transition orbitals are denoted with h^+, electron NTOs with e^-.

in Figure 13. The natural transition orbitals show a considerable contribution of both π^* and σ^* orbitals in both the first and second excited state, indicating that both states are mixed.

Table 5. Excitation energy (in eV) and charge-transfer number of the first and second excited state as well as difference between the energies of S_1 and S_2 (in eV) and O–H bond distance (in Å) of the geometries with nearly degenerate $\pi\pi^*$ and $\pi\sigma^*$ states.

S_1 exc. energy	S_1 CT	S_2 exc. energy	S_2 CT	energy diff.	O–H distance
4.78	0.41	4.84	0.60	0.06	0.974
4.64	0.37	4.81	0.43	0.17	0.975
4.65	0.38	4.68	0.42	0.03	0.974
4.74	0.55	4.76	0.44	0.02	0.974
4.62	0.40	4.85	0.23	0.23	0.974
4.78	0.20	4.83	0.38	0.05	0.973

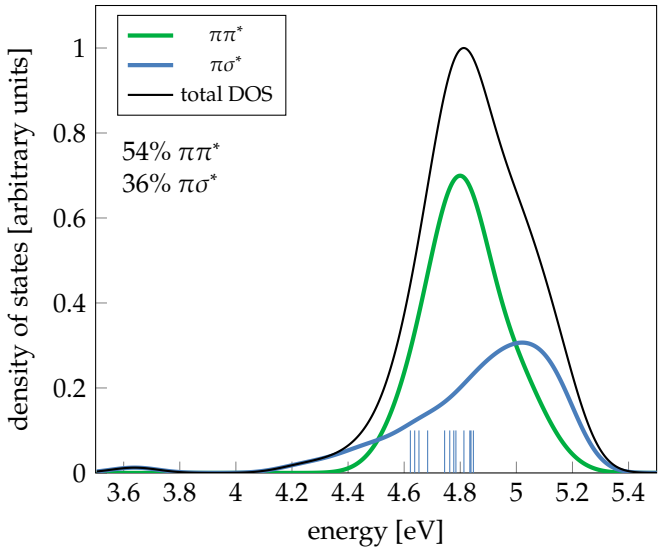

Figure 13. Density of states with the excitation energies of the nearly degenerate $\pi\sigma^*$ and $\pi\pi^*$ states depicted as vertical lines. For this illustration, the DOS of these states is depicted arbitrarily as 0.1 for better visibility.

For these energetically degenerate states the charge-transfer numbers are usually slightly below 0.5, indicating that the $\pi\pi^*$ and $\pi\sigma^*$ states are mixed since the values are between those of pure $\pi\pi^*$ states with charge-transfer numbers of the order of 0.05 and those of pure $\pi\sigma^*$ states (CT $>$ 0.5). For four of the geometries, the difference between the energies of the first and second excited state is below 0.1 eV, for one geometry the energy difference is as small as 0.018 eV. The excitation energies of the geometries with nearly degenerate $\pi\pi^*$ and $\pi\sigma^*$ state are below or near the maximum of the $\pi\pi^*$ band. Thus, the near-degeneracy occurs for geometries for which the $\pi\sigma^*$ state decreases in energy and not due to an increase of the energy of the $\pi\pi^*$ state. In order to investigate whether the factor contributing to decreasing the energy of the $\pi\sigma^*$ state is O–H elongation as suggested by Sobolewski et al.,[2,3] the O–H distances of these geometries were compared to the average of the ensemble. The average O–H bond length of the geometries with degenerate $\pi\pi^*$ and $\pi\sigma^*$ states is 0.97412 Å while that of all snapshots that were used for the calculation of the spectrum is 0.97393 Å. The negligible difference between the O–H distances suggests that an elongation of the

O–H bond is not necessary but rather the orientation of the solvent molecules plays an important role. Therefore, an anaylsis to identify a geometrical feature that contributes to a lowering of the energy of the $\pi\sigma^*$ state was carried out in the next subsection.

3.2.3 *Factors contributing to lowering of energy of $\pi\sigma^*$ state*

The energy of the $\pi\sigma^*$ state depends partially on the orientation of the solvent molecules. A σ^* orbital surrounded by several water molecules, with their hydrogen atoms pointing towards it, is probably better stabilized than a less well solvated σ^* orbital. Thus, a good solvation of the σ^* orbital requires a large separation between phenol and the electron, which reduces the Coulomb attraction between electron and hole. In order to quantify these geometrical analyses, two investigations of the charge-transfer states were carried out. First, the distance between the hole and the electron was computed as the root-mean-squared electron-hole separation employing the TheoDORE wavefunction analysis package. Second, the number of water molecules involved in the solvation sphere of the σ^* orbital was determined.

Figure 14 shows a plot of the root-mean-square electron-hole separation versus the excitation energy.

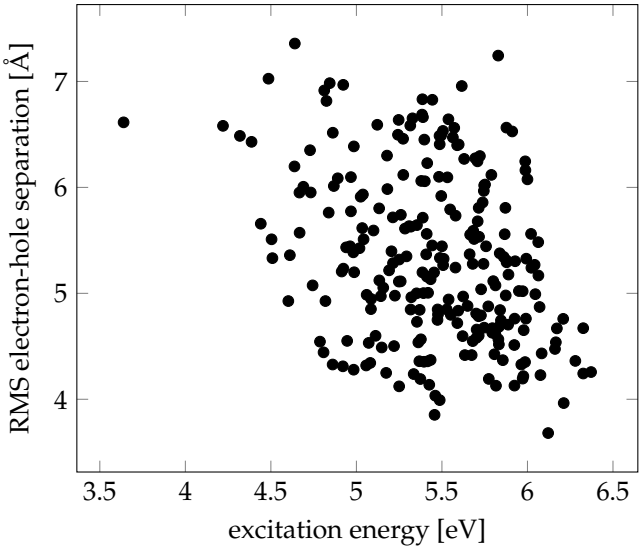

Figure 14. Root-mean-square (RMS) electron-hole separation versus excitation energy of all charge-transfer states.

Although the distribution is rather broad, a trend is clearly visible: Lower excitation energies are associated with larger root-mean-square electron-hole separations. This results seems curious since a larger electron-hole separation reduces the Coulombic interaction between electron and hole and should therefore increase the energy. However, a larger distance from the electron to the hole, which is located on phenol, allows for more water molecules to surround the orbital, thus providing a better solvation and lowering the energy of the $\pi\sigma^*$ state. In order to investigate this hypothesis, the correlation between the number of water molecules containing more than 10% of electron population and the root-mean-square electron-hole separation was examined. The results are plotted in Figure 15.

As expected, the number of water molecules solvating the σ^*-orbital increases with the electron-hole separation. As a consequence, the solvation energy that stabilizes the system increases, which can counteract the loss of Coulombic energy between the electron and the hole due to the larger separation. For further investigation, a geometrical

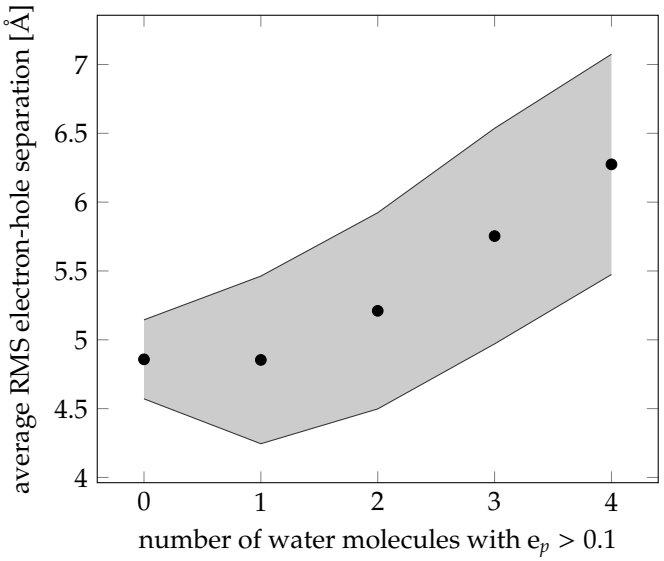

Figure 15. Root mean square (RMS) electron-hole separation versus number of water molecules containing $> 10\%$ of electron population. The standard deviation is indicated by the shaded area.

analysis was carried out to examine whether a correlation between excitation energy and number of water molecules in close proximity to the orbital exists.

In order to allow for a partially automated analysis of the 96 geometries based on which a total of 244 charge-transfer states were calculated, an approximation of the position of the σ^* orbital needs to be defined. For this purpose, in the wavefunction analysis each water molecule was defined as a single fragment and the electron and hole populations for each fragment were calculated. Then, for each charge-transfer state the water molecules containing more than 10% of electron population were identified. The approximate position of the σ^* orbital was defined as the center of mass of these water molecules. For illustration, for one exemplary state the orbital and the center of mass are depicted in Figure 16. For each number of water molecules containing more than 10% of electron population the average of the excitation energies of all charge-transfer states was calculated. The results are plotted in Figure 17. The numbers of states corresponding to the different cluster sizes are listed in Table 6.

Table 6. Number of states with different numbers of water molecules containing more than 10% of electron population.

0	1	2	3	4
7	58	112	59	16

Although the standard deviation is rather large, a lower excitation energy is clearly associated with a larger number of water molecules solvating the orbital. This result agrees with the result that a lower energy correlates with a larger electron-hole separation, allowing for better stabilization of the orbital due to the presence of several water molecules close to it.

In general, the excitation energy clearly decreases with increasing number of water molecules in close proximity to the approximate position of the σ^* orbital. Chemical intuition suggests that the orientation of the water molecules also plays an important role, but it was not possible to identify further conditions neccesary to lower the energy of the $\pi\sigma^*$ state.

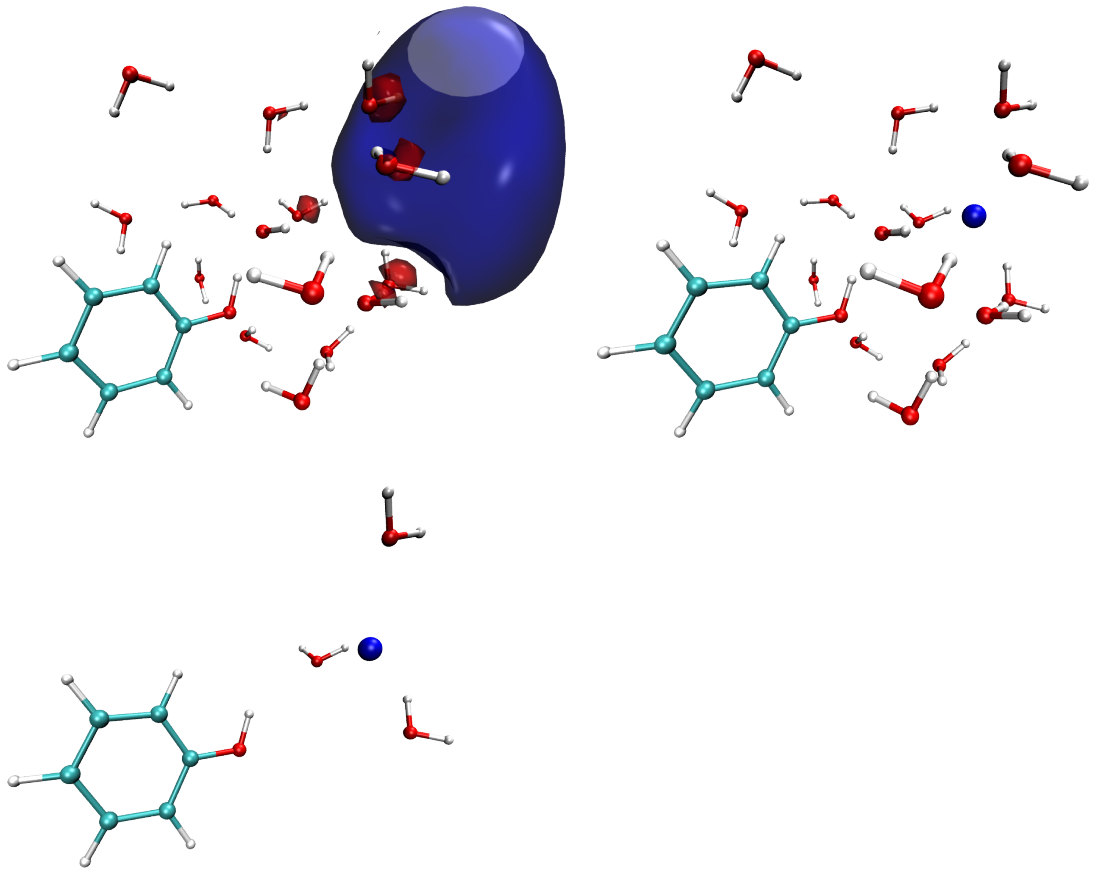

Figure 16. σ^* orbital of one exemplary charge-transfer state and center of mass (figured as blue sphere) of the three water molecules containing more than 10% of electron population. The three water molecules are depicted in the bottom picture.

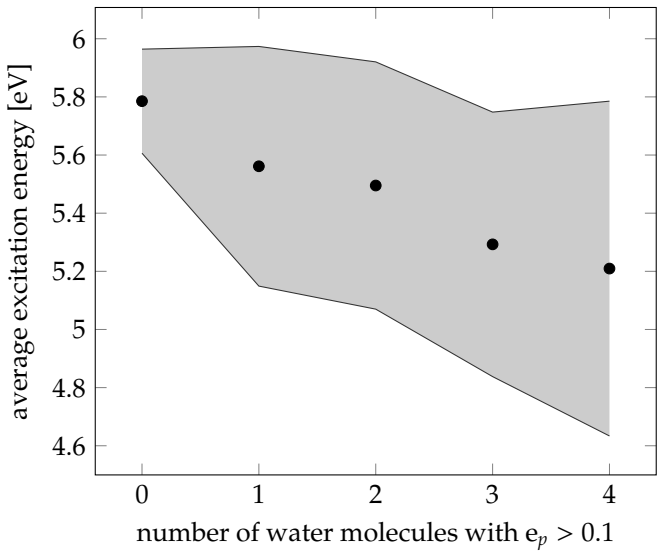

Figure 17. Average of the excitation energy of charge-transfer states with different numbers of solvent molecules containing $>$ 10% of electron population. The standard deviation is represented by the shaded area.

To summarize the findings of the investigation of the mechanism of solvent reorganization, a cluster size of 15 water molecules seems to be enough since the spectrum calculated with this environment model agrees very well with the spectrum calculated with the QM/continuum model, which is able to describe the effects of bulk solva-

tion. An electronic structure analysis of the absorption spectrum and density of states shows that while the $\pi\sigma^*$ states are mainly dark, there exist several low-lying $\pi\sigma^*$ states which can be populated by internal conversion after excitation to the $\pi\pi^*$ band. The factor contributing to lowering the energy of the $\pi\sigma^*$ state is not O–H elongation but rather the orientation of the solvent molecules. In order to lower the energy of the $\pi\sigma^*$ state the σ^* orbital has to be well solvated by several water molecules. Lowest $\pi\sigma^*$ excitation energies were obtained if the σ^* orbital is solvated by 4 water molecules. A large number of solvating water molecules is only possible if the σ^* orbital is located at a comparatively large distance from phenol, with a root-mean-square electron-hole separation of about 6 Å. These water molecules likely also have to be oriented in a certain way to better stabilize the orbital.

4

CONCLUSIONS AND OUTLOOK

The goal of this work was to investigate two possible mechanisms for the photodissociation of phenol. After excitation to the bright first excited state of $\pi\pi^*$ character, a conical intersection to a dark, dissociative state of $\pi\sigma^*$ character is present. For the reaction coordinate, two hypotheses have been examined: 1) elongation of the O–H bond; 2) reorganization of the solvent molecules, facilitating the formation of a solvated electron.

In order to investigate the mechanism of O–H bond elongation, the geometries of the $\pi\pi^*$ and the $\pi\sigma^*$ state for different O–H distances for phenol with one water molecule forming a hydrogen bond to the acidic proton were optimized with CASSCF. The energies of these geometries were calculated with CASPT2 and ADC(2). The height of the energy barrier between the $\pi\pi^*$ and $\pi\sigma^*$ states computed with CASPT2 is 0.7 eV. The experimental time scale[8] for the formation of solvated electrons in phenol in aqueous solution ($>$ 2 ns) corresponds to a barrier height of about 0.24 eV. While CASPT2 overestimates the barrier height, the value calculated with ADC(2) (0.16 eV), although slightly underestimated, agrees better with experiment. Thus, the mechanism of O–H elongation seems plausible.

For the investigation of the mechanism of solvent reorganization, first a suitable model for the description of the environment had to be found. Therefore, the absorption spectrum of phenol microsolvated by clusters comprised of different numbers of water molecules based on 101 snapshots of a classical molecular dynamics simulation was calculated and compared to experiment. The excited-state energies calculated with a cluster size of 15 water molecules agree very well with the results of QM/COSMO calculations, which are able to describe the effects of bulk solvation. The electronic structure of the absorption spectrum and the density of states calculated with this model were analyzed in order to investigate whether for some orientations of solvent molecules the $\pi\sigma^*$ state is the lowest excited state already in the Franck-Condon region. While the $\pi\sigma^*$ state is mainly dark and direct excitations to it seem improbable, an analysis of the density of states shows that for several geometries the $\pi\sigma^*$ state has a lower energy than the maximum peak of the $\pi\pi^*$ band. These low-lying $\pi\sigma^*$ states can in principle be populated by internal conversion after excitation to the $\pi\pi^*$ band. Finally, an analysis to identify factors contributing to lowering the energy of the $\pi\sigma^*$ state was carried out. The excitation energy of charge-transfer states decreases with increasing root-mean-square electron-hole. While this finding seems curious since a larger electron-hole separation reduces the Coulomb attraction between electron and hole and should therefore increase the energy, a larger electron-hole separation allows for more water molecules solvating and stabilizing the σ^*-orbital, reducing the energy of the $\pi\sigma^*$ state without elongation of the O–H bond. Thus, a larger number of water molecules with an electron population $>$ 10% and a larger number of water molecules within 3 Å around the approximate position of the σ^*-orbital are associated with a lower excitation energy. To conclude, the mechanism of solvent reorganization facilitating the formation of a solvated electron seems plausible. Lower energy of the $\pi\sigma^*$ state was obtained if the σ^* orbital was solvated by 4 water molecules. This is possible when the root-mean-square electron-hole separation is around 6 Å.

For further investigation of the mechanism of photodissociation of phenol, it would be interesting to carry out excited-state dynamics. However, due to the long time scale of the formation of solvated electrons, enhanced sampling methods[137,138] like acceler-

ated molecular dynamics would have to be used, which are currently not implemented in the program packages for non-adiabatic dynamics. Furthermore, the possibility of the mechanism of solvent reorganization could be investigated for derivatives of phenol.

A

APPENDIX

The following Appendix contains further results that were obtained in the course of this work. Apart from CASPT2 and ADC(2) results discussed in Section 3.1, scans along the O–H elongation coordinate have been performed with different methods in order to aid in the choice of a compuational method (Section A). The electronic structure of absorption spectrum and density of states calculated for phenol with different numbers of water molecules was analyzed to investigate the influence of the cluster size on the occurence of low-lying $\pi\sigma^*$ states (Section B). Absorption spectra with different methods and environment models were calculated based on snapshots from a classical MD simulation in order to aid in the choice of a suitable computational model including solvent and electronic structure of the chromophore (Section C). For the cluster model comprised of 15 water molecules, further geometrical analysis was carried out to investigate the relation between excitation energy and number of water molecules in close proximity to the σ^* orbital (Section D).

A BENCHMARKING OF QUANTUM CHEMICAL METHODS ALONG PROTON TRANSFER

Scans of the O–H distance for phenol with one water molecule have been carried out with different methods. First, the energies calculated with CASSCF are presented (subsection A.1). Then, in subsection A.2, the effect of not including a level shift in the CASPT2 calculations will be investigated, followed by a discussion of the effects of increasing the size of the active space (subsection A.3).

In addition to the CASPT2 and ADC(2) results discussed in Section 3.1, scans have also been performed employing CC2 (subsection A.4) and TDDFT (subsection A.5). Additionally, the possibility to carry out optimizations in the ground state with CASSCF and DFT as an approximation to excited state optimizations has been investigated since excited-state optimizations including several water molecules turned out to be unfeasible (subsection A.6). For comparison of the height of the energy barrier, a scan of the O–H distance of gas-phase phenol has been carried out employing CASPT2/CASSCF (subsection A.7).

A.1 *CASSCF*

The geometries of the $\pi\sigma^*$ and the $\pi\pi^*$ state of phenol·(H_2O) were optimized with CASSCF(6,7). Thus, in addition to the CASPT2 energies discussed in Section 3.1.1, also CASSCF energies were obtained. Figure A.1 shows the O–H scan calculated with CASSCF. The height of the energy barrier (0.7 eV) agrees with the value calculated with CASPT2 (0.7 eV) while the O–H separation at the crossing is 0.11 Å shorter.

A.2 *CASPT2: Level shift*

In order to investigate the effect of the level shift on the CASPT2 calculations, test calculations without level shift were carried out for the ground-state optimized geometry and for several excited-state optimized geometries for the phenol·(H_2O) system. The excitation energies and reference weights of the three states, calculated at different O–H bond lengths, with and without level shift, for geometries optimized for the $\pi\sigma^*$

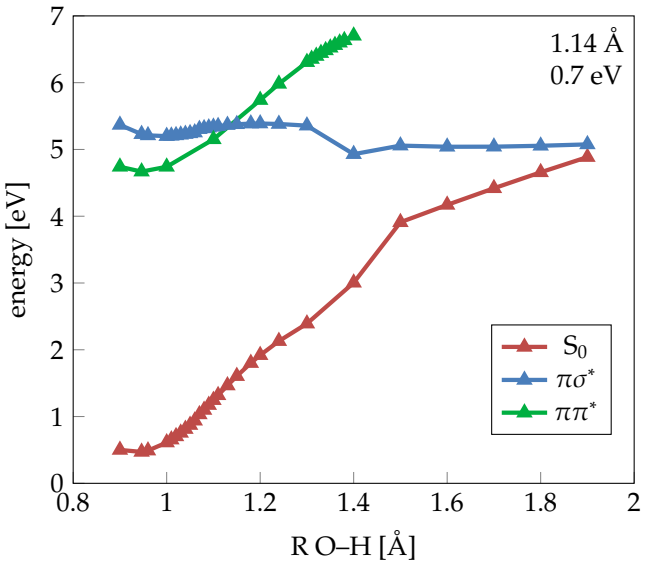

Figure A.1. O–H scan with geometries optimized in the $\pi\pi^*$ and $\pi\sigma^*$ states employing CASSCF(6,7), energies calculated with CASSCF. Numbers in the right corner give the O–H distance at the $\pi\pi^*/\pi\sigma^*$ crossing and the height of the energy barrier between these states.

state are shown in Figure A.2a and b, the values of the $\pi\pi^*$ optimized geometries are depicted in Figure A.2c and d. The values of the ground-state optimized geometry are listed in Table A.1.

Table A.1. Excitation energies and reference weights calculated for the ground-state optimized geometry with and without level shift.

		ex. energy [eV]		ref. weight	
level shift	S_1	S_2	S_0	S_1	S_2
0.3	4.45	5.66	0.77	0.75	0.76
none	4.61	5.62	0.73	0.67	0.70

Without level shift, for most geometries the reference weight (see Figure A.2b and d) of the $\pi\pi^*$ state is considerably smaller than that of the ground state and the $\pi\sigma^*$ state, indicating that intruder states are present. The energy of the $\pi\sigma^*$ state is only slightly (generally < 0.05 eV) shifted by including a level shift. In contrast, the energy of the $\pi\pi^*$ state is susceptible to the introduction of a level shift due to the removal of intruder states. With a level shift of 0.3, the reference weights of the three states are similar, suggesting that this value of the level shift is suited for the calculations.

A.3 *CASPT2(6,9)*

In order to investigate whether the size of the active space is sufficient, two additional σ^* orbitals were included in the active space and a scan of the O–H distance was performed with MS-CASPT2/SA-CASSCF for 6 states. The results are plotted in Figure A.3. The orbitals included in the (6,9) active space are depicted in Figure A.4.

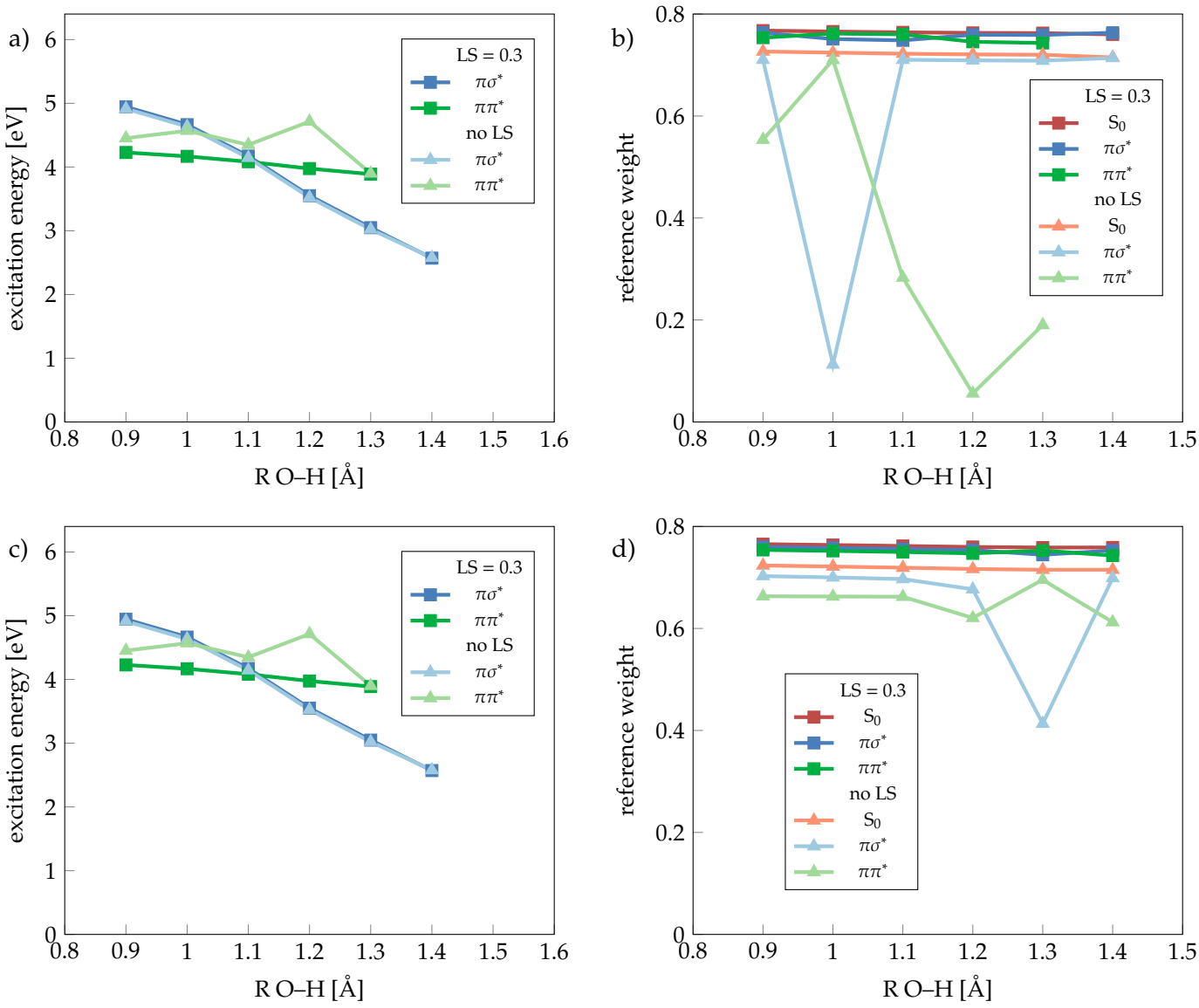

Figure A.2. Excitation energies and reference weights calculated for geometries optimized in the $\pi\sigma^*$ state (top) and the $\pi\pi^*$ state (bottom) with and without level shift (LS).

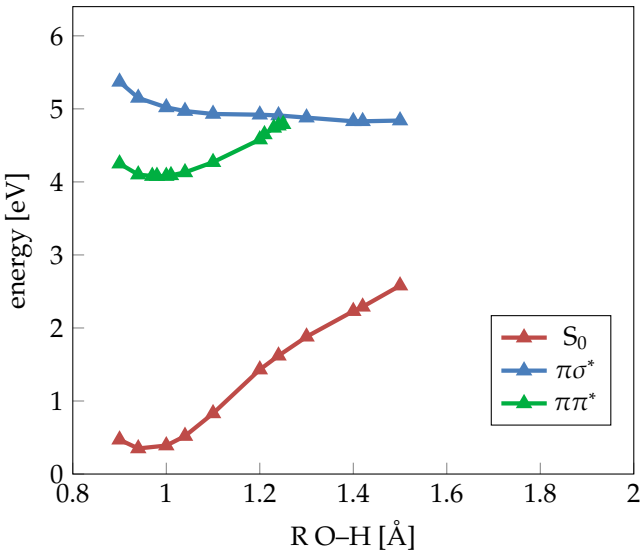

Figure A.3. O–H scan with geometries optimized in the $\pi\pi^*$ and $\pi\sigma^*$ states employing SA-CASSCF(6,9) for 6 states, energies calculated with MS-CASPT2.

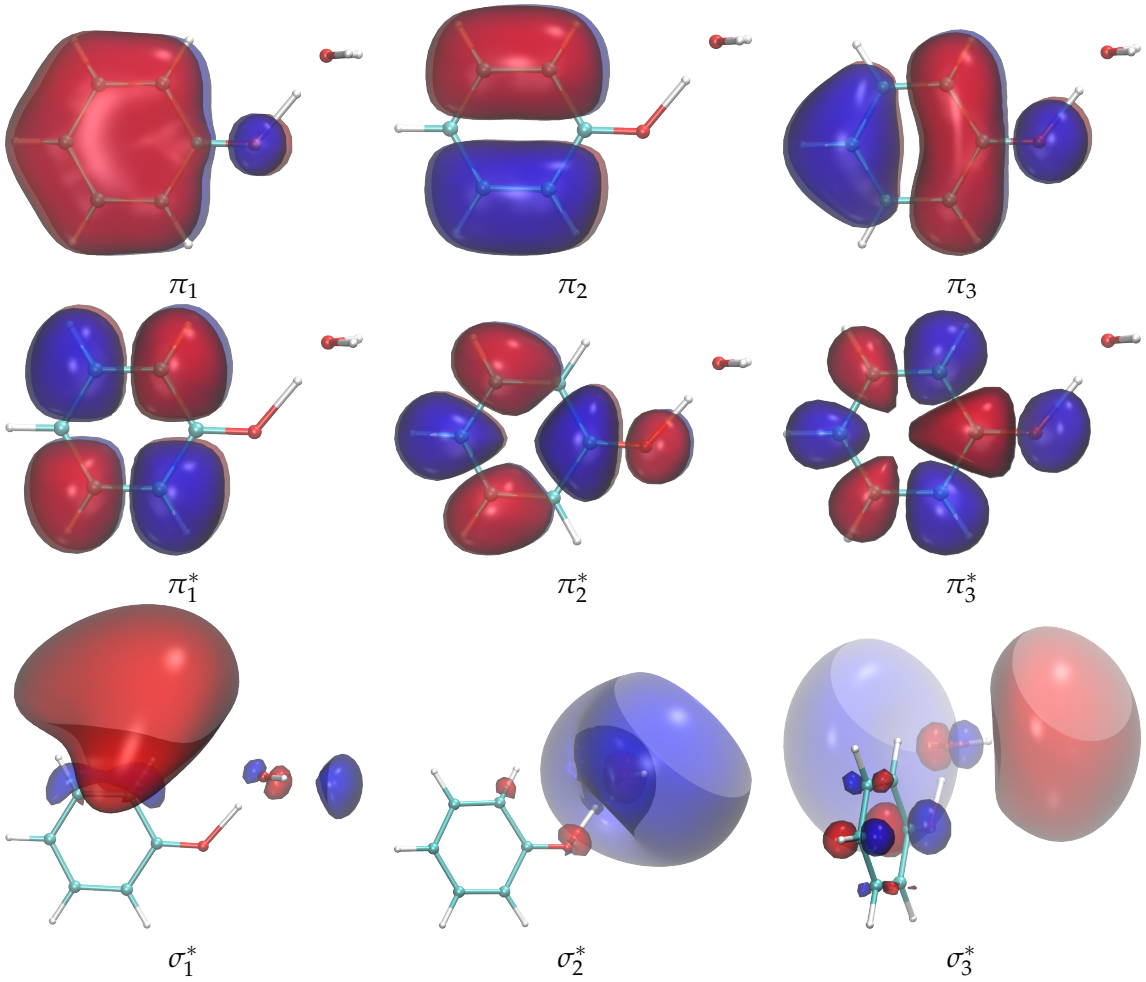

Figure A.4. (6,9) active space depicted for $\pi\sigma^*$ optimized geometry at O–H distance of 1.4 Å.

The scan computed with 7 active orbitals agrees very well with the results of the computations employing an active space size of 9 orbitals. This good agreement suggests that for the O–H reaction coordinate the (6, 7) active space is sufficiently large. The overestimation of the height of the energy barrier between the minimum of the $\pi\pi^*$ state and the conical intersection between $\pi\pi^*$ and $\pi\sigma^*$ state discussed in Section 3.1.1 is probably not due to an insufficiently large active space but rather due to the dynamical correlation computed in the CASPT2 calculation. However, no calculations with larger active spaces, including e. g. the corresponding σ orbitals, were carried out in this work.

A.4 CC2

The energies of the CASSCF-optimized geometries of the $\pi\pi^*$ and $\pi\sigma^*$ states were calculated with CC2[139] employing the Turbomole[126–130] program package with the aug-cc-pvdz basis set.[56,113–115] The results are shown in Figure A.5.

The O–H distance at the crossing calculated with CC2 of 1.07 Å agrees very well with the ADC(2) result of 1.08 Å. The height of the energy barrier of 0.13 eV is sligthly more underestimated than the ADC(2) barrier.

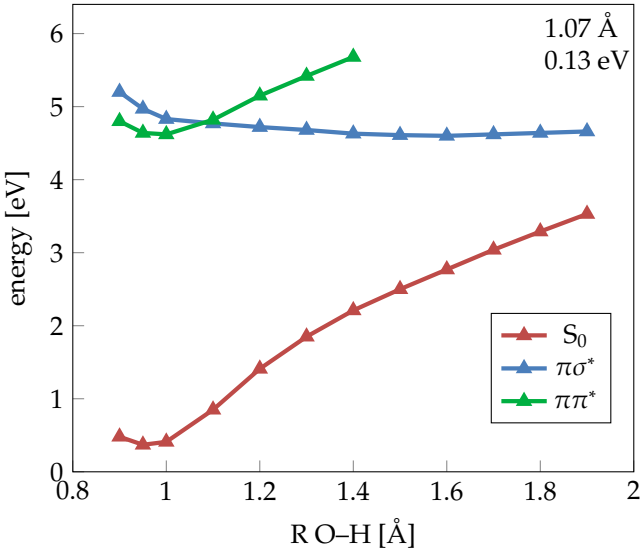

Figure A.5. Energies of the CASSCF-optimized geometries in the $\pi\pi^*$ and $\pi\sigma^*$ states calculated with CC2.

A.5 *TDDFT*

In order to compare the results of TDDFT with that of CASPT2/CASSCF and ADC(2), for phenol with one water molecule geometries at different O–H distances have been optimized in the $\pi\pi^*$ and $\pi\sigma^*$ states employing the ωB97XD functional[92] with the Gaussian 09[140] program package. The aug-cc-pvdz basis set[56,113–115] and the "Ultra-Fine" integration grid were used.

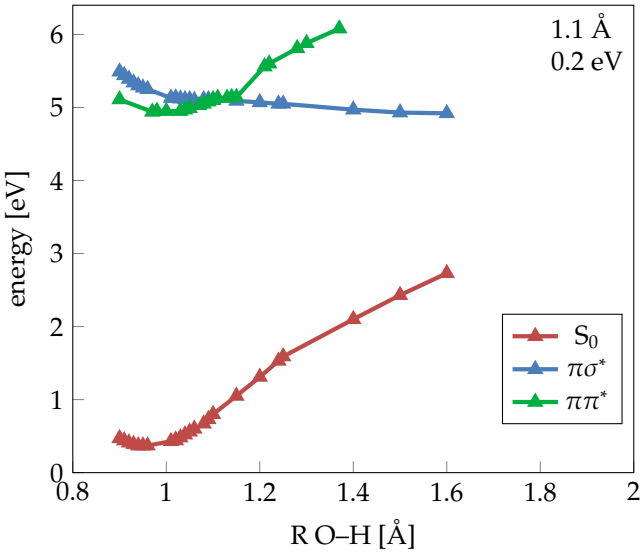

Figure A.6. O–H scan with geometries optimized in the $\pi\pi^*$ and $\pi\sigma^*$ states employing the ωB97XD functional, energies calculated at the same level of theory.

The O–H distance at the crossing is only 1.1 Å and thus 0.14 Å shorter than that calculated with CASPT2/CASSCF. Also, the energy barrier is only 0.2 eV, which is less than one third of the CASPT2 barrier. These results agree well with the ADC(2) values for crossing distance and energy barrier.

The energy barrier of 0.2 eV corresponds to a time scale of $\approx$ 0.37 ns and thus agrees better with the experimental time scale of 2 ns than the ADC(2) value. While TDDFT is able to describe phenol with a cluster size of one water molecule well, TDDFT tends to underestimate the energy of charge-transfer states.[89,91,141–143] This problem becomes

more prominent when the cluster size is increased. For this reason, ADC(2) rather than TDDFT was employed for the calculations on clusters comprised of 15 water molecules.

To investigate how well geometries optimized with TDDFT agree with CASSCF optimized geometries, the energies of the CASSCF-optimized geometries were calculated with the range-separated functionals ωB97XD[92] and CAM-B3LYP[91] (Figure A.7). Since DFT tends to underestimate the energy of charge-transfer states,[89,91,141–143] non-range-separated functionals seem less well suited for this system, and where therefore not tested. Additionally, the energies of the ωB97XD-optimized geometries of the O–H scan were computed with CASPT2 (Figure A.8).

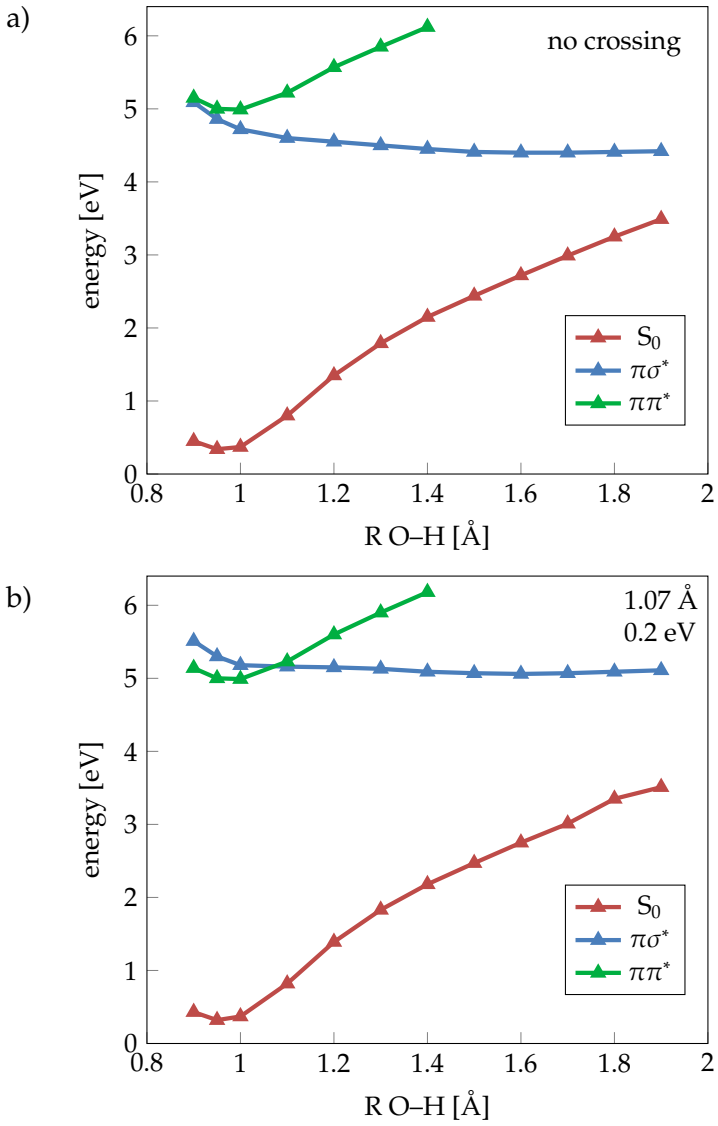

Figure A.7. O–H scan with geometries optimized with CASSCF, energies calculated with a) CAM-B3LYP, b) ωB97XD

CAM-B3LYP overestimates the $\pi\pi^*$ state to such an extent that even in the Franck-Condon region the $\pi\sigma^*$ state is the lowest excited state and there is no crossing between the states. The values obtained with ωB97XD for O–H distance at the crossing (1.07 Å) and energy barrier (0.2 eV) for the CASSCF-optimized geometries are similar to the values of the ωB97XD/ωB97XD calculation. Furthermore, the O–H distance (1.25 Å) and energy barrier (0.7 eV) from the CASPT2/ωB97XD calculation agree very well with the values obtained in the CASPT2/CASSCF calculation. These results suggest that ωB97XD is similarly well suited for geometry optimizations as CASSCF. Unfortunately, it was not possible to carry out geometry optimizations employing ωB97XD for excited

states with more water molecules since there exist many low-frequency modes which hinders the convergence of optimizations.

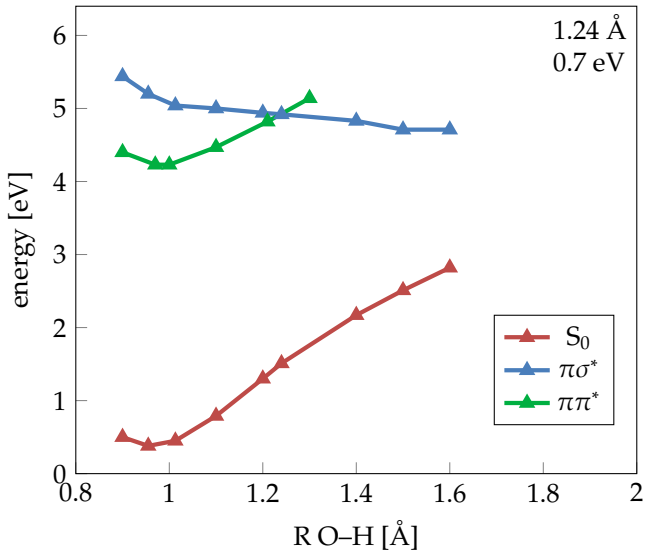

Figure A.8. O–H scan with geometries optimized with ωB97XD in the $\pi\pi^*$ and $\pi\sigma^*$ states, energies calculated with CASPT2.

To summarize, several methods have been employed to calculate the height of the energy barrier between the minimum of the $\pi\pi^*$ and the conical intersection between the $\pi\pi^*$ and $\pi\sigma^*$ states (see Table A.2). The fact that ADC(2), CC2 and ωB97XD agree very well indicates that ADC(2) accurately describes the system and can be employed for calculations including more water molecules. Due to the underestimation of charge-transfer states by TDDFT, which becomes more severe when the cluster size is increased, ωB97XD was not employed for the calculations including 15 water molecules.

Table A.2. O–H distance at the crossing between $\pi\pi^*$ and $\pi\sigma^*$ states (in Å) and height of the energy barrier between the minimum of the $\pi\pi^*$ state and the crossing between the $\pi\pi^*$ and $\pi\sigma^*$ states (in eV) calculated with different methods used for geometry optimizations and calculation of excitation energies.

method			
geometries opt.	energies	O–H distance	barrier
CASSCF(6,7)	CASPT2(6,7)	1.25	0.7
CASSCF(6,7)	ADC(2)	1.08	0.16
CASSCF(6,7)	CASSCF(6,7)	1.14	0.7
CASSCF(6,7)	CC2	1.07	0.13
ωB97XD	ωB97XD	1.1	0.2
CASSCF(6,7)	CAM-B3LYP	no crossing	
CASSCF(6,7)	ωB97XD	1.07	0.2
ωB97XD	CASPT2(6,7)	1.24	0.7

A.6 *CASSCF and DFT: Ground state optimizations*

Since excited-state optimizations for phenol with several water molecules turned out to be unfeasible, it was examined whether the approach to approximate excited-state optimized geometries by geometries optimized in the ground state[144] can be employed

for this system. For this purpose, geometries with different O–H distances were optimized with CASSCF and ωB97XD in the ground state. The resulting scans are shown in Figure A.9.

For the geometries optimized with CASSCF in the ground state, the values for bond distance at the crossing and energy barrier are 1.28 Å and 1.55 eV. Thus, the bond distance is 0.03 Å longer than the value obtained in the CASPT2 calculations on geometries optimized with CASSCF in the excited states while the energy barrier is more than twice as high. The values obtained in the ωB97XD/ωB97XD calculation for the ground state optimized geometries are 1.13 Å and 0.4 eV. Thus, while the O–H distance at the crossing agrees with the value obtained in the excited-state optimizations (see subsection A.5), the energy barrier is twice as high. The distance at the crossing and the barrier height from the CASPT2/ωB97XD calculation are 1.34 Å and 1.0 eV. These values do not agree with the CASPT2/CASSCF optimizations in the ground state, indicating that the ground-state optimized geometries differ more strongly between CASSCF and ωB97XD than the excited state optimized ones.

For none of the tested methods the values obtained for O–H distance at crossing and height of the energy barrier based on ground-state optimized geometries agree with values based on excited-state geometry optimizations. Therefore, the approach to use ground-state optimized geometries cannot be employed for the O–H reaction coordinate in phenol.

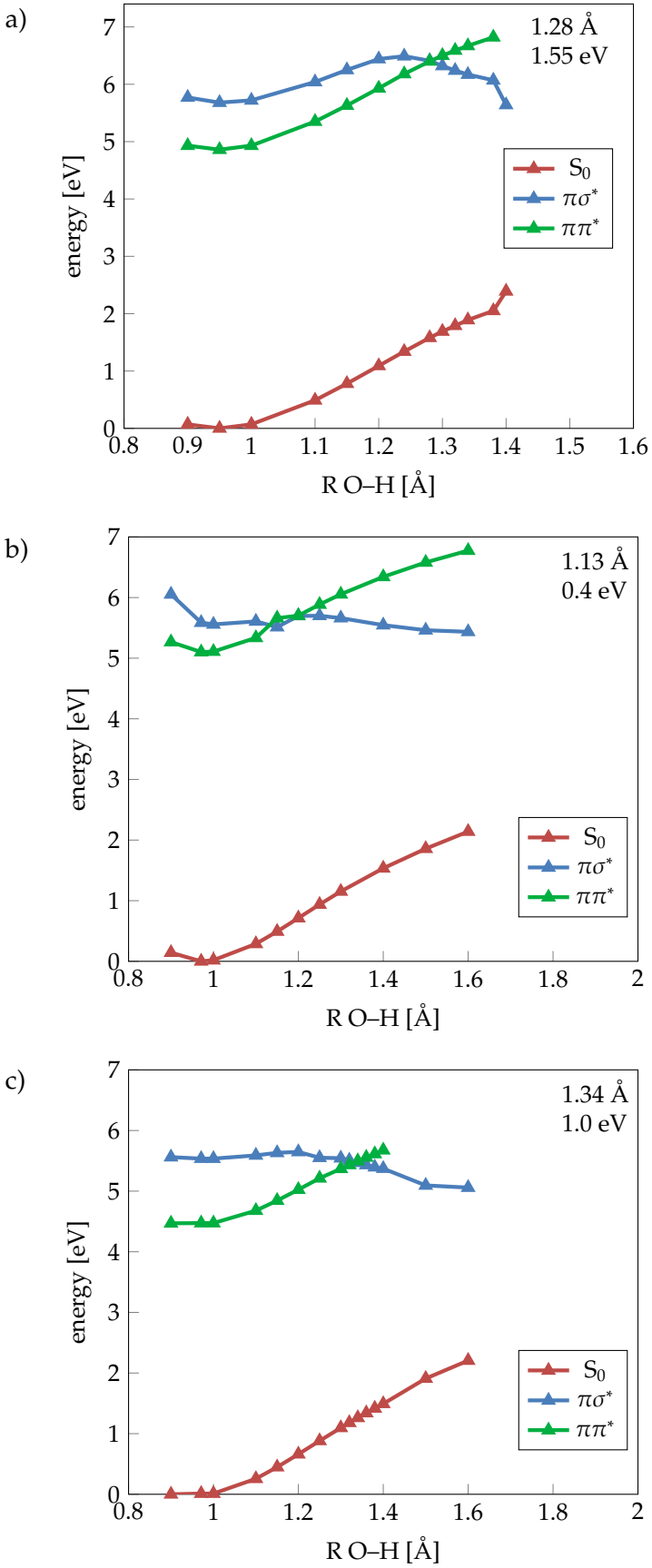

Figure A.9. a) MS-CASPT2(6,7) energies of geometries optimized employing SA-CASSCF(6,7) in the ground state. b,c) Energies calculated employing b) ωB97XD c) CASPT2(6,7) of geometries optimized with ωB97XD in the ground state.

In order to compare the height of the energy barrier between the $\pi\pi^*$ and $\pi\sigma^*$ states for phenol with one water molecule to the value in isolated phenol, a scan of the O–H distance for phenol in the gas phase has been carried out. The geometries of the $\pi\pi^*$ and $\pi\sigma^*$ states were optimized employing CASSCF(6,7). The energies were computed with CASPT2(6,7). The results are shown in Figure A.10.

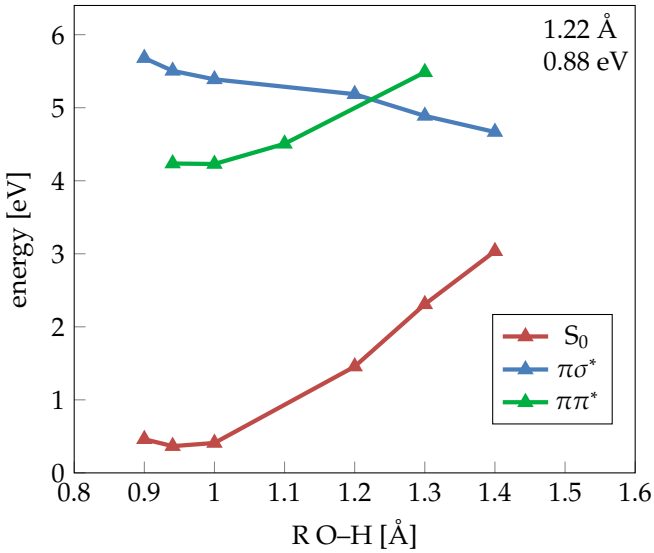

Figure A.10. CASPT2(6,7) energies of the geometries optimized with CASSCF(6,7) of the $\pi\pi^*$ and $\pi\sigma^*$ states of gas-phase phenol plotted relative to the ground-state optimized geometry; energies of S_0 were calculated at $\pi\sigma^*$-optimized geometries.

The O–H distance at the crossing is 1.22 Å, which is 0.03 Å smaller than the value calculated for phenol with one water molecule. The energy barrier between $\pi\pi^*$ and $\pi\sigma^*$ states is 0.88 eV, which is about 0.18 eV larger than the energy barrier for phenol with a cluster size of one water molecule.

The ground-state optimized value for the O–H distance for phenol in the gas phase (0.94039 Å) is slightly smaller than the O–H distance for phenol with one water molecule (0.94633 Å).

The electronic structure of the absorption spectrum and the density of states calculated with ADC(2) for phenol with cluster sizes of one, five and fifteen water molecules was analyzed in order to investigate the influence of the inclusion of larger numbers of water molecules on the occurence of $\pi\sigma^*$ states at low energies. The decomposed spectra and densities of states are plotted in Figure B.11. The $\pi\pi^*$ and $\pi\sigma^*$ states were identified as described in Section 3.2.2 by using two values from the TheoDORE wavefunction analysis, with $\pi\sigma^*$ states defined as excitations with a charge-transfer number > 0.5 and $\pi\pi^*$ states as having a charge-transfer number $\leqslant 0.5$ and a POS value $\leqslant 1.2$, i. e. excitations located at phenol.

The $\pi\sigma^*$ contribution to the spectrum increases slightly with increasing number of water molecules. For a cluster size of one water molecule, $\pi\sigma^*$ states contribute to about 1% to the spectrum, for five and fifteen water molecules, the percentage is 4% and 5%, respectively. However, the $\pi\sigma^*$ states are always mainly dark and direct excitation to the $\pi\sigma^*$ states is unlikely.

The $\pi\sigma^*$ contribution to the density of states is considerably larger. With one water molecule, $\pi\sigma^*$ states make up about 18% of the DOS. However, they are found mainly at the blue end of the spectrum at higher excitation energies than the peak of the $\pi\pi^*$ band. The $\pi\sigma^*$ fraction increases to 31% for a cluster size of five. In addition, a considerable amount of $\pi\sigma^*$ states is now found at lower energies. For the fifteen water molecules cluster, the percentage further increases slightly to 36%. The $\pi\sigma^*$ states extend even further to the red end of the spectrum. A considerable fraction of $\pi\sigma^*$ states has excitation energies below the maximum of the $\pi\pi^*$ band. These $\pi\sigma^*$ states can in principle be populated after excitation to the $\pi\pi^*$ state followed by internal conversion induced by reorganization of the solvent molecules without elongation of the O–H bond.

Figure B.12 shows the decomposition of the absorption spectrum and of the density of states calculated with CC2 for a cluster size of five water molecules.

The $\pi\sigma^*$ contribution to the CC2 spectrum of 4% is equal to the value in the ADC(2) calculation for the same solvent model. Also, the $\pi\sigma^*$ contribution to the density of states is equal with 31%, whereas the $\pi\pi^*$ contribution (58%) is slightly smaller. Thus, the decomposition of the spectrum agrees very well between CC2 and ADC(2).

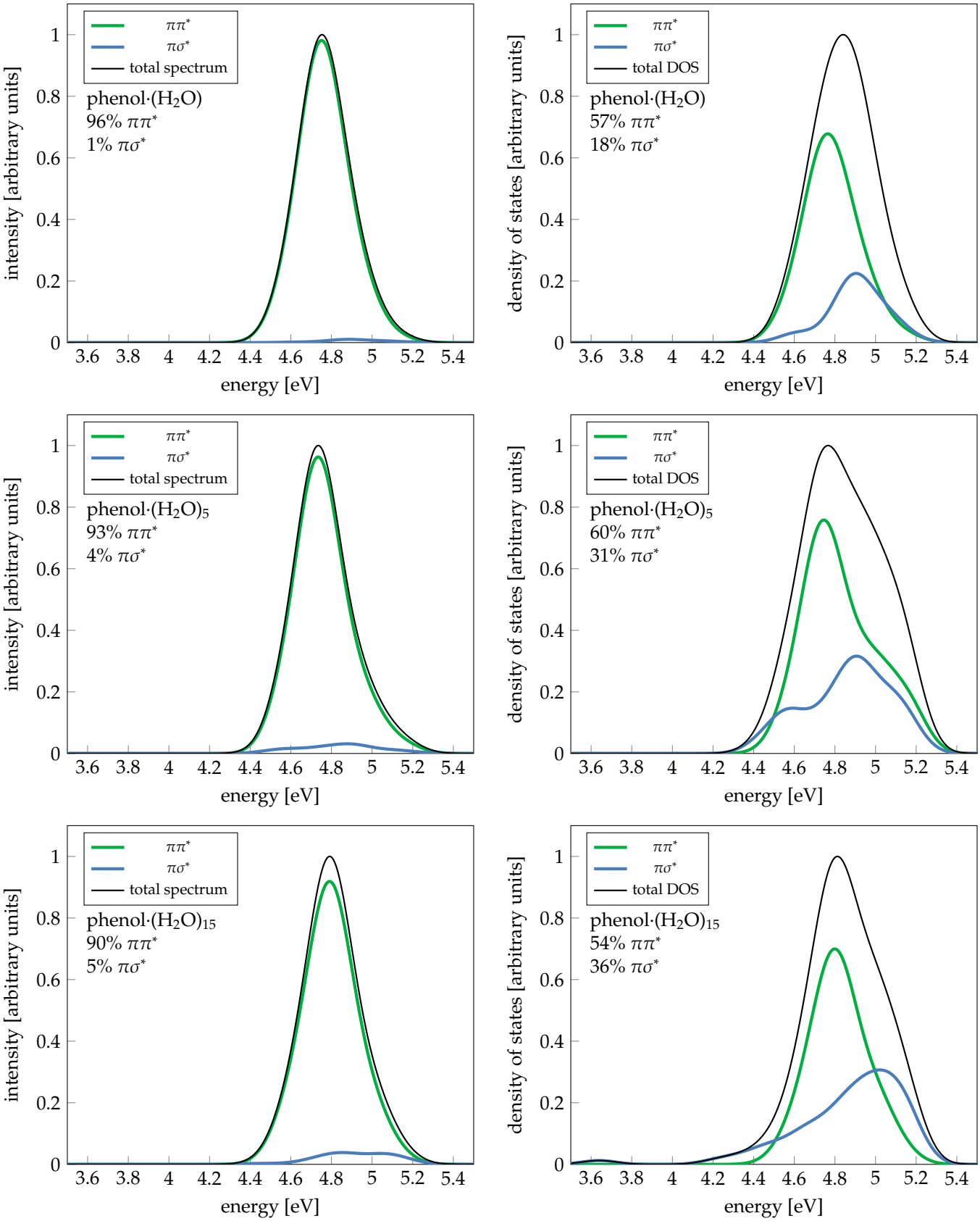

Figure B.11. Absorption spectrum and density of states below an energy threshold of 5.2 eV calculated with ADC(2) for phenol with water clusters consisting of one (top), five (middle) and fifteen (bottom) water molecules.

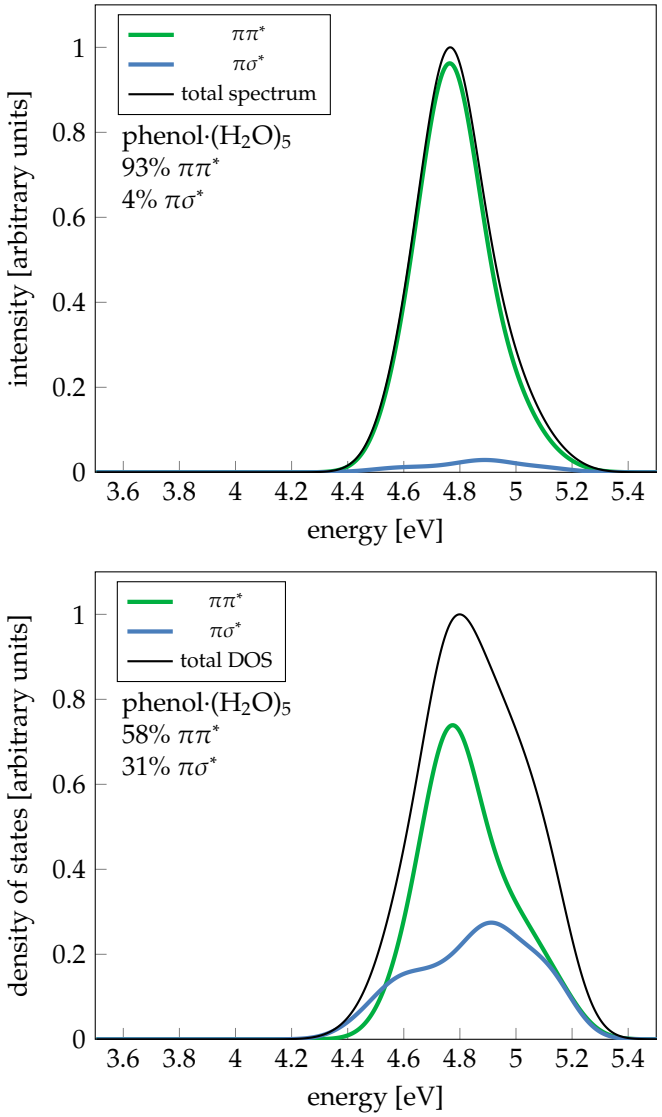

Figure B.12. Decomposition of the absorption spectrum and of the density of states below an energy threshold of 5.2 eV in $\pi\pi^*$ and $\pi\sigma^*$ states computed with CC2 for a cluster size of five water molecules.

In order to aid in the choice of a suitable computational model, absorption spectra were calculated with different methods and environment models based on up to 101 snapshots from the constrained molecular dynamics simulation. The energy at the maximum of the peak, the difference to experiment and to the value calculated in the gas phase with the respective method are listed in Table C.3. In the following, the plotted spectra will be shown and discussed.

Table C.3. Energy of the peak with highest intensity calculated with the different methods as well as the experimental value in eV. For comparison, the difference to experiment and the difference to the gas phase value, calculated with the respective method, is also listed.

Method	Environment description	Energy	Diff. to exp.	Diff. to gas phase
experiment		4.585		
CASPT2(6,6)	gas phase	4.488	−0.097	
CASPT2(6,6)	QM/MM	4.528	−0.057	0.040
CASPT2(6,6) IPEA	QM/MM	4.880	0.295	0.392
CASPT2(6,6)	1 water	4.428	−0.157	−0.060
CASPT2(6,6)	1 water, PCM	4.472	−0.113	−0.016
CASPT2(6,7)	1 water	4.368	−0.217	
CASPT2(6,7)	1 water, PCM	4.428	−0.157	
ADC(2)	gas phase	4.864	0.279	
ADC(2)	QM/MM	4.904	0.319	0.040
ADC(2)	COSMO	4.872	0.287	0.008
ADC(2)	1 water	4.752	0.167	−0.112
ADC(2)	5 water	4.736	0.151	−0.128
ADC(2)	15 water	4.792	0.207	−0.072
ADC(2)	1 water, COSMO	4.784	0.199	−0.08
ADC(2)	1 water, QM/MM	4.852	0.267	−0.012
CC2	gas phase	4.884	0.299	
CC2	QM/MM	4.924	0.339	0.040
CC2	5 water	4.764	0.179	−0.120

The gas phase spectra calculated with the different methods are shown in Figure C.13.

Compared to experiment, the CASPT2(6,6) spectrum, which was calculated with MOLCAS 8.0, is red-shifted by 0.097 eV. The ADC(2) and CC2 spectra agree very well with each other. Both spectra are blue-shifted by 0.279 and 0.299 eV compared to experiment, respectively. The underestimation of the energy of the $\pi\pi^*$ state by CASPT2 agrees with the overestimation of the height of the energy barrier between $\pi\pi^*$ and $\pi\sigma^*$ state described in Section 3.1.1. In contrast, ADC(2) overestimates the energy of the $\pi\pi^*$ state and therefore underestimates the height of the energy barrier, as described in Section 3.1.2.

Figure C.14 shows spectra calculated with several environment models employing ADC(2) and CC2.

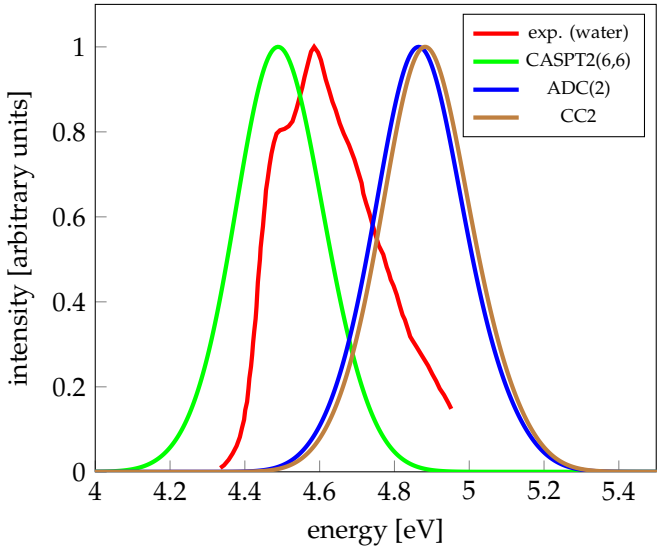

Figure C.13. Absorption spectra of phenol in the gas phase based on 101 snapshots from a MD simulation calculated with different methods.

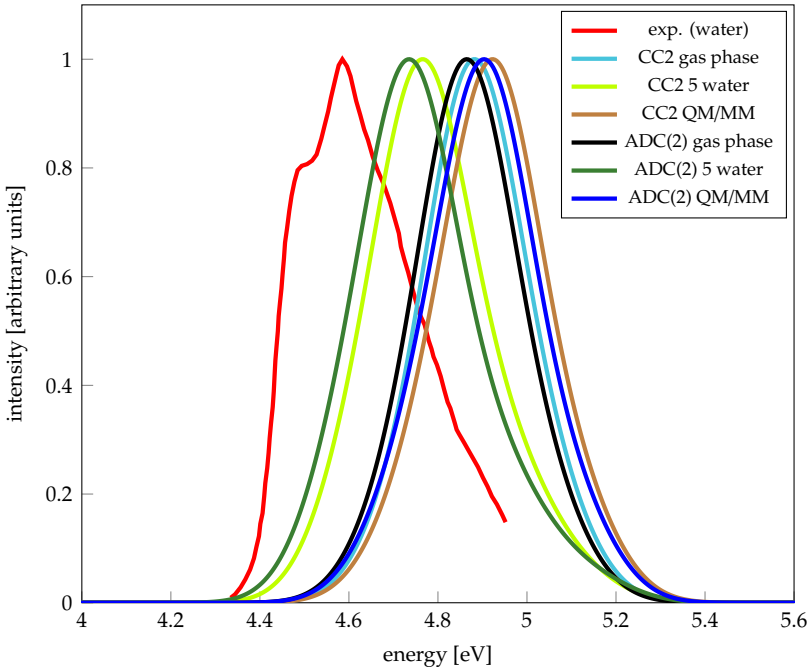

Figure C.14. Absorption spectra calculated with different environment models employing ADC(2) and CC2.

The ADC(2) gas phase spectrum is red-shifted by 0.02 eV compared to the CC2 spectrum. The ADC(2) spectrum with a cluster size of five water molecules is red-shifted by 0.028 eV and the ADC(2)/MM spectrum is red-shifted by 0.02 eV compared to the corresponding CC2 spectra, respectively. Thus, the ADC(2) and CC2 spectra calculated with the same environment model agree very well with each other.

To demonstrate the effect of the choice of the active space, Figures C.15 and C.16 show the spectra calculated with CASPT2(6,7) and CASPT2(6,6) for one water molecule in the gas phase and with PCM, respectively, which were calculated with a development version of MOLCAS that supports wavefunction analysis by the library libwfa.

The CASPT2(6,7) spectrum for a cluster size of one water molecule, peaking at an excitation energy of 4.368 eV, is red-shifted by 0.06 eV compared to the CASPT2(6,6) spectrum, which has a maximum at 4.428 eV. When including the PCM model, the

CASPT2(6,7) spectrum peaks at 4.428 eV while the CASPT2(6,6) spectrum has a maximum at 4.472 eV. Again, the CASPT2(6,7) spectrum is red-shifted by 0.044 eV. Thus, including the σ^* orbital in the active space leads to a lowering of the excitation energy of the $\pi\pi^*$ state.

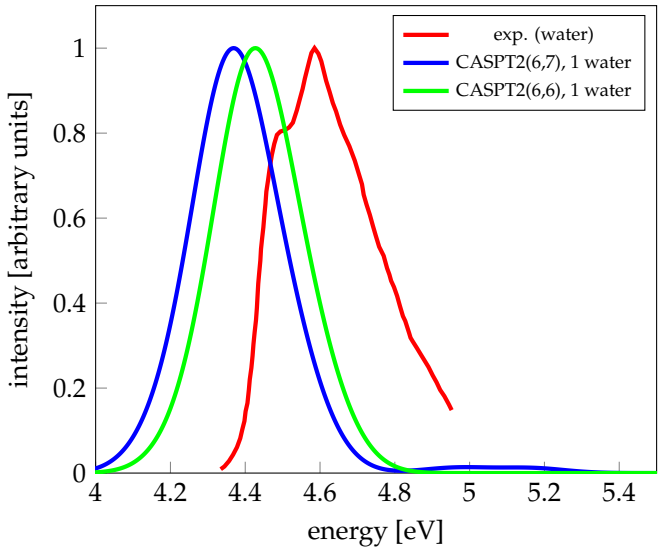

Figure C.15. Spectra calculated with CASPT2(6,7) and CASPT2(6,6) with one water molecule in the gas phase.

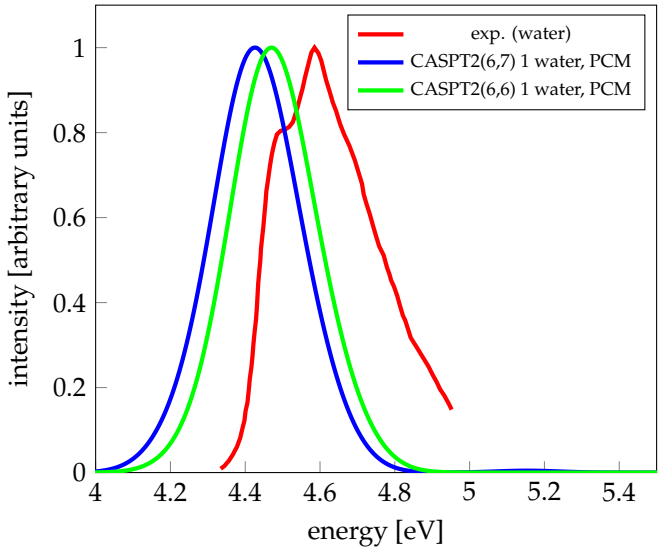

Figure C.16. Spectra calculated with CASPT2(6,7) and CASPT2(6,6) with one water molecule with PCM.

To highlight the effect of including a continuum model, the same spectra are plotted together in Figure C.17.

When including the PCM solvation model, the CASPT2(6,6) spectrum is blue-shifted by 0.044 eV with respect to the gas-phase spectrum. The CASPT2(6,7) spectrum with PCM is blue-shifted by 0.06 eV compared to the gas-phase spectrum. Incidentally, the CASPT2(6,6) gas phase spectrum and the CASPT2(6,7) spectrum with PCM overlap, both peaking at 4.428 eV.

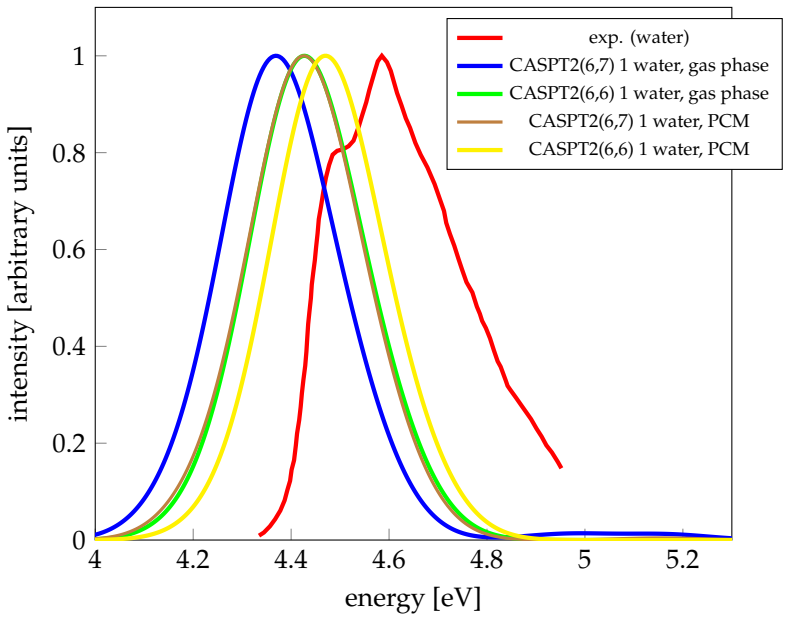

Figure C.17. Spectra calculated with CASPT2(6,7) and CASPT2(6,6) with one water molecule with and without PCM.

Figure C.18 shows the spectra calculated with ADC(2) for cluster sizes of zero and one water molecule with and without the COSMO solvation model.

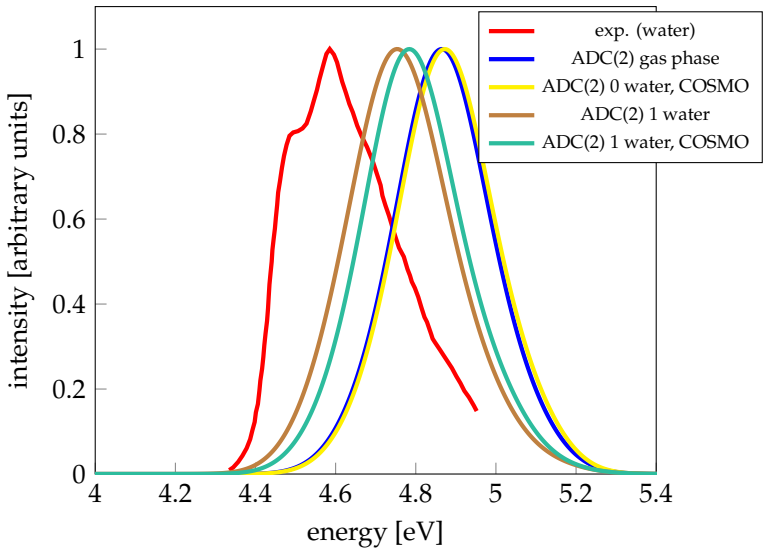

Figure C.18. Spectra calculated with ADC(2) for phenol with zero or one water molecule with or without COSMO.

The ADC(2) spectrum calculated with the COSMO solvation model is slightly (0.008 eV) blue-shifted compared to the gas-phase spectrum.

The spectrum calculated for a cluster size of one water molecule using the COSMO solvation model is blue-shifted by 0.032 eV compared to the corresponding gas-phase spectrum.

Figure C.19 shows the absorption spectra calculated with CASPT2(6,6) with different environment models, calculated with MOLCAS 8.0.

The spectrum calculated with one explicitely treated water molecule, peaking at 4.428 eV, is red-shifted with respect to the gas-phase spectrum, which has a maximum at 4.488 eV. Thus, including one water molecule increases the difference to experiment from 0.097 eV to 0.157 eV. The QM/MM spectrum, which has a maximum at 4.528 eV, is

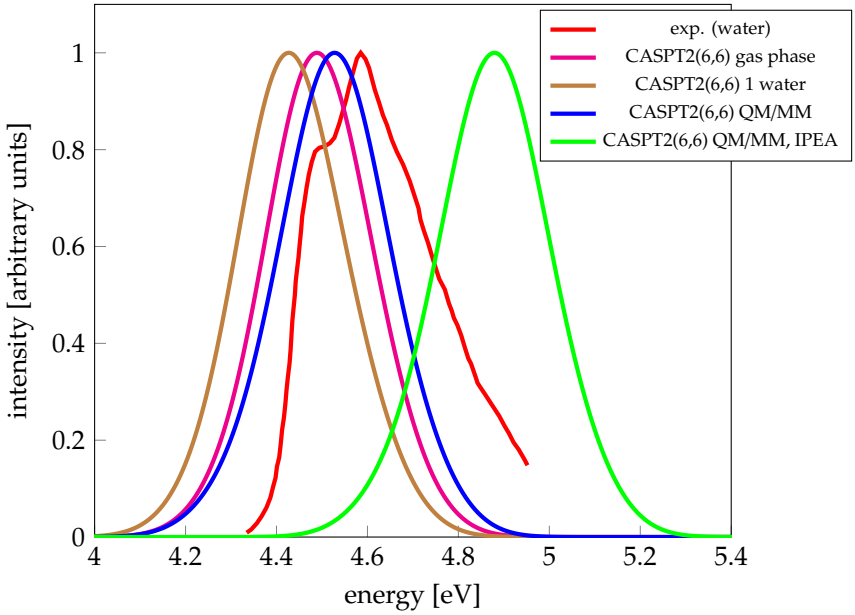

Figure C.19. Absorption spectra calculated with CASPT2(6,6) with different environment models.

blue-shifted by 0.04 eV with respect to the gas-phase spectrum, reducing the distance to experiment to 0.057 eV. For comparison, a calculation with the default IPEA shift was carried out. The QM/MM spectrum with IPEA shift is blue-shifted compared to the QM/MM spectrum without IPEA shift by 0.352 eV. The difference to experiment with IPEA is increased to 0.295 eV.

As described in Section 3.2.3, a lower excitation energy of charge-transfer states is associated with a larger number of water molecules containing more than 10% of electron population. In order to further investigate the correlation between the number of water molecules in proximity to the σ^* orbital and the excitation energy, the number of water molecules within a radius of 3 Å around the approximate position of the orbital, which was defined as discussed in Section 3.2.3 as the center of mass of the water molecules containing more than 10% of electron population, was determined. To simplify the calculations, the distances to the oxygen atoms of the water molecules instead of their centers of mass were used. The results are plotted in Figure D.20. The number of states for the different numbers of water molecules are listed in Table D.4. The seven states with zero water molecules containing more than 10% of electron population were not considered for this further analysis since the definition of the approximate position of the σ^* orbital could not be used. Furthermore, only excitation energy averages calculated for at least ten states are considered in the analysis.

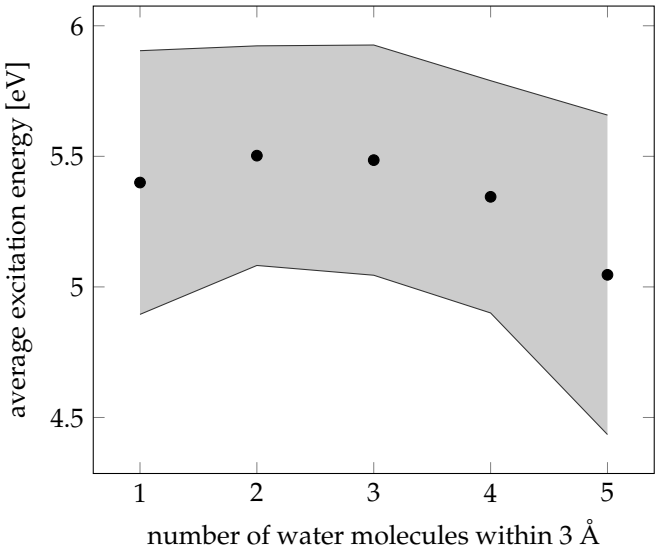

Figure D.20. Average of the excitation energy for charge-transfer states with different numbers of water molecules within 3 Å around the approximate position of the σ^* orbital. The standard deviation is indicated by the shaded area. Only excitation energy averages calculated for at least ten states are considered.

Table D.4. Number of states with different numbers of water molecules within 3 Å of the approximate position of the σ^* orbital.

1	2	3	4	5
11	81	90	46	10

From one to two water molecules the average excitation energy increases while from two to five water molecules the trend shows a decrease of the excitation energy with increasing number of water molecules within 3 Å of the approximate position of the σ^* orbital, in accordance with the result that the excitation energy decreases with increasing number of water molecules with an electron population $> 10\%$ (see Section 3.2.3).

[1] Barry, B. A. The role of redox-active amino acids in the photosynthetic water-oxidizing complex. *Photochem. Photobiol.* **1993**, *57*, 179–188.

[2] Sobolewski, A. L.; Domcke, W. Photoinduced Electron and Proton Transfer in Phenol and Its Clusters with Water and Ammonia. *J. Phys. Chem. A* **2001**, *105*, 9275–9283.

[3] Sobolewski, A. L.; Domcke, W.; Dedonder-Lardeuxc, C.; Jouvet, C. Excited-state hydrogen detachment and hydrogen transfer driven by repulsive $^1\pi\sigma^*$ states: A new paradigm for nonradiative decay in aromatic biomolecules. *Phys. Chem. Chem. Phys.* **2002**, *4*, 1093–1100.

[4] Domcke, W.; Sobolewski, A. L. Unraveling the Molecular Mechanisms of Photoacidity. *Science* **2003**, *302*, 1693–1694.

[5] Lan, Z.; Domcke, W.; Vallet, V.; Sobolewski, A. L.; Mahapatra, S. Time-dependent quantum wave-packet description of the $^1\pi\sigma^*$ photochemistry of phenol. *J. Chem. Phys.* **2005**, *122*, 224315.

[6] Vieuxmaire, O. P. J.; Lan, Z.; Sobolewski, A. L.; Domcke, W. Ab initio characterization of the conical intersections involved in the photochemistry of phenol. *J. Chem. Phys.* **2008**, *129*, 224307.

[7] Arnaut, L. G.; Formosinho, S. J. Excited-state proton transfer reactions I. Fundamentals and intermolecular reactions. *J. Photochem. Photobiol. A* **1993**, *75*, 1–20.

[8] Oliver, T. A. A.; Zhang, Y.; Roy, A.; Ashfold, M. N. R.; Bradforth, S. E. Exploring Autoionization and Photoinduced Proton-Coupled Electron Transfer Pathways of Phenol in Aqueous Solution. *J. Phys. Chem. Lett.* **2015**, *6*, 4159–4164.

[9] Dixon, R. N.; Oliver, T. A. A.; Ashfold, M. N. R. Tunnelling under a conical intersection: Application to the product vibrational state distributions in the UV photodissociation of phenols. *J. Chem. Phys.* **2011**, *134*, 194303.

[10] Iqbal, A.; Pegg, L.-J.; Stavros, V. G. Direct versus Indirect H Atom Elimination from Photoexcited Phenol Molecules. *J. Phys. Chem. A* **2008**, *112*, 9531–9534.

[11] Tseng, C.-M.; Lee, Y. T.; Ni, C.-K. H atom elimination from the $\pi\sigma^*$ state in the photodissociation of phenol. *J. Chem. Phys.* **2004**, *121*, 2459–2461.

[12] Nix, M. G. D.; Devine, A. L.; Cronin, B.; Dixon, R. N.; Ashfold, M. N. R. High resolution photofragment translational spectroscopy studies of the near ultraviolet photolysis of phenol. *J. Chem. Phys.* **2006**, *125*, 133318.

[13] Iqbal, A.; Cheung, M. S. Y.; Nix, M. G. D.; Stavros, V. G. Exploring the Time-Scales of H-Atom Detachment from Photoexcited Phenol-h_6 and Phenol-d_5: Statistical vs Nonstatistical Decay. *J. Phys. Chem. A* **2009**, *113*, 8157–8163.

[14] Roberts, G. M.; Chatterley, A. S.; Young, J. D.; Stavros, V. G. Direct Observation of Hydrogen Tunneling Dynamics in Photoexcited Phenol. *J. Phys. Chem. Lett.* **2012**, *3*, 348–352.

[15] Lipert, R. J.; Bermudez, G.; Colson, S. D. Pathways of S1 Decay in Phenol, Indoles, and Water Complexes of Phenol and Indole in a Free Jet Expansion. *J. Phys. Chem.* **1988**, *92*, 3801–3805.

[16] Lipert, R. J.; Colson, S. D. Time-Resolved Pump-Probe Photoionization Study of Excited-State Dynamics of Phenol-$(H_2O)_2$ and Phenol-$(H_2O)_3$. *J . Phys. Chem.* **1990**, *94*, 2358–2361.

[17] Lipert, R. J.; Colson, S. D. Deuterium Isotope Effects on S, Radiationless Decay in Phenol and on Intermolecular Vibrations in the Phenol-Water Complex. *J. Phys. Chem.* **1989**, *93*, 135–139.

[18] Lipert, R.; Colson, S. Low frequency vibrations in phenol-$(H_2O)_2$ revealed by hole-burning spectroscopy in a supersonic jet. *Chem. Phys. Lett.* **1989**, *161*, 303–307.

[19] Ratzer, C.; Küpper, J.; Spangenberg, D.; Schmitt, M. The structure of phenol in the S1-state determined by high resolution UV-spectroscopy. *Chem. Phys.* **2002**, *283*, 153–169.

[20] Köhler, G.; Kittel, G.; Getoff, N. Decay processes of singlet excited phenol in solution. *J. Photochem.* **1982**, *18*, 19–27.

[21] Hermann, R.; Mahalaxmi, G. R.; Jochum, T.; Naumov, S.; Brede, O. Balance of the Deactivation Channels of the First Excited Singlet State of Phenols: Effect of Alkyl Substitution, Sterical Hindrance, and Solvent Polarity. *J. Phys. Chem. A* **2002**, *106*, 1379–2389.

[22] Zhang, Y.; Oliver, T. A. A.; Ashfold, M. N. R.; Bradforth, S. E. Contrasting the excited state reaction pathways of phenol and para-methylthiophenol in the gas and liquid phases. *Faraday Discuss.* **2012**, *157*, 141–163.

[23] Arrhenius, S. Über die Reaktionsgeschwindigkeit bei der Inversion von Rohrzucker durch Säuren. *Z. Phys. Chem.* **1889**, *4*, 226–248.

[24] Nogueira, J. J.; Corani, A.; Nahhas, A. E.; Pezzella, A.; d'Ischia, M.; González, L.; Sundström, V. Sequential Proton-Coupled Electron Transfer Mediates Excited-State Deactivation of a Eumelanin Building Block. *J. Phys. Chem. Lett.* **2017**, *8*, 1004–1008.

[25] d'Ischia, M.; Napolitano, A.; Pezzella, A.; Meredith, P.; Sarna, T. Chemical and structural diversity in eumelanins: Unexplored biooptoelectronic materials. *Angew. Chem., Int. Ed.* **2009**, *48*, 3914–3921.

[26] Prota, G. *Melanins and Melanogenesis*; Academic Press: San Diego, CA, 1992.

[27] Meredith, P.; Sarna, T. The physical and chemical properties of eumelanin. *Pigm. Cell Res.* **2006**, *19*, 572–594.

[28] Adcock, S. A.; McCammon, J. A. Molecular Dynamics: Survey of Methods for Simulating the Activity of Proteins. *Chem. Rev.* **2006**, *106*, 1589–1615.

[29] Leach, A. R. *Molecular Modelling - Principles and Applications*; Prentice Hall, 2001.

[30] Verlet, L. Computer "Experiments" on Classical Fluids. I. Thermodynamical Properties of Lennard-Jones Molecules. *Phys. Rev.* **1967**, *159*, 98–103.

[31] Hockney, R. The potential calculation and some applications. *Methods Comput. Phys.* **1970**, *9*, 136–211.

[32] Swope, W.; Andersen, H.; Berens, P.; K.R., W. A computer simulation method for the calculation of equilibrium constants for the formation of physical clusters of molecules: Application to small water clusters. *J. Chem. Phys.* **1982**, *76*, 637–649.

[33] Jones, J. On the Determination of Molecular Fields. II. From the Equation of State of a Gas. *Proc. R. Soc. Lond. A* **1924**, *106*, 463–477.

[34] Jensen, F. *Introduction to Computational Chemistry*; John Wiley & Sons, 2007.

[35] Ewald, P. Die Berechnung optischer und elektrostatischer Gitterpotentiale. *Ann. Phys.* **1921**, *369*, 253–287.

[36] Darden, T.; York, D.; Pedersen, L. Particle Mesh Ewald: An N Log(N) method for Ewald sums in large systems. *J. Chem. Phys.* **1993**, *98*, 10089–10092.

[37] Essmann, U.; Perera, L.; Berkowitz, M. L. A smooth particle mesh Ewald method. *J. Chem. Phys.* **1995**, *103*, 8577–8593.

[38] Crowley, M. F.; Darden, T. A.; Cheatham III, T. E.; Deerfield II, D. W. Adventures in Improving the Scaling and Accuracy of a Parallel Molecular Dynamics Program. *J. Supercomput.* **1997**, *11*, 255–278.

[39] Hünenberger, P. *Advanced Computer Simulation: Approaches for Soft Matter Sciences I*; Advances in Polymer Science; Springer, 2005; Vol. 173; pp 105–149.

[40] Andersen, H. C. Molecular dynamics simulations at constant pressure and/or temperature. *J. Chem. Phys.* **1980**, *72*, 2384–2393.

[41] Berendsen, H. J. C.; Postma, J. P. M.; van Gunsteren, W. F.; DiNola, A.; Haak, J. R. Molecular dynamics with coupling to an external bath. *J. Chem. Phys.* **1984**, *81*, 3684–3690.

[42] Hoover, W. G. Canonical dynamics: Equilibrium phase-space distributions. *Phys. Rev. A* **1985**, *31*, 1695–1697.

[43] Hoover, W. G. Constant-pressure equations of motion. *Phys. Rev. A* **1986**, *34*, 2499–2500.

[44] Melchionna, S.; Ciccotti, G.; Holian, B. L. Hoover NPT dynamics for systems varying in shape and size. *Mol. Phys.* **1993**, *78*, 533–544.

[45] Feller, S. E.; Zhang, Y.; Pastor, R. W. Constant pressure molecular dynamics simulation: The Langevin piston method. *J. Chem. Phys.* **1995**, *103*, 4613–4621.

[46] Martyna, G. J.; Tobias, D. J.; Klein, M. L. Constant pressure molecular dynamics algorithms. *J. Chem. Phys.* **1994**, *101*, 4177–4189.

[47] Martyna, G. J.; Tuckerman, M. E.; Tobias, D. J.; Klein, M. L. Explicit reversible integrators for extended systems dynamics. *Mol. Phys.* **1996**, *87*, 1117–1157.

[48] Quigley, D.; Probert, M. I. J. Langevin dynamics in constant pressure extended systems. *J. Chem. Phys.* **2004**, *120*, 11432–11441.

[49] Rogge, S.; Vanduyfhuys, L.; Ghysels, A.; Waroquier, M.; Verstraelen, T.; Maurin, G.; Van Speybroeck, V. A Comparison of Barostats for the Mechanical Characterization of Metal–Organic Frameworks. *J. Chem. Theory Comput.* **2015**, *11*, 5583–5597.

[50] Grest, G. S.; Kremer, K. Molecular dynamics simulation for polymers in the presence of a heat bath. *Phys. Rev. A* **1986**, *33*, 3628–3631.

[51] Cerutti, D. S.; Duke, R.; Freddolino, P. L.; Fan, H.; Lybrand, T. P. Vulnerability in Popular Molecular Dynamics Packages Concerning Langevin and Andersen Dynamics. *J. Chem. Theory Comput.* **2008**, *4*, 1669–1680.

[52] Lion, T. W.; Allen, R. J. Computing the local pressure in molecular dynamics simulations. *J. Phys.: Condens. Matter* **2012**, *24*, 284133.

[53] Schrödinger, E. Quantisierung als Eigenwertproblem. *Ann. Phys.* **1926**, *384*, 361–376.

[54] Szabo, A.; Ostlund, N. S. *Modern Quantum Chemistry*; Dover publications, 1996.

[55] Born, M.; Oppenheimer, R. Zur Quantentheorie der Molekeln. *Ann. Phys.* **1927**, *389*, 457–484.

[56] T.H. Dunning, J. Gaussian basis sets for use in correlated molecular calculations. I. The atoms boron through neon and hydrogen. *J. Chem. Phys.* **1989**, *90*, 1007–1023.

[57] Almlöf, J.; Taylor, P. R. General contraction of Gaussian basis sets. I. Atomic natural orbitals for first- and second-row atoms. *J. Chem. Phys.* **1987**, *86*, 4070–4077.

[58] Ditchfield, R.; Hehre, W. J.; Pople, J. A. Self-Consistent Molecular-Orbital Methods. IX. An Extended Gaussian-Type Basis for Molecular-Orbital Studies of Organic Molecules. *J. Chem. Phys.* **1971**, *54*, 724–728.

[59] Roos, B. O. *Lecture Notes in Quantum Chemistry: European Summer School in Quantum Chemistry*; Lecture Notes in Chemistry; Springer, 1992; pp 177–254.

[60] Siegbahn, P. E. M. Generalizations of the direct CI method based on the graphical unitary group approach. I. Single replacements from a complete CI root function of any spin, first order wave functions. *J. Chem. Phys.* **1979**, *70*, 5391–5397.

[61] Roos, B. O.; Taylor, P. R.; Siegbahn, P. E. A complete active space SCF method (CASSCF) using a density matrix formulated super-CI approach. *Chem. Phys.* **1980**, *48*, 157–173.

[62] Paldus, J. Group theoretical approach to the configuration interaction and perturbation theory calculations for atomic and molecular systems. *J. Chem. Phys.* **1974**, *61*, 5321–5330.

[63] Andersson, K.; Malmqvist, P. A.; Roos, B. O.; Sadlej, A. J.; Wolinski, K. Second-order perturbation theory with a CASSCF reference function. *J. Phys. Chem.* **1990**, *94*, 5483–5488.

[64] Andersson, K.; Malmqvist, P.; Roos, B. O. Second-order perturbation theory with a complete active space self-consistent field reference function. *J. Chem. Phys.* **1992**, *96*, 1218–1226.

[65] Angeli, C.; Cimiraglia, R.; Evangelisti, S.; Leininger, T.; Malrieu, J.-P. Introduction of n-electron valence states for multireference perturbation theory. *J. Chem. Phys.* **2001**, *114*, 10252–10264.

[66] Angeli, C.; Cimiraglia, R.; Malrieu, J.-P. N-electron valence state perturbation theory: a fast implementation of the strongly contracted variant. *Chem. Phys. Lett.* **2001**, *350*, 297–305.

[67] Angeli, C.; Cimiraglia, R.; Malrieu, J.-P. n-electron valence state perturbation theory: A spinless formulation and an efficient implementation of the strongly contracted and of the partially contracted variants. *J. Chem. Phys.* **2002**, *117*, 9138–9153.

[68] Levine, I. N. *Quantum Chemistry*; Prentice Hall, 2000.

[69] Roos, B. O.; Andersson, K. Multiconfigurational perturbation theory with level shift - the Cr_2 potential revisited. *Chem. Phys. Lett.* **1995**, *245*, 215–223.

[70] Roos, B. O.; Andersson, K.; Fiilscher, M. P.; Serrano-Andres, L.; Pierloot, K.; Merchan, M.; Molina, V. Applications of level shift corrected perturbation theory in electronic spectroscopy. *J. Mol. Struct. (Theochem)* **1996**, *388*, 257–276.

[71] Roos, B. O. In *Radiation Induced Phenomena in Nucleic Acids*; Shukla, M. K., Leszczynski, J., Eds.; Challenges and Advances in Computational Chemistry and Physics; Springer, 2008; Vol. 5; pp 125–156.

[72] Schirmer, J. Beyond the random-phase approximation: A new approximation scheme for the polarization propagator. *Phys. Rev. A* **1982**, *26*, 2395–2416.

[73] Dreuw, A.; Wormit, M. The algebraic diagrammatic construction scheme for the polarization propagator for the calculation of excited states. *WIREs Comput. Mol. Sci.* **2015**, *5*, 82–95.

[74] Oddershede, J. In *Methods in Computational Molecular Physics*; Saunders, V. R., Diercksen, G. H. F., Wilson, S., Eds.; Springer, 1983; pp 249–270.

[75] Oddershede, J.; Jørgensen, P.; Beebe, N. Coupled hartree-fock and second order polarization propagator calculations of indirect nuclear spin-spin coupling constants for diatomic molecules. *Chem. Phys.* **1977**, *25*, 451–458.

[76] Dickhoff, W. H.; Neck, D. V. *Many-Body Theory Exposed! Propagator description of quantum mechanics in many-body systems*; World Scientific, 2005.

[77] Ho-Kim, Q.; Pham, X.-Y. *Elementary Particles and Their Interactions - Concepts and Phenomena*; Springer, 1998.

[78] Raimes, S. *Many-electron Theory*; North-Holland, 1972.

[79] Harbach, P. H. P.; Wormit, M.; Dreuw, A. The third-order algebraic diagrammatic construction method (ADC(3)) for the polarization propagator for closed-shell molecules: Efficient implementation and benchmarking. *J. Chem. Phys.* **2014**, *141*, 064113.

[80] Møller, C.; Plesset, M. S. Note on an Approximation Treatment for Many-Electron Systems. *Phys. Rev.* **1934**, *46*, 618–622.

[81] Koch, W.; Holthausen, M. C. *A chemist's guide to density functional theory*; Wiley-VCH, 2000.

[82] Hohenberg, P.; Kohn, W. Inhomogeneous Electron Gas. *Phys. Rev.* **1964**, *136*, B864–B871.

[83] Perdew, J. P.; Schmidt, K. Jacob's ladder of density functional approximations for the exchange-correlation energy. AIP Conference Proceedings. 2001; pp 1–20.

[84] Runge, E.; Gross, E. K. U. Density-Functional Theory for Time-Dependent Systems. *Phys. Rev. Lett.* **1984**, *52*, 997–1000.

[85] Dreuw, A.; Head-Gordon, M. Single-Reference ab Initio Methods for the Calculation of Excited States of Large Molecules. *Chem. Rev.* **2005**, *105*, 4009–4037.

[86] Ullrich, C. A. *Time-Dependent Density-Functional Theory. Concepts and Applications*; Oxford University Press, 2012.

[87] van Leeuwen, R. Mapping from Densities to Potentials in Time-Dependent Density-Functional Theory. *Phys. Rev. Lett.* **1999**, *82*, 3863–3866.

[88] Casida, M. E. In *Recent Advances in Density Functional Methods*; Chong, D. E., Ed.; World Scientific, 1995; pp 155–192.

[89] Tsuneda, T.; Hirao, K. Long-range correction for density functional theory. *WIREs Comput. Mol. Sci.* **2014**, *4*, 375–390.

[90] Tawada, Y.; Tsuneda, T.; Yanagisawa, S. A long-range-corrected time-dependent density functional theory. *J. Chem. Phys.* **2004**, *120*, 8425–8433.

[91] Yanai, T.; Tew, D. P.; Handy, N. C. A new hybrid exchange–correlation functional using the Coulomb-attenuating method (CAM-B3LYP). *Chem. Phys. Lett.* **2004**, *393*, 51–57.

[92] Chai, J.-D.; Head-Gordon, M. Long-range corrected hybrid density functionals with damped atom-atom dispersion corrections. *Phys. Chem. Chem. Phys.* **2008**, *10*, 6615–6620.

[93] Senn, H. M.; Thiel, W. QM/MM Methods for Biomolecular Systems. *Angew. Chem. Int. Ed.* **2009**, *48*, 1198–1229.

[94] Lin, H.; Truhlar, D. G. QM/MM: what have we learned, where are we, and where do we go from here? *Theor. Chem. Acc.* **2007**, *117*, 185–199.

[95] Brunk, E.; Rothlisberger, U. Mixed Quantum Mechanical/Molecular Mechanical Molecular Dynamics Simulations of Biological Systems in Ground and Electronically Excited States. *Chem. Rev.* **2015**, *115*, 6217–6263.

[96] Friesner, R.; Guallar, V. Ab initio quantum chemical and mixed quantum mechanics/molecular mechanics (QM/MM) methods for studying enzymatic catalysis. *Annu. Rev. Phys. Chem.* **2005**, *56*, 389–427.

[97] Mennucci, B. Polarizable continuum model. *WIREs Comput. Mol. Sci.* **2012**, *2*, 386–404.

[98] Klamt, A. The COSMO and COSMO-RS solvation models. *WIREs Comput. Mol. Sci.* **2011**, *1*, 699–709.

[99] Tomasi, J.; Mennucci, B.; Cammi, R. Quantum Mechanical Continuum Solvation Models. *Chem. Rev.* **2005**, *105*, 2999–3093.

[100] Nogueira, J. J.; González, L. Computational Photophysics in the Presence of an Environment. *Annu. Rev. Phys. Chem.* **2018**, *69*.

[101] Barone, V.; Cossi, M. Quantum Calculation of Molecular Energies and Energy Gradients in Solution by a Conductor Solvent Model. *J. Phys. Chem. A* **1998**, *102*, 1995–2001.

[102] Cossi, M.; Rega, N.; Scalmani, G.; Barone, V. Polarizable dielectric model of solvation with inclusion of charge penetration effects. *J. Chem. Phys.* **2001**, *114*, 5691–5701.

[103] Klamt, A.; Schuurmann, G. COSMO: a new approach to dielectric screening in solvents with explicit expressions for the screening energy and its gradient. *J. Chem. Soc., Perkin Trans. 2* **1993**, *5*, 799–805.

[104] Klamt, A. Conductor-like Screening Model for Real Solvents: A New Approach to the Quantitative Calculation of Solvation Phenomena. *J. Phys. Chem.* **1995**, *99*, 2224–2235.

[105] Sinnecker, S.; Rajendran, A.; Klamt, A.; Diedenhofen, M.; Neese, F. Calculation of Solvent Shifts on Electronic g-Tensors with the Conductor-Like Screening Model (COSMO) and Its Self-Consistent Generalization to Real Solvents (Direct COSMO-RS). *J. Phys. Chem. A* **2006**, *110*, 2235–2245.

[106] Plasser, F.; Wormit, M.; Dreuw, A. New tools for the systematic analysis and visualization of electronic excitations. I. Formalism. *J. Chem. Phys.* **2014**, *141*, 024106.

[107] Mulliken, R. S. Electronic Population Analysis on LCAO–MO Molecular Wave Functions. I. *J. Chem. Phys.* **1955**, *23*, 1833–1840.

[108] Bäppler, S. A.; Plasser, F.; Wormit, M.; Dreuw, A. Exciton analysis of many-body wavefunctions: Bridging the gap between solid-state physics and quantum chemistry. *Phys. Rev. A* **2014**, *90*, 052521.

[109] Mewes, S. A.; Mewes, J.-M.; Dreuw, A.; Plasser, F. Excitons in poly(para phenylene vinylene): a quantum-chemical perspective based on high-level ab initio calculations. *Phys. Chem. Chem. Phys.* **2016**, *18*, 2548–2563.

[110] Plasser, F.; Lischka, H. Analysis of Excitonic and Charge Transfer Interactions from Quantum Chemical Calculations. *J. Chem. Theory Comput.* **2012**, *8*, 2777–2789.

[111] Aquilante, F.; Autschbach, J.; Carlson, R. K.; Chibotaru, L. F.; Delcey, M. G.; Vico, L. D.; Galván, I. F.; Ferré, N.; Frutos, L. M.; Gagliardi, L.; Garavelli, M.; Giussani, A.; Hoyer, C. E.; Manni, G. L.; Lischka, H.; Ma, D.; Malmqvist, P. A.; Müller, T.; Nenov, A.; Olivucci, M.; Pedersen, T. B.; Peng, D.; Plasser, F.; Pritchard, B.; Reiher, M.; Rivalta, I.; Schapiro, I.; Segarra-Martí, J.; Stenrup, M.; Truhlar, D. G.; Ungur, L.; Valentini, A.; Vancoillie, S.; Veryazov, V.; Vysotskiy, V. P.; Weingart, O.; Zapata, F.; Lindh, R. MOLCAS 8: New Capabilities for Multiconfigurational Quantum Chemical Calculations across the Periodic Table. 2016.

[112] Nemethy, G.; Ray, A. Solvent effects on the near-ultraviolet spectrum of phenol and its distribution in micellar solutions. *J. Phys. Chem.* **1973**, *77*, 64–68.

[113] Kendall, R.; T.H. Dunning, J.; Harrison, R. Electron affinities of the first-row atoms revisited. Systematic basis sets and wave functions. *J. Chem. Phys.* **1992**, *96*, 6796–6806.

[114] Feller, D. The Role of Databases in Support of Computational Chemistry Calculations. *J. Comp. Chem.* **1996**, *17*, 1571–1586.

[115] Schuchardt, K.; Didier, B.; Elsethagen, T.; Sun, L.; Gurumoorthi, V.; Chase, J.; Li, J.; Windus, T. Basis Set Exchange: A Community Database for Computational Sciences. *J. Chem. Inf. Model.* **2007**, *47*, 1045–1052.

[116] Finley, J.; Åke Malmqvist, P.; Roos, B. O.; Serrano-Andrés, L. The multi-state CASPT2 method. *Chem. Phys. Lett* **1998**, *288*, 299–306.

[117] Zobel, J. P.; Nogueira, J. J.; González, L. The IPEA dilemma in CASPT2. *Chem. Sci.* **2017**, *8*, 1482–1499.

[118] Case, D.; Cerutti, D.; III, T. C.; Darden, T.; Duke, R.; Giese, T.; Gohlke, H.; Goetz, A.; D. Greene, N. H.; Izadi, S.; Kovalenko, A.; Lee, T.; LeGrand, S.; Li, P.; Lin, C.; Liu, J.; Luchko, T.; Luo, R.; Mermelstein, D.; Merz, K.; Monard, G.; Nguyen, H.; Omelyan, I.; Onufriev, A.; Pan, F.; Qi, R.; Roe, D.; Roitberg, A.; Sagui, C.; Simmerling, C.; Botello-Smith, W.; Swails, J.; Walker, R.; Wang, J.; Wolf, R.; Wu, X.; Xiao, L.; York, D.; Kollman, P. AMBER 16. 2017.

[119] Wang, J.; Wolf, R. M.; Caldwell, J. W.; Kollman, P. A.; Case, D. A. Development and testing of a general amber force field. *J. Comput. Chem.* **2004**, *25*, 1157–1174.

[120] Salomon-Ferrer, R.; Goetz, A. W.; Poole, D.; Grand, S. L.; Walker, R. C. Routine microsecond molecular dynamics simulations with AMBER - Part II: Particle Mesh Ewald. *J. Chem. Theory Comput.* **2013**, *9*, 3878–3888.

[121] Goetz, A. W.; Williamson, M. J.; Xu, D.; Poole, D.; Grand, S. L.; Walker, R. C. Routine microsecond molecular dynamics simulations with AMBER - Part I: Generalized Born. *J. Chem. Theory Comput.* **2012**, *8*, 1542–1555.

[122] Grand, S. L.; Goetz, A. W.; Walker, R. C. SPFP: Speed without compromise - a mixed precision model for GPU accelerated molecular dynamics simulations. *Comp. Phys. Comm.* **2013**, *184*, 374–380.

[123] Jorgensen, W. L.; Chandrasekhar, J.; Madura, J. D.; Impey, R. W.; Klein, M. L. Comparison of simple potential functions for simulating liquid water. *J. Chem. Phys.* **1983**, *79*, 926–935.

[124] Miyamoto, S.; Kollman, P. A. SETTLE: An Analytical Version of the SHAKE and RATTLE Algorithm for Rigid Water Models. *J. Comp. Chem.* **1992**, *13*, 952–962.

[125] Ryckaert, J.-P.; Ciccotti, G.; Berendsen, H. J. Numerical integration of the cartesian equations of motion of a system with constraints: molecular dynamics of n-alkanes. *J. Comp. Phys.* **1977**, *23*, 327–341.

[126] TURBOMOLE V7.0 2015, a development of University of Karlsruhe and Forschungszentrum Karlsruhe GmbH, 1989-2007, TURBOMOLE GmbH, since 2007; available from http://www.turbomole.com.

[127] Ahlrichs, R.; Bär, M.; Häser, M.; Horn, H.; Kölmel, C. Electronic structure calculations on workstation computers: The program system turbomole. *Chem. Phys. Lett* **1989**, *162*, 165–169.

[128] Furche, F.; Ahlrichs, R.; Hattig, C.; Klopper, W.; Sierka, M.; Weigend, F. Turbomole. *WIREs Comput. Mol. Sci.* **2014**, *4*, 91–100.

[129] Hättig, C.; Weigend, F. CC2 excitation energy calculations on large molecules using the resolution of the identity approximation. *J. Chem. Phys.* **2000**, *113*, 5154.

[130] Köhn, A.; Hättig, C. Analytic gradients for excited states in the coupled-cluster model CC2 employing the resolution-of-the-identity approximation. *J. Chem. Phys.* **2003**, *119*, 5021–5036.

[131] Plasser, F. "TheoDORE 1.5.1: a package for theoretical density, orbital relaxation, and exciton analysis"; available from http://theodore-qc.sourceforge.net.

[132] Plasser, F.; Lischka, H. Analysis of excitonic and charge transfer interactions from quantum chemical calculations. *J. Chem. Theo. Comp.* **2012**, *8*, 2777–2789.

[133] Plasser, F.; Bäppler, S. A.; Wormit, M.; Dreuw, A. New tools for the systematic analysis and visualization of electronic excitations. Part II: Applications. *J. Chem. Phys,* **2014**, *141*, 024107.

[134] Kumar, A.; Walker, J. A.; Bartels, D. M.; Sevilla, M. D. A Simple ab Initio Model for the Hydrated Electron That Matches Experiment. *J. Phys. Chem. A* **2015**, *119*, 9148–9159.

[135] Löwdin, P.-O. On the Non-Orthogonality Problem Connected with the Use of Atomic Wave Functions in the Theory of Molecules and Crystals. *J. Phys. Chem.* **1950**, *18*, 365–375.

[136] Löwdin, P.-O. On the Nonorthogonality Problem. *Adv. Quantum Chem.* **1970**, *5*, 185–199.

[137] Christ, C. D.; Mark, A. E.; van Gunsteren, W. F. Basic ingredients of free energy calculations: A review. *J. Comput. Chem.* **2010**, *31*, 1569–1582.

[138] Kästner, J. Umbrella sampling. *WIREs Comput. Mol. Sci.* **2011**, *1*, 932–942.

[139] Christiansen, O.; Koch, H.; Jørgensen, P. The second-order approximate coupled cluster singles and doubles model CC2. *Chem. Phys. Lett.* **1995**, *243*, 409–418.

[140] Frisch, M. J.; Trucks, G. W.; Schlegel, H. B.; Scuseria, G. E.; Robb, M. A.; Cheeseman, J. R.; Scalmani, G.; Barone, V.; Mennucci, B.; Petersson, G. A.; Nakatsuji, H.; Caricato, M.; Li, X.; Hratchian, H. P.; Izmaylov, A. F.; Bloino, J.; Zheng, G.; Sonnenberg, J. L.; Hada, M.; Ehara, M.; Toyota, K.; Fukuda, R.; Hasegawa, J.; Ishida, M.; Nakajima, T.; Honda, Y.; Kitao, O.; Nakai, H.; Vreven, T.; Montgomery, J. A., Jr.; Peralta, J. E.; Ogliaro, F.; Bearpark, M.; Heyd, J. J.; Brothers, E.; Kudin, K. N.; Staroverov, V. N.; Kobayashi, R.; Normand, J.; Raghavachari, K.; Rendell, A.; Burant, J. C.; Iyengar, S. S.; Tomasi, J.; Cossi, M.; Rega, N.; Millam, J. M.; Klene, M.; Knox, J. E.; Cross, J. B.; Bakken, V.; Adamo, C.; Jaramillo, J.; Gomperts, R.; Stratmann, R. E.; Yazyev, O.; Austin, A. J.; Cammi, R.; Pomelli, C.; Ochterski, J. W.; Martin, R. L.; Morokuma, K.; Zakrzewski, V. G.; Voth, G. A.; Salvador, P.; Dannenberg, J. J.; Dapprich, S.; Daniels, A. D.; Farkas, O.; Foresman, J. B.; Ortiz, J. V.; Cioslowski, J.; Fox, D. J. Gaussian 09, Revision D.01. Gaussian Inc. Wallingford CT 2009.

[141] Jäger, M.; Freitag, L.; González, L. Using computational chemistry to design Ru photosensitizers with directional charge transfer. *Coord. Chem. Rev.* **2015**, *304*, 146–165.

[142] Dreuw, A.; Weismann, J.; Head-Gordon, M. Failure of Time-Dependent Density Functional Theory for Long-Range Charge-Transfer Excited States: The Zincbacteriochlorin-Bacteriochlorin and Bacteriochlorophyll-Spheroidene Complexes. *J. Am. Chem. Soc.* **2004**, *126*, 4007–4016.

[143] Dreuw, A.; Head-Gordon, M. Long-range charge-transfer excited states in time-dependent density functional theory require non-local exchange. *J. Chem. Phys.* **2003**, *119*, 2943–2946.

[144] Lee, W.; Matsika, S. Conformational and electronic effects on the formation of anti cyclobutane pyrimidine dimers in G-quadruplex structures. *Phys. Chem. Chem. Phys.* **2017**, *19*, 3325–3336.

ACKNOWLEDGEMENTS

First, I would like to thank Prof. Leticia González for mentoring me on my way in quantum chemistry and giving me the opportunity to work in her group.

I am especially grateful to Dr. Juan José Nogueira Pérez for his great supervision of my work, his advice and support and his patience with me.

I would also like to thank Dr. Felix Plasser for help with the TheoDORE analysis package.

I am grateful to Dr. Clemens Rauer, Dr. Michael Gastegger, Sandra Gómez, Dr. Boris Maryasin, Martina de Vetta, Dr. Nicolás Ramos, Patrick Zobel and Dr. Pedro A. Sanchez Murcia for helpful discussions.

On the technical side, I would like to acknowledge Dr. Markus Oppel and Dimitri Robl for maintaining the computational resources of the González group.

I would like to thank the former and present members of the González research group for the nice working atmosphere.

Furthermore, I am grateful to Trini for her advice, which I will try to follow.

Last but not least, I would like to thank my family and friends for the support and encouragement.